Phase Information and Phase Modulated Signals in Fiber Optical Communications

Junjia Wang

Department of Electrical & Computer Engineering
McGill University
Montreal, Quebec, Canada

October 2011

A thesis submitted to McGill University in partial fulfillment of the requirements for the degree of Master of Engineering.

Abstract

In future telecommunication networks, a wide range of pulse durations 0.1–100 ps, duty cycles from less than 1% to 99%, and different modulation formats, such as on-off-keying (OOK) and binary or differential phase-shift-keying (BPSK or DPSK) will be selected, depending on the network size and the bit rate. A transparent all-optical format conversion between OOK and DPSK is highly demanded to connect cost effective OOK based metropolitan area networks (MAN) to robust PSK-based long-haul backbone networks. Moreover, for such complex optical transmission systems, the information on the phase and amplitude of the pulses is required for predicting the effects of chromatic dispersion and various optical nonlinearities. A temporal resolution of 1 ps and a sensitivity of less than 0.1 mW are required for an ideal characterization of optical pulses used in optical communications systems.

In this thesis, we simulate the simple method of pulse characterization using sinusoidal optical phase modulation proposed by Kang and Dorrer using OptiSystem™ and MATLAB™. We also experimentally verify this method. A detailed characterization of all optical OOK to DPSK format conversion is presented by comparing simulation and experimental results for the receiver sensitivity (*i.e.*, received power to have a BER of 10^{-9}) on the important properties of the input signal. By knowing the optimum configuration of the single channel OOK to DPSK format conversion, we then perform an OOK to DPSK format conversion with wavelength multicasting, which can operate simultaneously at four different wavelengths.

Abrégé

Les réseaux de communications optiques de l'avenir sont plus complexes : la durée des impulsions varie entre 0.1 ps et 100 ps, les rapports cycliques peuvent s'étendre entre 1% et 100% et il y aura différents formats de modulation. Par exemple, le choix entre la modulation à tout ou rien (OOK) et la modulation par excursion différentielle (DPSK) se fait en fonction de l'étendue du réseau et le débit binaire. Un format de conversion entre OOK et DPSK qui est intégralement optique est requis pour connecter les MAN basées sur le format OOK, qui est rentable, et DPSK, qui est très utile pour l'infrastructure des réseaux à longues distances. Pour les systèmes de transmission optique complexe comme ceux-ci, les informations sur la phase et l'amplitude des impulsions sont requises pour prédire les effets de la dispersion chromatique et des diverses non linéarités optiques. Une résolution de 1 ps et une sensibilité plus basse que 0.1 mW sont nécessaires pour caractériser les impulsions idéales utilisées dans les systèmes de communications optiques. Dans cette thèse, nous avons utilisé OptiSystem™ et MATLAB™ pour simuler une méthode simple pour caractériser les formats de modulations optiques de phases sinusoïdales proposées par Inuk Kang et Christophe Dorrer. Nous avons aussi prouvé la méthode expérimentalement. Une caractérisation détaillée des formats de conversion de OOK a DPSK est présentée en faisant la comparaison des simulations et des résultats expérimentaux pour vérifier l'influence de la puissance reçue, qui doit avoir un BER de 10^{-9}, sur les propriétés importantes du signal d'entré. L'optimisation de la configuration des formats de conversion de OOK à DPSK pour un seul canal nous a permis de concevoir la conversion multipoint de OOK à DPSK pour l'opération simultanée de quatre longueurs d'ondes différentes.

ACKNOWLEDGMENTS

I feel very fortunate to meet and work with so many incredible individuals at McGill University during my Masters study. Foremost, I thank my supervisor Professor Lawrence R. Chen for his guidance and support throughout the past two years. I have benefited tremendously from his profound thinking, generosity and integrity.

I would like to thank many people who have supported my Master's degree studies and helped me through the process of writing this thesis. Especially Pegah, for teaching me hand by hand about how to use the equipment. It was a privilege to work together with you in the lab.

I extend many thanks to everyone in PSG department. I would like to thank Professor Andrew Kirk for introducing me to the field of photonics. I also thank Professor Martin Rochette for teaching me nonlinear optics and fiber optics. I would like to thank Professors David Plant who organized the lab and Zhaobing who developed the equipment booking system. I would like to thank Victor, Pegah, Payman, Maria, Xinghua, Chris, Jia, Lv, Tianye and Wanjing for the good time that we had during the weekly group meetings as well as outside the lab.

I could not forget all people I met during last two years in Montreal who gave me unforgettable moments.

Last, but not the least, thanks to my family who always supported me in all my decisions and gave me the possibility to study aboard. Thank you mom for all your loving care, advice and support during all my student life. I would have never studied for this degree if you had not encouraged me.

TABLE OF CONTENTS

LIST OF FIGURES

LIST OF TABLES

LIST OF ACRONYMS

ASE	Amplified Spontaneous Emission
AWG	Arrayed Waveguide Grating
BPSK	Binary Phase Shift Keying
CS-RZ	Carrier-Suppressed Return-to-Zero
CW	Continuous Wave
DCA	Digital Communications Analyzer
DCF	Dispersion Compensating Fiber
DGD	Differential Group Delay
DPSK	Differential Phase Shift Keying
DQPSK	Differential Quadrature Phase Shift Keying
DSF	Dispersion Shifted Fiber
DSP	Digital Signal Processing
DWDM	Dense Wavelength Division Multiplexing
EAM	Electro-Absorption Modulator
EDFA	Erbium-Doped Fiber Amplifier
EOM	Electro-Optic Modulator
FROG	Frequency Resolved Optical Gating

FWM	Four-Wave Mixing
FWHM	Full Width at Half Maximum
HNLF	Highly Nonlinear Fiber
GVD	Group Velocity Dispersion
ITU	International Telecommunications Union
MAN	Metropolitan Area Network
MLL	Mode-Locked Laser
MZM	Mach-Zehnder Modulator
NLSE	Nonlinear Schrödinger Equation
NRZ-OOK	Non-Return-to-Zero On-Off Keying
NZ-DSF	Non-Zero Dispersion Shifted Fiber
OSA	Optical Spectrum Analyzer
OTDM	Optical Time Division Multiplexing
PC	Polarization Controller
PPG	Pulse Pattern Generator
QPSK	Quadrature Phase Shift Keying
RF	Radio Frequency
RZ	Return-to-Zero
RZ-OOK	Return-to-Zero On-Off Keying
RZ-DPSK	Return-to-Zero Differential Phase Shift Keying
SMF	Single-Mode Fiber
SOA	Semiconductor Optical Amplifier
SPM	Self-Phase Modulation
TBPF	Tunable Bandpass Filter

TLS	Tunable Laser Source
TODL	Tunable Optical Delay Line
VOA	Variable Optical Attenuator
WAN	Wide Area Network
WDM	Wavelength Division Multiplexing
XAM	Cross-Absorption Modulation
XGM	Cross-Gain Modulation
XPM	Cross Phase Modulation
2R	Re-amplifying and Re-shaping

Chapter 1

Introduction

Light has always been with us. Communication using light occurred early in our evolution, when human beings started communicating with hand signals. This is definitely a form of optical communications. The sun is the source and the hand modulates the light, but the transfer speed of such a system is slow, the transmission distance is limited, and the possibilities of errors are great. A later optical communication system, which has a longer transmission distance, employed smoke. By varying the pattern of smoke rising from a fire, which is a form of coding, the message can be transmitted between the communicator and receiver. In 1880, Alexander Graham Bell invented the photophone [1]. A thin voice-modulated mirror was used to modulate the reflected sunlight, and the modulated sunlight fell on a photoconducting selenium cell. Thus, the sunlight is converted into electric current and received by a telephone receiver. During the 1940s, microwave communication systems were commercialized and carrier frequencies of up to 4 GHz were used commercially between New York and Boston [2]. During the next 25 years or so,

microwave as well as coaxial systems were approaching their fundamental limits. It was realized in the 1950s that a drastic increase in transmission capacity could be possible if optical waves replaced microwaves as the carrier of information. A major breakthrough that led to an increase of several orders of magnitude in the transmission capacity was the invention of the laser in 1960 [3]. Unguided optical communication systems were invented shortly after the discovery of the laser, but in contrast with microwave systems, optical waves were constrained by many conditions when they were transmitted through the air, such as the dependence on a clear atmosphere or the need for a line-of-sight between transmitter and receiver. In 1966, K. C. Kao and G. A. Hockman suggested that optical fibers might be the best choice for transporting optical signals [4]. But a key element in a practical fiber system was missing, namely a low loss fiber, since fibers available at the time had losses of 1,000 dB/km [5]. It was not until 1970 when fiber with losses below 20 dB/km was developed and fiber optic communications became practical [6]. In the 1980s, the second generation of fiber optic communication systems which operated at 1.3 μm became available due to the invention of single mode fiber. A transmission at 2 Gb/s over 44 km was demonstrated in 1981 [7]. The third generation of fiber optic communications operated at the wavelength of minimum loss of silica fibers, which is 1.55 μm, and dispersion-shifted fibers were introduced to overcome the relatively large dispersion. Laboratory experiments demonstrated successful transmission over 100 km at a bit rate of 4 Gb/s [8]. The fourth generation of lightwave systems employed optical amplification instead of electronic repeaters to increase the distance of the regeneration period, and wavelength-division multiplexing (WDM) was employed to increase the system capacity. After 1992, the WDM technique started a revolution that doubled the system capacity every 6 months, up to 2000, resulting in data rates

beyond 10 Tb/s over several hundreds of kilometers [5]. The pace slowed down after 2001 due to the economic downturn as well as the spectral limit of dense wavelength-division-multiplexing (DWDM). The fifth generation of lightwave systems adopted the Raman amplification technique to extend the conventional wavelength window to both the long and short-wavelength sides. In brief, the DWDM system capacity can be increased by using a wider optical bandwidth, by increasing the spectral efficiency (SE), or by combining the two [9]. Modulation formats are key to increasing SE. High SE modulation formats can effectively increase the transmission capacity without expanding the bandwidth of optical amplifiers. Recently, research in high capacity transmission has shifted to coherent detection. Coherent detection in conjugation with digital signal processing (DSP) enables compensation of fiber optic transmission impairments, revealing new possibilities that will likely shape the future of optical communications. Table 1 shows a selection of record numbers recently achieved in research laboratories, with up to 160 channels at per channel data rates of 100 Gb/s [16].

1.1

Phase Shift Keying Techniques

Phase shift keying (PSK) is a modulation scheme that conveys data by changing the phase of a reference signal. Figure 1.1 shows the basic idea of binary phase shift keying (BPSK) system operating at a carrier frequency f_T, $x(t)$ represents the data signal and can be expressed as

$$x(t) = \sum_{-\infty}^{+\infty} b_k h(t - kT_b), \qquad (1.1)$$

	Capacity	Distance	Capacity x Distance
273×40 Gb/s tripe-band/ultra-dense WDM [11]	10.9 Tb/s (273 ch × 40 Gb/s)	117 km	1.3 Pb/s·km
256 wavelength-division and polarization-division multiplexed at 42.7 Gb/s [12]	10.2 Tb/s (256 ch × 42.7 Gb/s)	3x100 km TeraLight fiber	3.1 Pb/s·km
WDM using 42.7 Gb/s differential phase shift keying [13]	6.0 Tb/s (149 ch × 42.7 Gb/s)	6100 km	36 Pb/s·km
64×42.7 Gb/s using RZ-DPSK and all Raman amplified spans [14]	2.6 Tb/s (64 ch × 42.7 Gb/s)	40x100 km NZDF	10 Pb/s·km
DWDM using CSRZ-DPSK and enhanced FEC and all Raman amplified Ultrawave fiber spans[15]	1.6 Tb/s (40 ch × 42.7 Gb/s)	10000 km	16 Pb/s·km
160×100 Gb/s using PDM QPSK modulation format and coherent receiver [16]	16.4 Tb/s (160 ch x 100Gb/s)	2550 km	41.8 Pb/s·km

Table 1.1 Some Recent Record Fiber-Optic Transmission Results [10].

where T_b is the bit rate, $h(t)$ is the impulse response function of the system and data $b_k \in \{-1; 1\}$, the BPSK system uses carrier phases of 0 and π [17]. The demodulator at the receiver end should be matched to the transmitted signal and a low-pass filter is necessary to filter out the signal component occurring at twice the carrier frequency. But unfortunately, this simple method cannot be adopted by lightwave systems, since the optical to digital conversion implemented by the photodiode automatically imposes a magnitude squared operation on the complex envelope of the incoming optical signal. There are two distinctive PSK implementations which can be found in the literature. One is PSK with coherent detection, including heterodyne and homodyne detection, and is implemented using a local oscillator for demodulation. The other method is the direct detection of self-homodyne differential phase shift keying (DPSK) and is implemented using a Mach–Zehnder delay interferometer (MZDI). Concerning receiver sensitivity, the coherent PSK implementation is

favorable, since the received noisy signal is modulated with a less noisy signal provided by the local oscillator, in contrast to the direct detection case where the received noisy signal is split into two and interfered in the MZDI. But C. Xu *et al.* suggested that direct detection is much more practical to implement at high data rate and only suffers a small penalty in receiver sensitivity [18]. A typical balanced DPSK receiver is shown in Fig. 1.2 [19]. The received optical signal is first split into two and launched into a MZDI, and one beam is delayed by a time delay corresponding to the bit period. The MZDI lets two adjacent bits recombine and coherently interfere with each other, which leads to the presence (absence) of power at one output port if the two bits interfere constructively (destructively). Instead of the local oscillator which beats with the received signal to produce constructive and destructive interference, in direct detection, the preceding bit in a DPSK-encoded bit stream acts as the phase reference for demodulating the current bit [20]. One of the DI output ports corresponding to destructive interference is the destructive port, while the other output port which exhibits constructive interference is the constructive port. Thus, the two MZDI output ports will carry logically inverted data under DPSK modulation. The constructive port carries duobinary modulation while the destructive port carries alternate-mark inversion (AMI) [19], [21]. Since both DI output ports carry the full information, they can be either detected by themselves (without the 3 dB advantage comparing to on-off keying (OOK)), or connected to a balanced receiver (in this case identical path lengths are required).

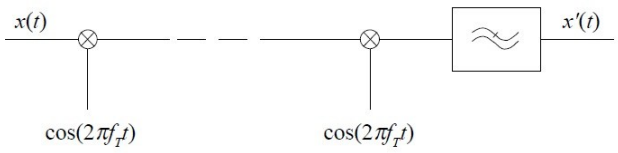

Figure 1.1 Schematic diagram of BPSK transmission [17].

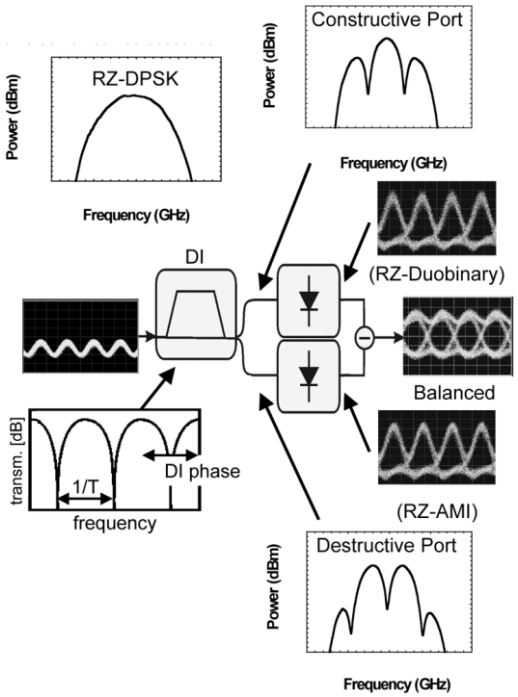

Figure 1.2 A typical DPSK receiver [19].

The benefit of DPSK compared to OOK is the 3 dB lower optical signal to noise ratio (OSNR) required to reach a given bit error rate (BER), which can easily be seen by comparing the signal constellations for DPSK and OOK, as shown in Figure 1.3. For the same optical power, only half is required for DPSK compared to OOK to reach the same symbol distance, which is proportional to OSNR. DPSK techniques were first operating as two-symbol transmission.

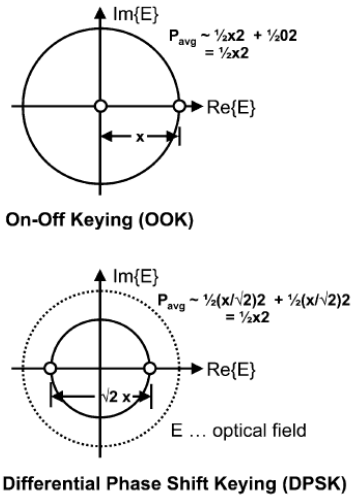

Figure 1.3 Signal constellation of binary on-off keying (top), and binary PSK (bottom) [19].

PSK for optical transmission was brought to attention in 1990 mainly in the field of coherent lightwave transmission, where a homodyne detection of PSK modulation gives the best theoretical receiver sensitivity of any of the binary modulation schemes [22]. In lightwave systems, the transmission distance is mainly restricted by three factors: the degradation of OSNR due to amplified spontaneous emission (ASE) generated by optical amplifiers, the degradation arising from the nonlinear effects of the optical fiber, and the degradation due to residual dispersion in the fiber transmission link. After the fourth generation employed erbium-doped fiber amplifiers (EDFAs) to compensate the loss, the interest in coherent detection of PSK for optical transmission decreased noticeably, since the ASE noise from the amplifier limits the transmission distance of PSK systems [23]. Over the next ten years, amplitude-shift keying (ASK), particularly OOK, was more favorable to PSK, and higher sensitivity became easily attainable. At the same time, due to the development of WDM technology, the capacity of the lightwave systems increased dramatically, not only the channel data rate but also the amount of channels. The SE has improved significantly, from a very low SE to approaching the binary limit of 0.8 bit/s/Hz in research laboratories [9]. Over the past few years, the desire of applying DPSK to long-haul WDM transmission has been revitalized. Return-to-zero differential phase shift keying (RZ-DPSK) is much more competitive at high data rates such as 40 Gb/s, due to the fact that the RZ format may reduce fiber nonlinear phase noise. Furthermore, signal degradation due to fiber nonlinearity is more severe with increasing SE. The OSNR can be increased by increasing the input optical power, but it enhances the degradation due to the nonlinear effect as well. Thus, the received OSNR is seriously limited in conventional OOK systems. Both numerical simulations [24] and experimental evidence [25][26] showed that using a DPSK technique in conjunction

with RZ-pulse shaping has superior tolerance to nonlinear phase noise. In [24], O. Vassilieva *et al.* have compared by numerical simulations the performance of NRZ, carrier-suppressed return-to-zero (CS-RZ), and DPSK modulation formats for propagation over 480 km of 40 channels WDM transmission with SMF and non-zero dispersion shifted fiber (NZ-DSF). The system parameters and fiber parameters are shown in Tables 1.2 and 1.3, respectively. From the bottom of Figure 1.4, we can see that NRZ suffers significant degradation of the eye opening due to nonlinear effects, while DPSK shows the clearest eye opening, having larger eye opening as well as smaller timing jitter. From the top of Figure 1.4, a more quantitative comparison is done by plotting the eye opening penalty; it is clearly seen that DPSK is much better than NRZ and CS-RZ. Figure 1.5 also proves that DPSK shows the highest power tolerance for both the SMF and NZ-DSF fibers. Figure 1.6 shows the dispersion tolerance curve for the central channel obtained at a fiber input power 2 dBm/ch. DPSK is more tolerant to dispersion compared with NRZ and CS-RZ for NZ-DSF and has the largest dispersion tolerance for SMF. In [26], C. Xu *et al.* show that OOK outperforms PSK in a low SE WDM system, which is shown in Figure 1.7(a). Figure 1.7(b) shows that the performance of DPSK is comparable to OOK at 10 Gb/s transmission with a spectral efficiency of 0.2. They also conclude by simulation that RZ-DPSK is advantageous in a high SE (e.g., 0.4 bits/s/Hz) system.

capacity	43 Gbit/s x 40 ch.
distance	80 km x 6 spans
channel allocation	1529.55 nm - 1560.61 nm, 100 GHz spacing
modulator chirp	+0.7
WDM filter shape	2nd order Gaussian, 76 GHz BW
polarization	same for all WDM channels
fiber input power	-2, 0, 2, 4, 6 dBm/ch
DCF input power	-5 dBm/ch.

Table 1.2 System parameters [24].

	SMF	NZ-DSF	DCF for SMF	DCF for NZ-DSF
D @1550 nm, ps/nm/km	17	4.4	-80	-90
S, ps/nm^2/km	0.057	0.045	-0.22	-0.65
loss, dB/km	0.2	0.2	0.45	0.5
effective area, μm^2	80	55	14	19
n_2, $x10^{-20}$ m^2/W	2.9	2.6	4.3	4.3

Table 1.3 Fiber parameters [24].

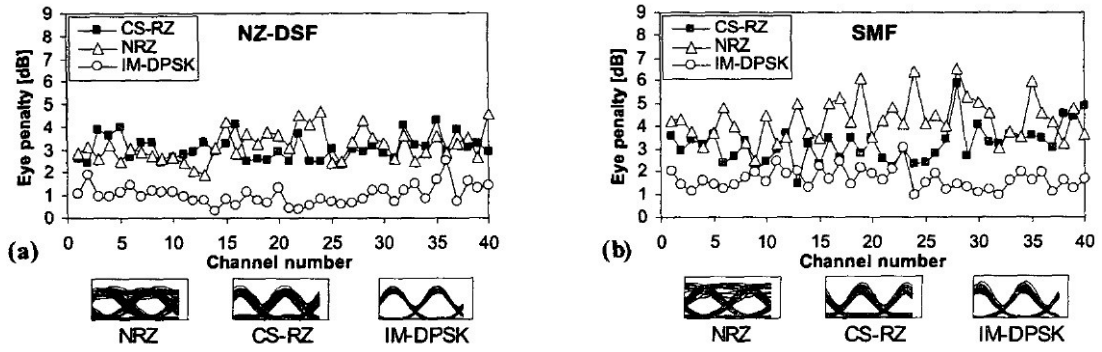

Figure 1.4 Eye penalty and eye diagrams after 480km transmission for (a) NZ-DSF and (b) SMF [24].

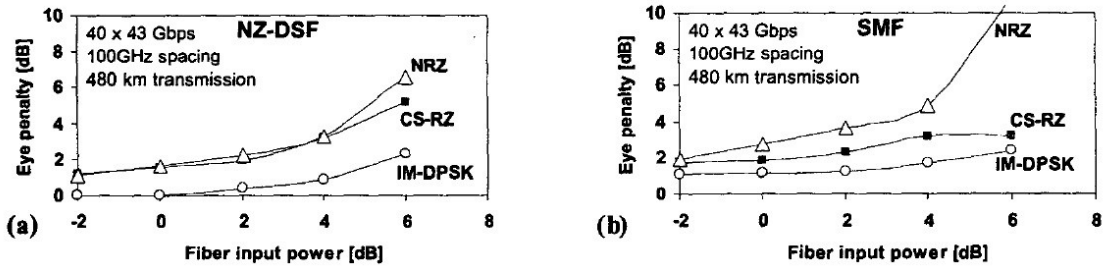

Figure 1.5 Power tolerance of IM-DPSK, CS-RZ and NRZ for (a) NZ-DSF and (b) SMF [24].

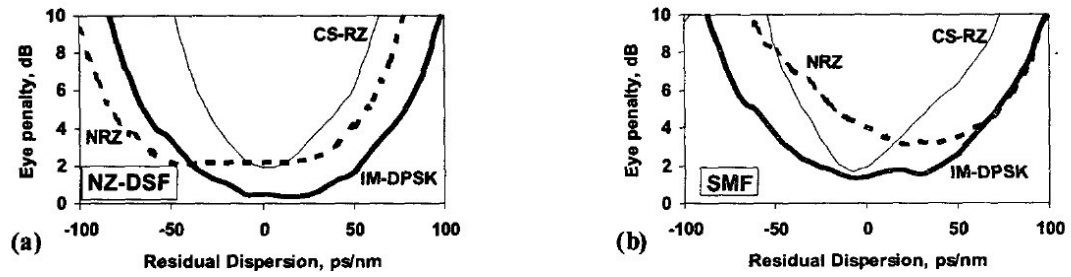

Figure 1.6 Dispersion tolerance for the central channel after 480km transmission with (a) NZ-DSF (b) SMF [24].

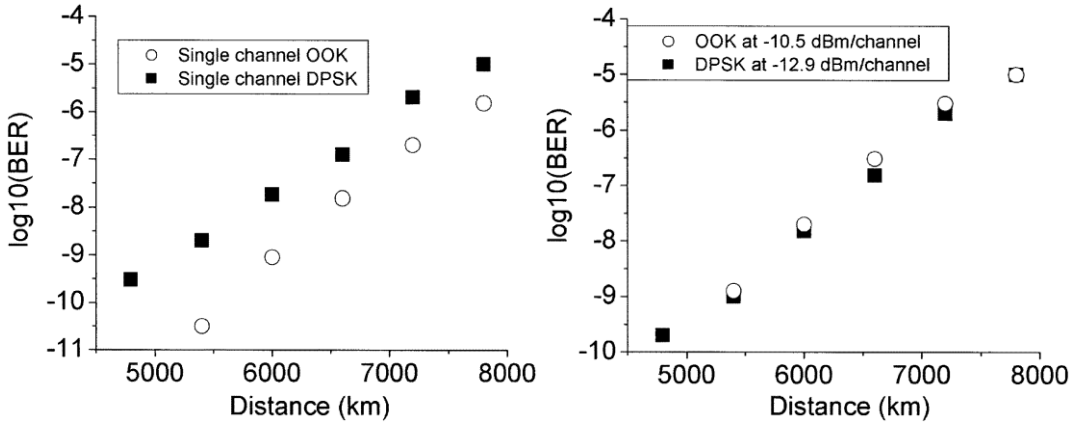

Figure 1.7(a) Single-channel RZ-OOK and RZ DPSK transmission at 10Gb/s (b) Dense WDM (10 Gb/s at 50-GHz channel separation) RZ-OOK and RZ DPSK transmission [26].

1.2

Motivation and Thesis Objectives

In future fiber optic communications systems, various modulation formats will be selected depending on the network size and the bit rate, which will increase network complexity. Table 1.4 shows the corresponding modulation formats that may be used for different kinds of optical networks.

Optical Network	**Modulation format**
Ultra long-haul systems	PSK
Long-haul systems	PSK, CSRZ, AMI
OTDM long-haul systems	RZ
WAN	RZ-DQPSK, PSK
MAN	NRZ, Duobinary
DWDM access network	NRZ

Table 1.4 Corresponding modulation formats for future optical networks.

Thus, in future optical networks, transparent all-optical format conversion between OOK and DPSK is highly demanded. In the past few years, researchers have proposed and demonstrated a variety of schemes for all optical format conversion between OOK and DPSK. These methods include the use of semiconductor optical amplifiers (SOAs) [27-28], highly nonlinear fiber (HNLF) [29-30] or nonlinear waveguides [44]. In [30], Kitagawa *et al.* experimentally demonstrated NRZ-OOK to RZ-QPSK based on fiber nonlinearity and also compared the performance of NRZ-OOK to RZ-BPSK and RZ-OOK to RZ-BPSK using numerical simulation. In [29], Mishina simulated and experimentally demonstrated NRZ-OOK to multilevel PSK based on nonlinearity in optical fiber. Using XPM in optical fiber is more attractive since SOAs suffer from

residual cross-gain modulation (XGM) and slow response time. The disadvantage of silica fiber is the high power level that is required. OOK to DPSK format conversion has been demonstrated only for an input NRZ signal at a fixed wavelength, and the subsequent performance of the conversion with signal degradation has not been investigated. Unlike the conventional lightwave systems, however, the performance of the fiber based OOK to DPSK conversion system can also be limited by a couple of impairments including: a mismatched interferometer delay (apart from imperfections in DI manufacturing, such a mismatch can occur from changes in line rate when upgrading installed systems with forward error correction (FEC) schemes [19]). Also the $\chi^{(3)}$ effect in HNLF is polarization-sensitive and the strength of the XPM effect induced by arbitrarily polarized RZ-OOK signals would fluctuate unpredictably. Recently, an experiment demonstration of RZ-OOK to RZ-BPSK format conversion using passive semiconductor waveguides has been reported, which provided an integrated solution for nonlinear signal processing [44]. In this thesis, a detailed characterization of the conversion is presented by directly comparing simulation and experimental results for the receiver sensitivity (*i.e.*, the received power necessary to obtain a BER of 10^{-9}) on the important properties of the input signal. These properties include:

- duty cycle
- peak power
- state-of-polarization
- optical signal-to-noise ratio (OSNR)
- residual dispersion
- polarization mode dispersion (PMD)

Collectively, the comprehensive set of results thoroughly characterizes the performance of the OOK to PSK format conversion by quantifying the requirements for the input signal properties. The specifications on the input signal quality is particularly useful for system design. By knowing the optimum configuration of the single channel OOK to DPSK format conversion, we then carry out an OOK to DPSK modulation format conversion system capable of wavelength multicasting. For such optical systems, and any other kinds of optical transmission systems, the information on the phase is highly demanded for predicting the effects from the chromatic dispersion and various optical nonlinearities. Thus, we simulated a simple method of pulse characterization using sinusoidal optical phase modulations proposed by Kang and Dorrer [31] using OptiSystem™ and MATLAB™. We also experimentally verified this method. The temporal resolution of this method is less than 1 ps and the sensitivity is less than 0.1 mW.

1.3

Thesis Outline

This thesis is organized as follows. In Chapter 2, a simple method of monitoring phase information for optical signals is described. The method is both examined by simulation and experiment. The simulation is performed by OptiSystem™, the algorithm to retrieve the phase information is performed by MATLAB™. The phase information of Gaussian pulses is extensively compared, by subjecting them to various chirp profiles and propagating them through fiber, exhibiting various dispersions and nonlinearities. In Chapter 3, a comprehensive investigation of all optical format conversion from OOK to DPSK at 10 Gb/s is provided. The design of a

multicasting OOK to DPSK format conversion is also discussed and verified by experiment. The analysis of the format conversion at 40 Gb/s is presented in Chapter 4. Finally, an overall summary and conclusion are provided in Chapter 5.

Chapter 2

Optical Pulse Phase Characterization Technique

2.1

Introduction

In the past few years, there has been a wide improvement in the complete characterization (intensity and phase information) of optical pulses, motivated mainly by the requirements of monitoring in high-speed all optical networking as shorter optical pulses are used for transmission and as the bit rate gets higher. For a typical optical transmission system, the information on the phase and amplitude of the pulses is required for predicting the effects from chromatic dispersion and optical nonlinearities. A temporal resolution of 1 ps and a sensitivity of less than 0.1 mW are required for an ideal characterization of optical sources typically used in networks without amplification [32]. Moreover, a wide range of pulse durations 0.1–100 ps,

duty cycles from less than 1% to 99%, and different modulation formats such as OOK and DPSK, should also be supported by signal monitoring. Practical pulse characterization can also optimize processes such as all-optical signal processing and nonlinear optical pulse compression [33]. Various conceptual approaches have been developed to meet the needs for signal characterization in communications applications, many of which draw on the methods developed for ultrashort pulse characterization [31]. Table 2.1 summarizes three types of measurement techniques that are the most commonly used for characterizing ultrashort optical pulses; the details can be found in [34].

Among these three characterization techniques, the method using sinusoidal optical phase modulation is considered to be easy and straightforward to implement. Non-iterative characterization of short optical pulses using sinusoidal optical phase modulation has been shown recently [31][33][35]. The simplified chronocyclic tomography (SCT) method proposed in [35] can fully characterize short optical pulses using just two pulse spectra recorded after the phase modulation. This method becomes very sensitive and fast when combined with the lock-in detection technique [33]. However, the SCT method has problems characterizing relatively long optical pulses whose temporal width is broad enough to break the quadratic phase modulation assumption [35]. An extension of this method has been proposed by Kang and Dorrer in [31], which uses four pulse spectra after phase modulation (instead of two) to reconstruct the pulse, thereby removing the limitation imposed by quadratic phase modulation. Also removed is the requirement for a specific temporal alignment between the pulse train and the modulation signal. In [36], Thomsen *et al.* claimed that the linear-spectrographic technique developed by Kang and Dorrer has much

greater sensitivity and much less polarization sensitivity compared to the nonlinear FROG technique developed by Trebino and Delong [37].

	Method	Devices	Properties
Spectrography	Measure a smoothed version of the chronocyclic Wigner function by using sequential amplitude filters to make a simultaneous measurement of time and frequency.	sonogram [38], frequency resolved optical gating (FROG) [39]	Most commonly used and very diverse in configuration. The electric field reconstruction is iterative in most cases.
Tomography	Measure projections of the chronocyclic Wigner function onto the frequency variable, following the application of a quadratic phase modulator to the input pulse. This serves to rotate the phase-space distribution of the pulse, so that a measurement of its modified spectrum reveals information about its initial orientation, and hence chirp.	temporal imaging system, simplified chronocyclic tomography (SCT) [32]	Difficult to implement reconstruction of femtosecond pulses in practice because of the difficulty in modulating pulses with sufficient bandwidth. Allows direct measurement and simple visualization of subpicosecond waveforms.
Interferometry	Measure a point or a section of the two-frequency or two-time correlation function. A single section of either function is adequate for reconstructing the underlying electric field.	spectral shearing interferometry (SSI), spectral phase interferometry for direct electric-field reconstruction (SPIDER) [40][41], test-plus-reference interferometry	Direct coding of spectral phase in the experimental data, allowing simple, robust and rapid inversion algorithms. SSI, is particularly adapted to the measurement of broadband pulses and has been implemented for a wide range of wavelengths and pulse durations.

Table 2.1 Corresponding measuring techniques

2.2

Theory

Figure 2.1(a) shows the experimental setup. The input optical signal is coupled into a phase modulator driven by a sinusoidal radio-frequency (RF). The frequency of the RF modulation is synchronized to the repetition rate of the signal under test. An optical spectrum analyzer (OSA) is used to measure the four spectra of the modulated

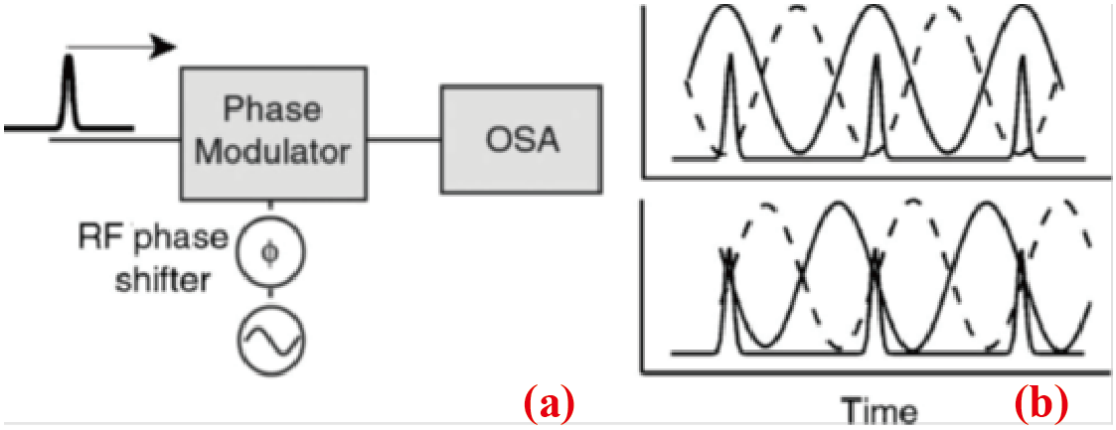

Figure 2.1 (a) Schematic of the measurement setup. (b) Timing between the pulses and cosine modulations (top) and sine modulations (bottom). [32]

signal needed for subsequent processing. The electric field of the input signal *E(t)* can be expressed as:

$$E(t) = \frac{1}{2\pi}\int E(\omega)e^{-i\omega t}d\omega = \frac{1}{2\pi}\int \sqrt{I(\omega)}\exp[i\varphi(\omega)]\,e^{-i\omega t}d\omega \qquad (2.1a)$$

where *t* is time; ω is optical frequency; *I(ω)* is the intensity envelope of the pulse; and *E(ω)* is the Fourier transform of *E(t)* which, being a complex value, is equivalently expressed as:

$$E(\omega) = \sqrt{I(\omega)}\exp[i\varphi(\omega)] \qquad (2.1b)$$

The sinusoidal RF signal can be described as:

$$\phi(t) = \psi\sin(\Omega t + \alpha_k) \qquad (2.2)$$

where Ω is the modulation frequency and ψ is the modulation amplitude. Using Eq. (2.2), the Fourier transforms of the modulated signal, $E_{\psi}^{k}(\omega)$, corresponding to the four sinusoidal signals, can be expressed as:

$$E_{\psi}^{\pm sin}(\omega) = \int[\pm i\psi\sin(\Omega t)]\,E(t)e^{i\omega t}dt \qquad (2.3a)$$

$$E_{\psi}^{\pm cos}(\omega) = \int[\pm i\psi\cos(\Omega t)]E(t)e^{i\omega t}dt \qquad (2.3b)$$

In practice, for a small ψ (less than 0.88), the two derivatives of $I_\psi(\omega)$ over ψ can be approximated using

$$\left.\frac{dI_\psi^{sin}(\omega)}{d\psi}\right|_{\psi=0} \approx \frac{I_\psi^{sin}(\omega)-I_\psi^{-sin}(\omega)}{2\psi} \quad (2.4a)$$

$$\left.\frac{dI_\psi^{cos}(\omega)}{d\psi}\right|_{\psi=0} \approx \frac{I_\psi^{cos}(\omega)-I_\psi^{-cos}(\omega)}{2\psi} \quad (2.4b)$$

The right hand sides of Eq. (2.4a) and Eq. (2.4b) contain the four spectra measured by the OSA.

We define a new quantity $\Delta(\omega)$:

$$\Delta(\omega) \equiv \left.\frac{dI_\psi^{cos}(\omega)}{d\psi}\right|_{\psi=0} + i\left.\frac{dI_\psi^{sin}(\omega)}{d\psi}\right|_{\psi=0} \quad (2.5)$$

which is the main equation we rely on for the electric field retrieval.

By substituting Eq. (2.4a) and Eq. (2.4b) into Eq. (2.5), we can express $\Delta(\omega)$ as

$$\Delta(\omega) = i[E(\omega+\Omega)E^*(\omega) - E(\omega)E^*(\omega-\Omega)] \quad (2.6)$$

Using Eq. (2.6), we can see that

$$\Delta(\omega - m\Omega) =$$

$$i[E(\omega-(m-1)\Omega)E^*(\omega-m\Omega) - E(\omega-m\Omega)E^*(\omega-(m+1)\Omega)] \quad (2.7)$$

By taking the summation, and for *E(ω)* with finite spectral content

$$\sum_{m=0}^{\infty}\Delta(\omega-m\Omega) = iE(\omega+\Omega)E^*(\omega) \quad (2.8)$$

Using Eq. (2.1b), the right hand side of Eq. (2.8) can be transformed into

$$\sqrt{I(\omega+\Omega)\mathrm{I}(\omega)}\mathrm{expi}[\varphi(\omega+\Omega)-\varphi(\omega)] = -i\sum_{m=0}^{\infty}\Delta(\omega-m\Omega) \quad (2.9a)$$

which is equivalent to

$$\sqrt{I(\omega+\Omega)\mathrm{I}(\omega)}\mathrm{expi}[\varphi(\omega+\Omega)-\varphi(\omega)] = i\sum_{m=1}^{\infty}\Delta(\omega+m\Omega) \quad (2.9b)$$

The right hand side of Eq. (2.9b) can be determined by using the data $I_\psi(\omega)$ measured from the OSA and then using Eqs. (2.4a-b) and Eq. (2.5) to calculate $\Delta(\omega)$ and then taking the summation. The phase angle of the right-hand side is equal to the phase angle of the left-hand side; thus, by determining the phase of the right hand side, we can get the value of $\varphi(\omega+\Omega)-\varphi(\omega)$. $\varphi(\omega+\Omega)-\varphi(\omega)$ is a recursion relation, from which we can get $\varphi(\omega)$ with Ω serving as a recursive increment.

After the determination of the phase of the signal, Eq. (2.1b) can be used to calculate *E(ω)*. *I(ω)* can be measured directly from the OSA or alternatively, *I(ω)* can be calculated using the approximation:

$$I(\omega) \approx \frac{I_\psi^{cos}(\omega)+I_\psi^{-cos}(\omega)}{2} \approx \frac{I_\psi^{sin}(\omega)+I_\psi^{-sin}(\omega)}{2} \quad (2.10)$$

The electric field in the time domain, *E(t)*, can then be calculated by using Eq. (2.1a). Finally, the intensity and phase can be extracted from *E(t)*:

$$I(t) = E(t)E^*(t) \quad (2.11)$$

$$\phi(t) = Arg(E(t)) \quad (2.12)$$

2.3

Simulation

The simulation of pulse generation and phase modulation is performed in OptiSystem™; we then use MATLAB™ to do the recursive calculations, using the data from OptiSystem™.

Figure 2.2 shows the basic schematic diagram of the simulation in OptiSystem™. The input signal is simulated by a bit generator coupled into a Gaussian pulse generator to generate a Gaussian pulse train at a bit rate of 10 Gb/s with a duty cycle of 25% and a peak power of 0 dBm. The carrier frequency is 193.1 THz. The signal then enters a phase modulator and is modulated with a sine wave generator. The frequency of the sine wave is 10 GHz and the amplitude is V_π. By adjusting the phase of the sine wave, we can acquire the data of the four spectra. Using the acquired data, the recursive calculation and Fourier transforms are calculated using MATLAB™. Different cases are simulated to assess the feasibility of this pulse characterization technique. For each case, unless mentioned specifically, the input optical signal is assumed to have zero chirp. Table 2.2 summarizes the different cases examined.

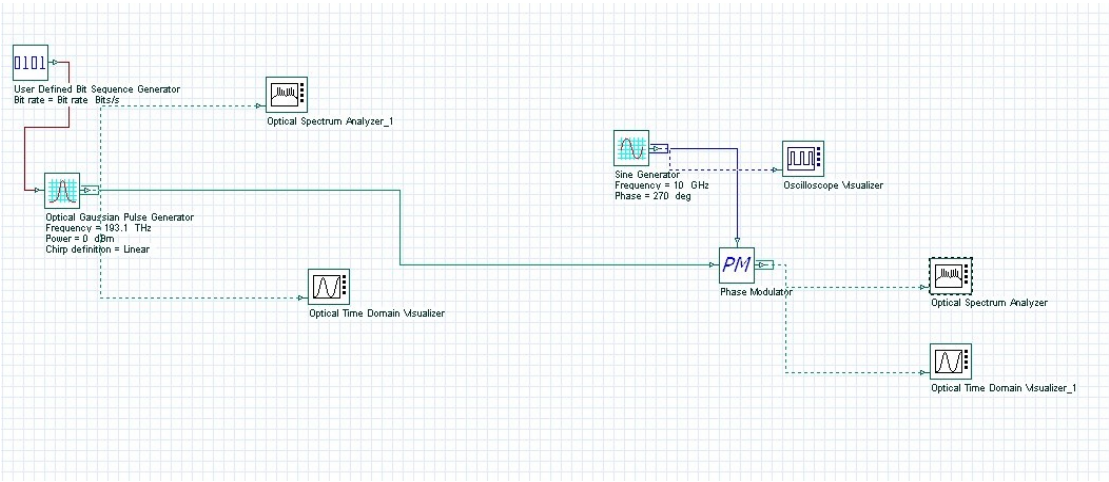

Figure 2.2 OptiSystem™ Setup for measuring the four spectra

Case	Description
1	The measurements are made directly after the pulse generator.
2	The pulse has a 2 rad/s chirped Gaussian pulse.
3	The pulse has a -2 rad/s chirped Gaussian pulse.
4	A 1 km length of fiber is added before the phase modulator. The dispersion of the fiber is 20 ps/km/nm.
5	The dispersion of the fiber is 40 ps/km/nm and the rest is the same as Case 4.
6	The dispersion of the fiber is 80 ps/km/nm and the rest is the same as Case 4.
7	A 1 km length of fiber is added before the phase modulator. The dispersion of the fiber is zero and the nonlinear coefficient is 1.3 $W^{-1}km^{-1}$.
8	The nonlinearity of the fiber is 5.1 $W^{-1}km^{-1}$ and the rest is the same as Case 7.
9	The peak power now is 30 dBm, the nonlinearity is 9.1 $W^{-1}km^{-1}$, and the rest is the same as Case 7.

Table 2.2 Summary of different cases

2.3.1 Cases

Case 1:

Figures 2.3 (a) and (b) show two sets of intensity and phase plots for Case 1. We use OptiSystem™ to simulate phase modulation and use the resulting data to calculate the intensity and phase information in MATLAB™. The original signal is acquired directly from the visualizer in OptiSystem™ before phase modulation. The recovered and original results have the same intensity of 1 mW and the same pulse width of 25 ps. Both exhibit zero phase in the time domain.

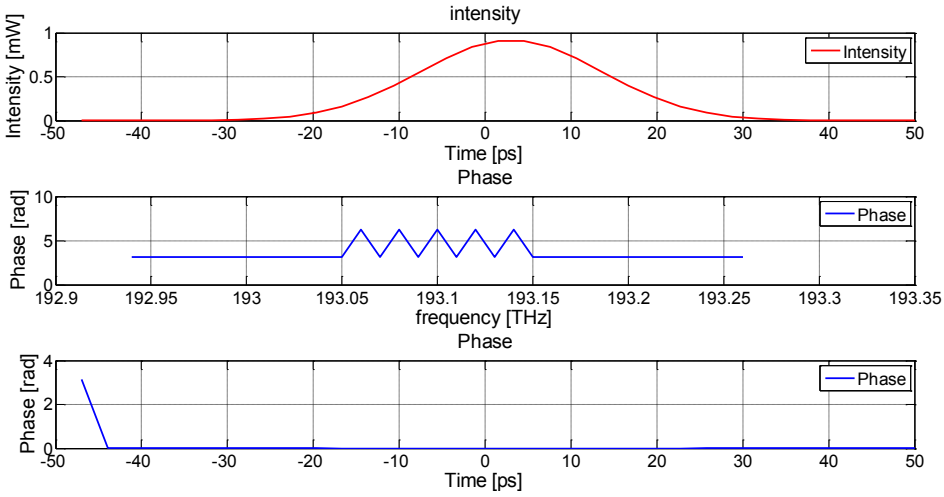

Figure 2.3 (a) Original signal intensity and phase information from OptiSystem™

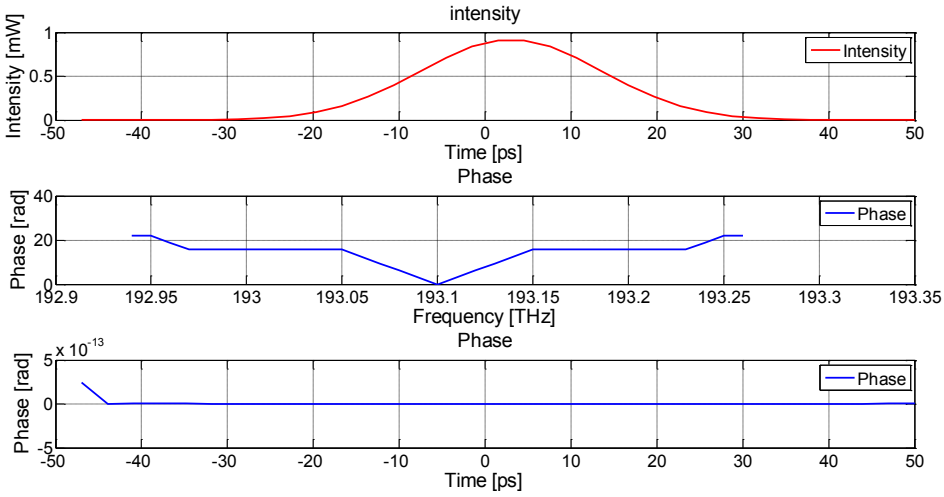

Figure 2.3 (b) Recovered signal intensity and phase information from MATLAB™

Case 2:

Figures 2.4 (a) and (b) show the results for Case 2. Again, the recovered and the original results have the same peak power of 1 mW and pulse width of 25 ps. They also have similar shape for phase profiles in both the frequency and time domains, with the difference in magnitude baring a $2n\pi$ phase shift. For the 2 ps/nm chirped Gaussian pulse, the curve of the phase profile is face upward and exhibits a positive

linear chirp. The slope of the chirp for both the recovered and original results are measured to be 1 $\times 10^{22}$ rad/s^2.

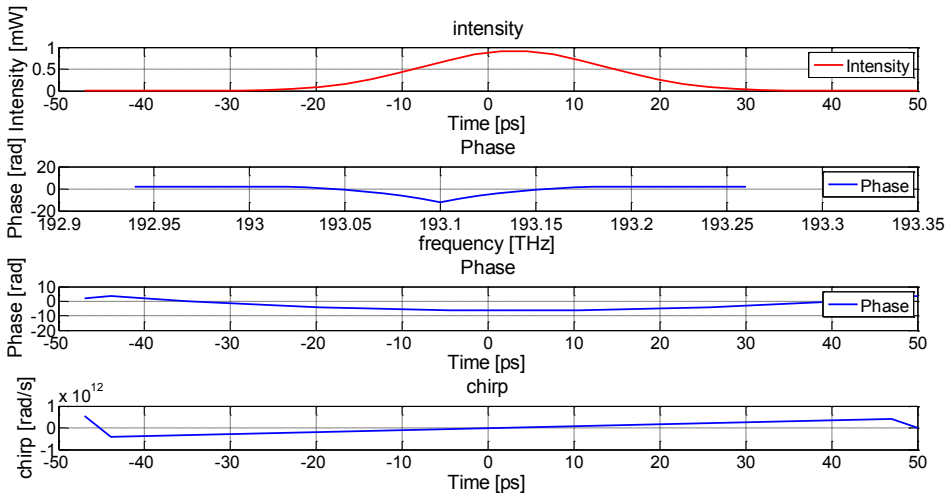

Figure 2.4 (a) Original signal intensity and phase information from OptiSystem™

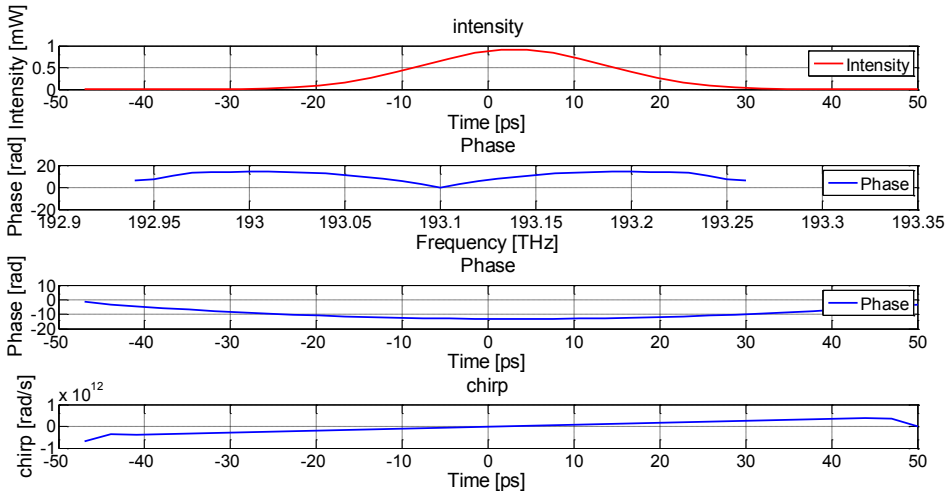

Figure 2.4 (b) Recovered signal intensity and phase information from MATLAB™

Case 3:

Figures 2.5 (a) and (b) show the results when the input signal has a -2 rad/s. The peak power is 1 mW and pulse width is 25 ps. The phase profiles in both the frequency and time domains have the same shape. Compared to Case 2, the curve of the phase now

faces downward and the slope of the chirp is now reversed. The chirp of the recovered and original results are both measured to be -1× 10^{22} rad/s^2.

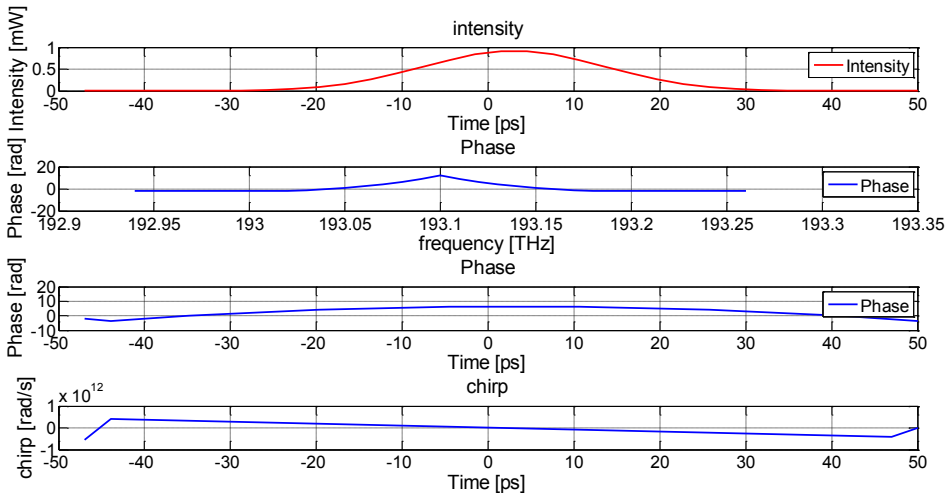

Figure 2.5 (a) Original signal intensity and phase information from OptiSystem™

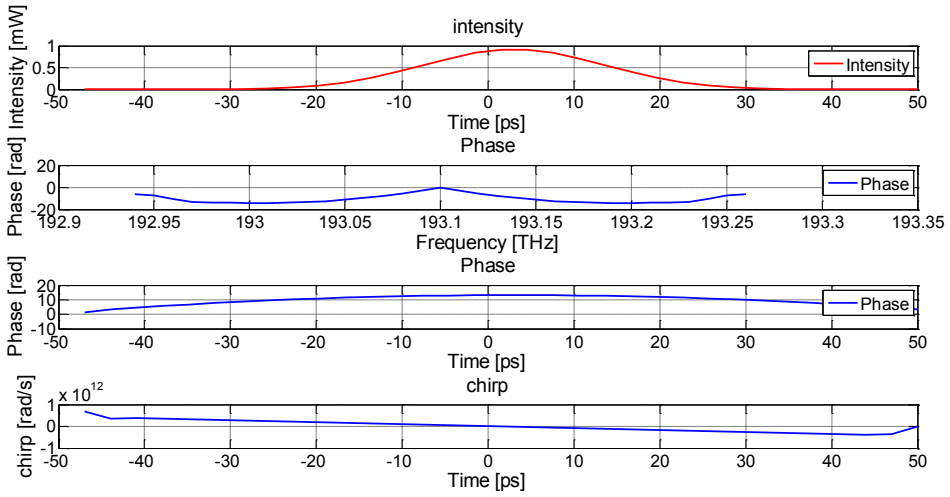

Figure 2.5 (b) Recovered signal intensity and phase information from MATLAB™

Cases 4 - 6:

From Case 4 to Case 6, the pulse propagates through a 1 km length of fiber with a dispersion of 20, 40, and 80 ps/nm/km, respectively. From Figures 2.6 (a) and (b), we can see that the amplitudes of the pulses in time domain are 1 mW and the pulse

widths are 25 ps. Compared to Case 2, the Gaussian pulse exhibits a linear chirp over the central portion of the pulse. The slope of the chirp is -5×10^{20} rad/s^2 for both plots. The phase and chirp change is due to the dispersion of the fiber.

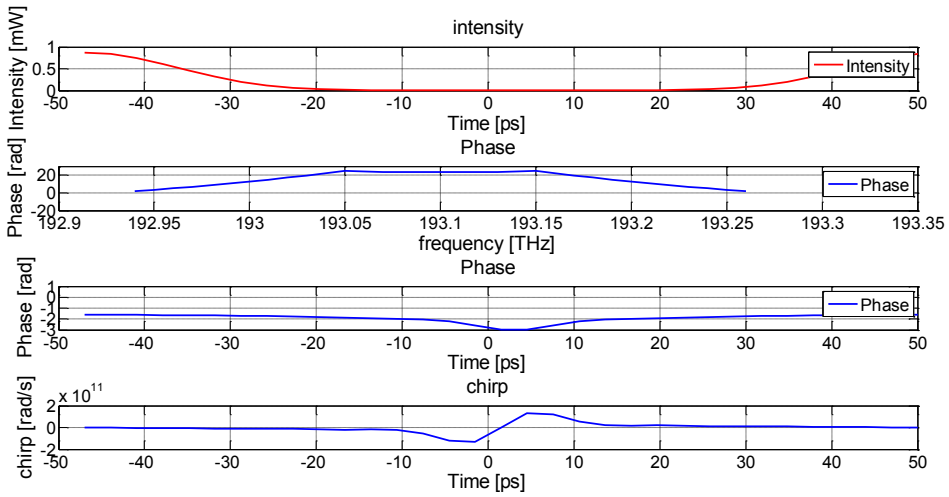

Figure 2.6 (a) Original signal intensity and phase information from OptiSystem™

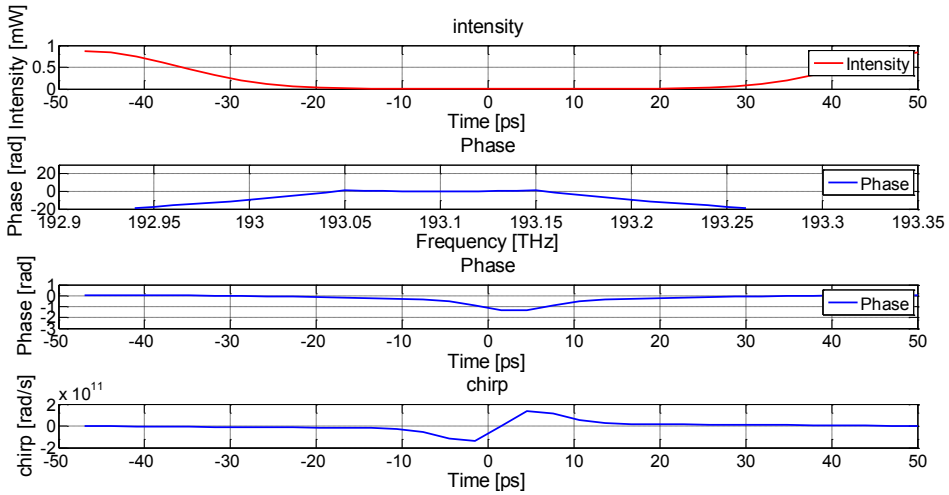

Figure 2.6 (b) Recovered signal intensity and phase information from MATLAB™

From Figures 2.7 (a) and (b) we can observe that the recovered and original signal intensities have the same peak power of 1 mW and pulse width of 25 ps. Compared to

Case 4 where the slope of the linear chirp has increased to -9.7 × 10^{20} rad/s^2, which is approximately two times greater as expected.

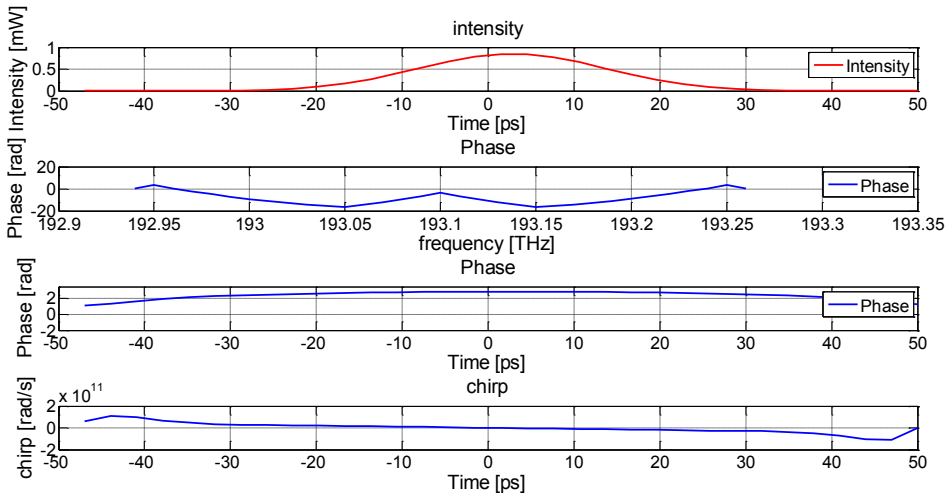

Figure 2.7 (a) Original signal intensity and phase information from OptiSystem™

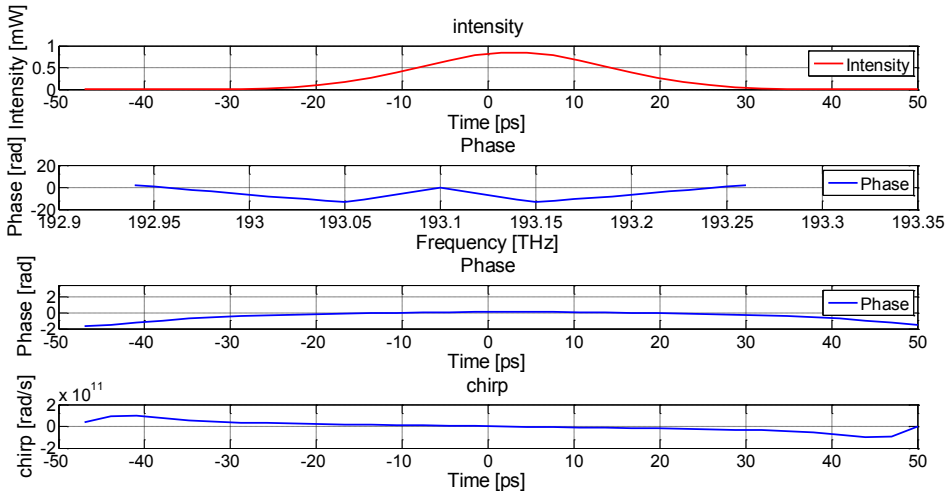

Figure 2.7 (b) Recovered signal intensity and phase information from MATLAB™

Case 6:

Figures 2.8 (a) and (b) show the results when the cumulating dispersion is 80 ps/nm. Compared to Case 5, the slope of the linear chirp in time domain is measured to be -1.7× 10^{21} rad/s^2 for both recovered and original results, which is two times greater, again as expected.

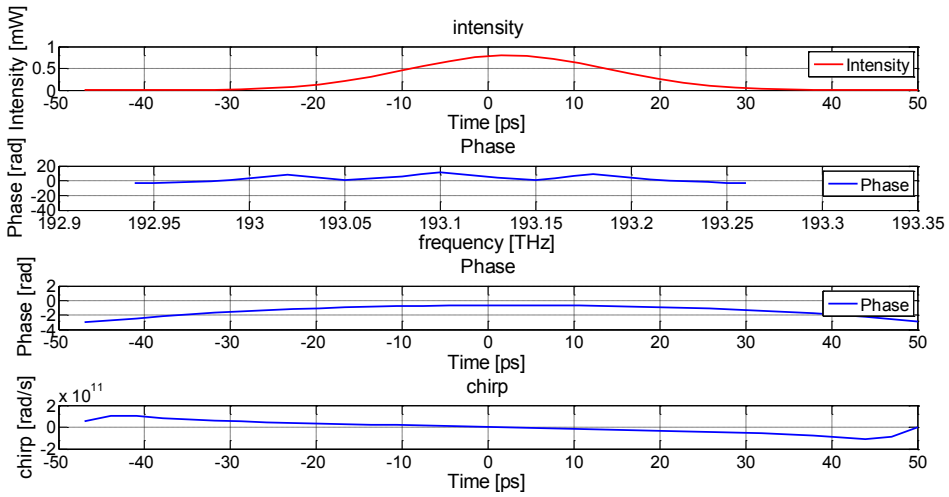

Figure 2.8 (a) Original signal intensity and phase information from OptiSystem™

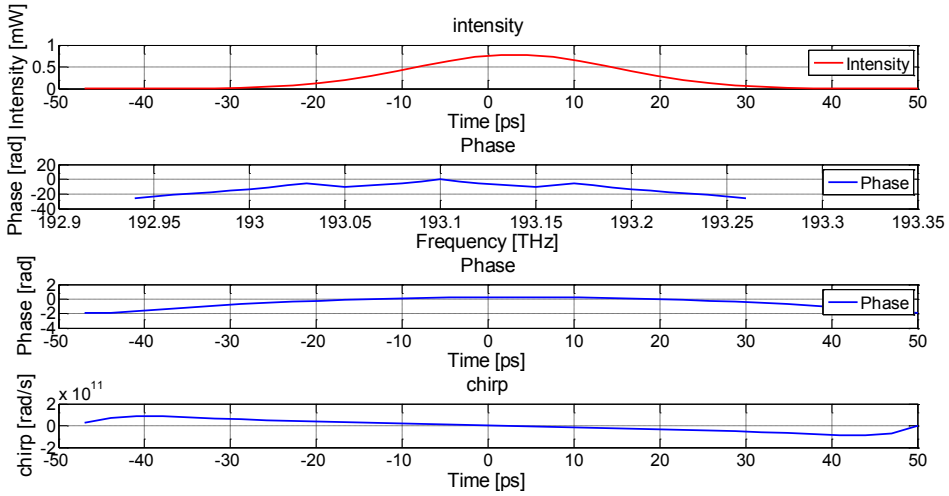

Figure 2.8 (b) Recovered signal intensity and phase information from MATLAB™

Case 7:

Now the pulse propagates through a 1 km length of fiber with a nonlinearity of 1.3 $W^{-1}km^{-1}$; the results are shown in Figures 2.9 (a) and (b). Compared to Case 1, the amplitude and phase profiles are similar; since the impact of nonlinearity is small (due to the relatively low peak power).

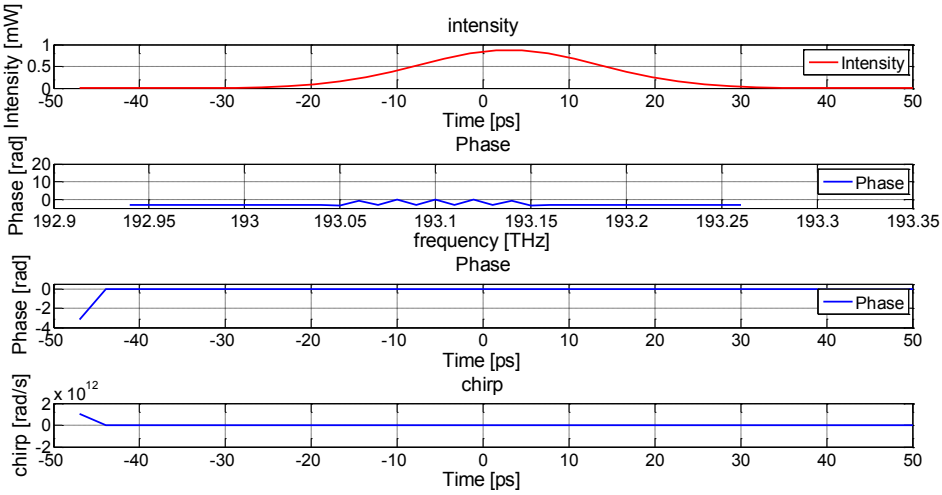

Figure 2.9 (a) Original signal intensity and phase information from OptiSystem™

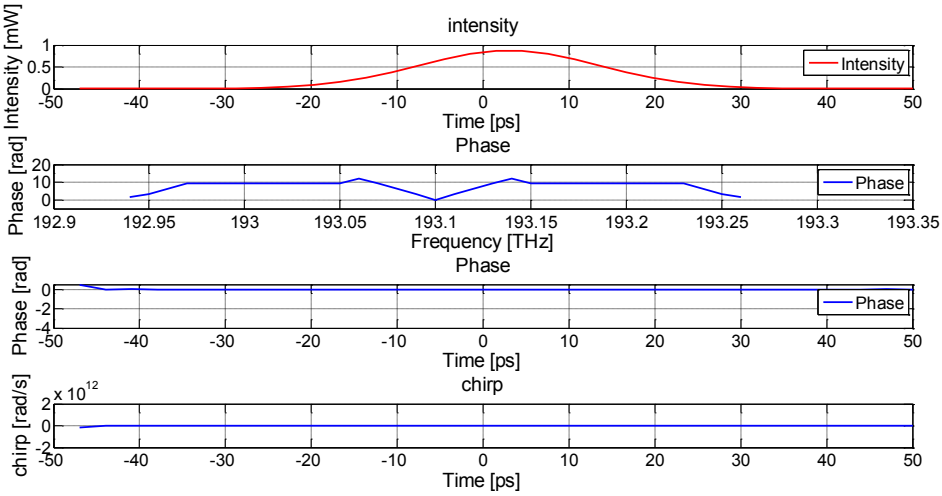

Figure 2.9 (b) Recovered signal intensity and phase information from MATLAB™

Case 8:

Figures 2.10 (a) and (b) show the results with a nonlinearity of 5.3 $W^{-1}km^{-1}$. We still cannot observe any obvious change due to nonlinear effects although the nonlinearity has been increased.

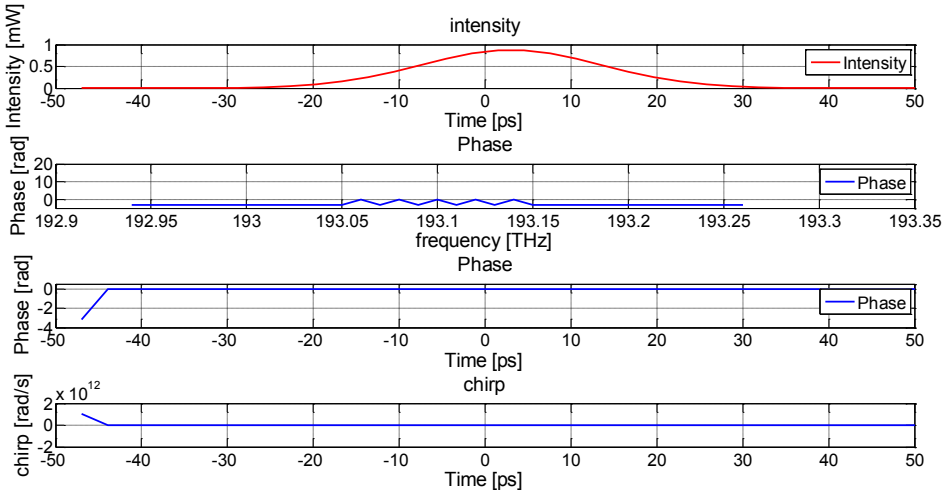

Figure 2.10 (a) Original signal intensity and phase information from OptiSystem™

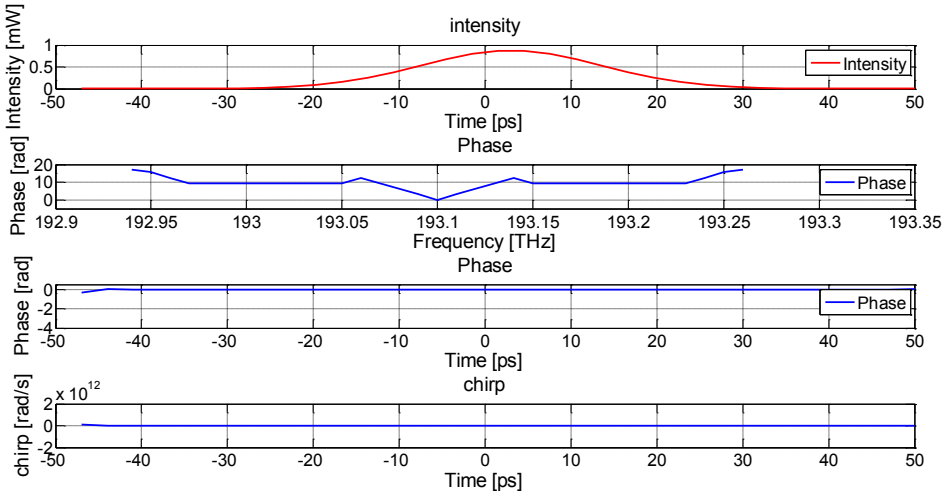

Figure 2.10 (b) Recovered signal intensity and phase information from MATLAB™

Case 9:

The peak power of the input signal is now increased to 30 dBm and the fiber nonlinearity is now increased to 9.1 $W^{-1}km^{-1}$. The results are shown in Figures 2.11 (a) and (b). There is a small difference in the shape of the intensity envelope, but the peak powers are the same ~ 1000 mW. There is also a phase change in the time domain, which results in a chirp for both plots. By observing the chirp, we can

conclude that the leading edge of the pulse is shifted to lower frequencies, while the trailing edge is shifted to higher frequencies. In the center of the pulse, the frequency shift is approximately linear. The linear chirp in the center of the pulse is measured to be 6×10^{22} rad/s for both plots. The phase change and frequency shift due to self-phase modulation (SPM) effect is expected since we increased both the nonlinearity of the fiber as well as the peak power.

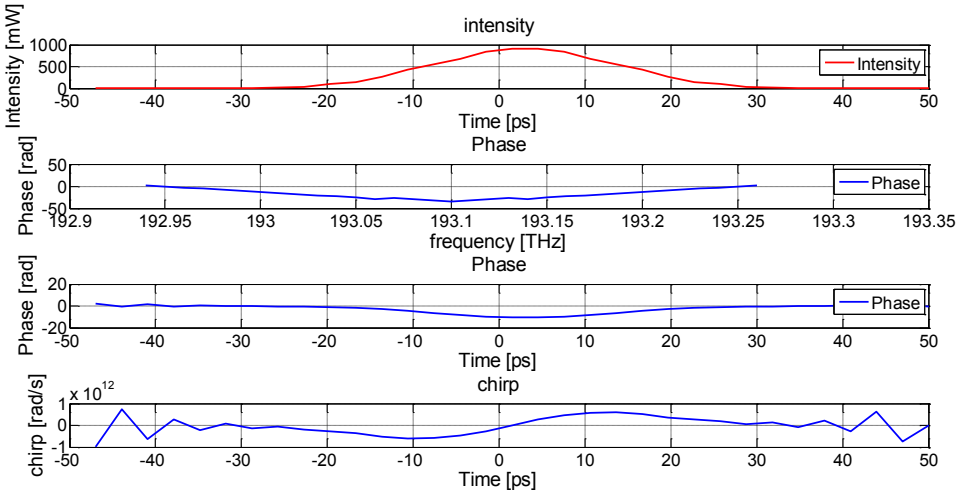

Figure 2.11 (a) Original signal intensity and phase information from OptiSystem™

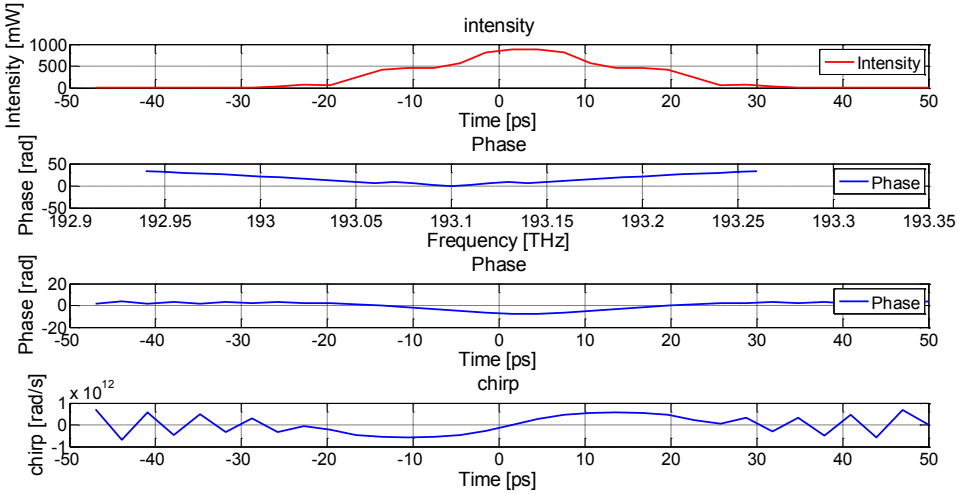

Figure 2.11 (b) Recovered signal intensity and phase information from MATLAB™

2.3.2 Summary

From Case 2 and Case 3, we can conclude that the pulse characterization technique can detect the chirped Gaussian pulse very well. Cases 4 - 6 show that the technique is capable of characterizing pulses with accumulated dispersion. Case 9 shows that the technique is reliable to detect nonlinear-induced phase changes.

2.4

Experiment

Next, we demonstrate the proposed method experimentally. Figure 2.12 shows the experimental setup. The pulse is generated by modulating the laser using an intensity modulator with a 2.5 GHz clock. The signal is phase-modulated with a phase modulator driven by the same clock at 2.5 GHz. An attenuator is used after the synthesizer to limit the amplified voltage in order to have V_π or lower. Figure 2.13 shows the original signal in yellow; the green signal is the sinusoidal signal used for modulation.

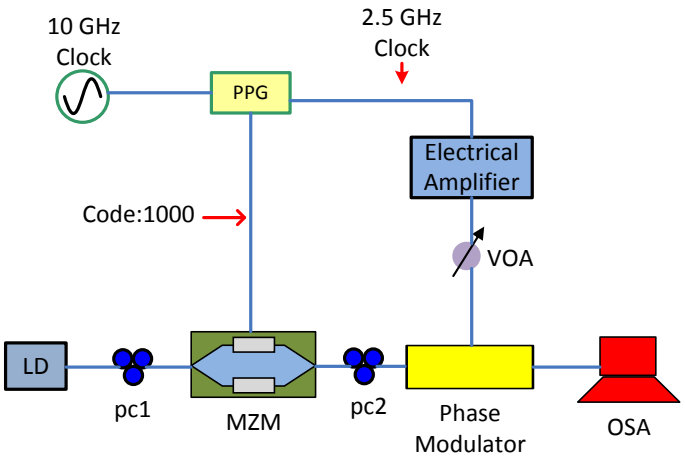

Figure 2.12 Experimental setup for pulse characterization.

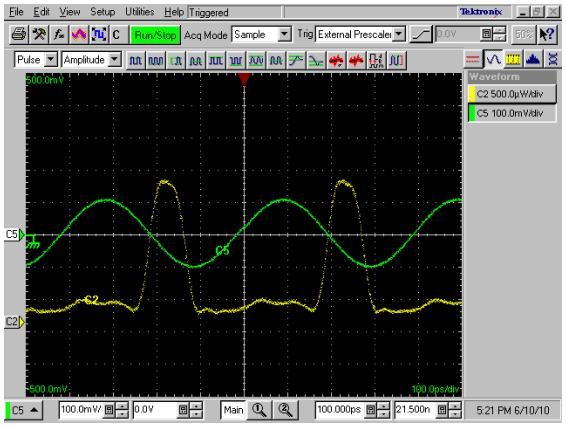

Figure 2.13 Original signal is shown in yellow and green is the sinusoidal signal for modulation.

An OSA with a resolution of 20 MHz is used to record the pulse spectra after the phase modulator. The span of the OSA is 250 GHz, and we record the spectrum using 100 points and 1000 points. The original pulse spectra intensity is directly measured by the OSA with the phase modulator turned off. The modulation amplitude used is $\frac{1}{6}V_\pi$ (0.5236 radians). With these two sets of data, the phase information in frequency can be recovered. The pulse intensity and phase versus time was then calculated by the pulse characterization technique described in Section 2.2; the results are shown in Figures 2.14 (a) and (b). Figure 2.14 (a) is the pulse intensity envelope and phase information in both the frequency and time domains recovered using the 100 steps. The peak power of the recovered pulse is 1.8 mW, which is the same as the original signal shown in Figure 2.13. The pulse width of the recovered pulse is around 100 ps, which is also the same as the original signal. There is a linear chirp of 7.4×10^{20} rad/s^{2}measured at the edge of the pulse. The linear chirp measured is the same as that obtained by Kim and Gnauck in [42], and is caused by the MZM. Figure 2.14 (b) shows the recovered pulse shape and phase using 1000 points. The recovered pulse shape is a train of 10 pulses and the recovered phase is the accumulated phase of 10 pulses.

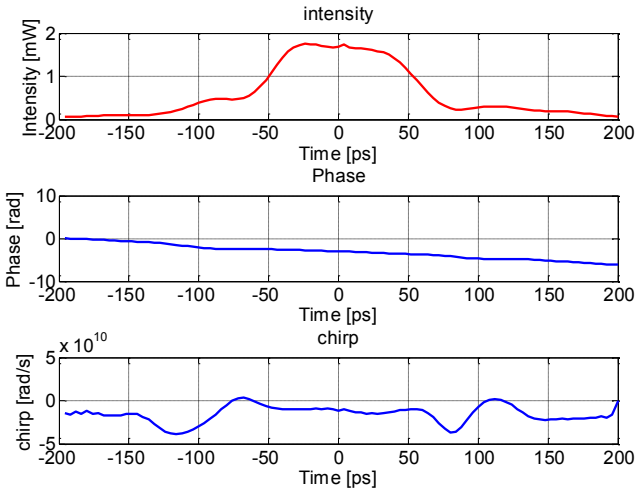

Figure 2.14 (a) Recovered signal intensity and phase information with 100 steps.

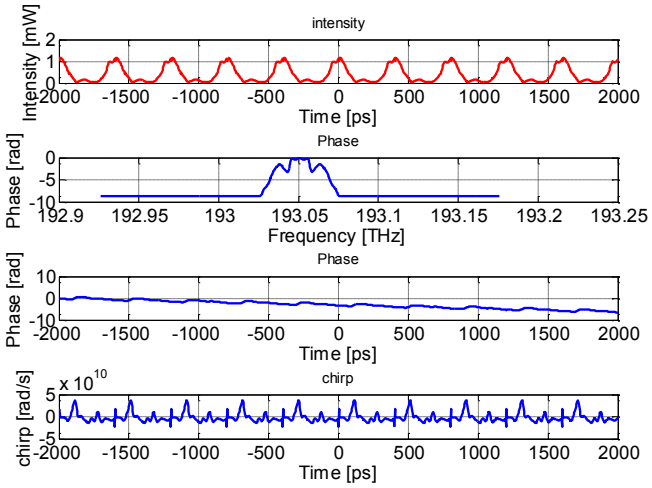

Figure 2.14 (b) Recovered signal intensity and phase information with 1000 steps.

2.5

Summary

We have simulated the linear-spectrographic technique under various conditions. We proved that this technique is capable of characterizing pulses with various amount of accumulated dispersion or nonlinear-induced phase change. The method is experimentally verified as well.

Chapter 3

Analysis of All Optical OOK to DPSK Modulation Format Conversion at 10 Gb/s

3.1

Introduction

Recently, researchers have proposed and demonstrated a variety of schemes for all optical format conversion between OOK and DPSK. These methods employ either SOAs [27][28], HNLF [29][30], or a passive nonlinear semiconductor waveguide [44]. Using XPM in optical fiber is more attractive since the SOAs suffer from residual cross-gain modulation and a CW assist light is required to overcome the slow response time. The disadvantage of silica fiber and waveguide are the high power level that is required. OOK to DPSK format conversion has been demonstrated only for an input NRZ signal at a fixed wavelength, and the subsequent performance of the

conversion with signal degradation has not been investigated. In this chapter, a detailed characterization of the conversion is presented by simulation. The simulation is carried out by OptiSystem™. We present a direct comparison between simulation and experimental results for the dependence of the receiver sensitivity (which is the average received power needed for a BER of 10^{-9}) on important properties of the input signal. These properties include the duty cycle, peak power, state-of-polarization, OSNR, residual group velocity dispersion, and PMD. By knowing the optimized parameters, we then implemented an OOK to DPSK format conversion scheme capable of wavelength multicasting.

3.2

Principle of Operation

3.2.1 RZ-OOK to RZ-DPSK Format Conversion

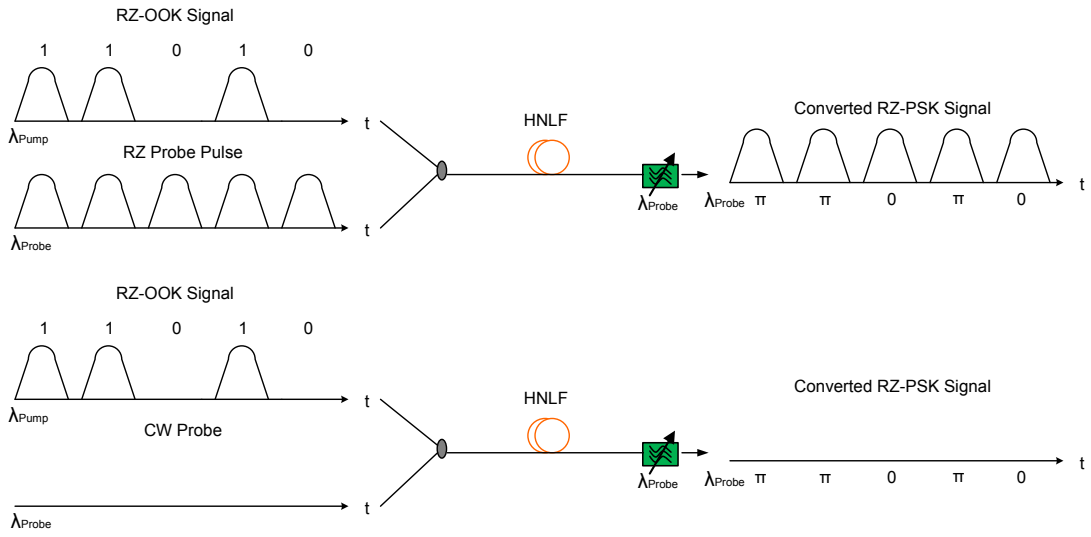

Figure 3.1 Configuration of RZ-OOK to DPSK conversion (top: RZ probe, bottom: CW probe)

Figure 3.1 shows the basic ideas of the RZ-OOK to RZ-DPSK conversion. A strong RZ-OOK pump at wavelength λ_{Pump} and a weak probe pulse (either RZ or CW) at wavelength λ_{Probe} are coupled into a length of HNLF where XPM takes place. A

filter is placed at the end of the fiber to filter out the converted PSK signal at λ_{Probe}. The phase change of the probe is described by

$$\Delta\phi_{probe} = 2\gamma L_{eff} P_{pk} \qquad (3.1)$$

where γ is the nonlinear parameter of the HNLF, L_{eff} is the effective interaction length of the HNLF, and P_{pk} is the peak power of the pump pulse. Thus, the peak power of the pump signal is calculated and adjusted to provide the desired phase shift. For the case of RZ-DPSK, the 0 or π phase shift corresponds with a "0" bit or "1" bit of the RZ-OOK signal, respectively.

3.2.2 NRZ-OOK to RZ-DPSK Format Conversion

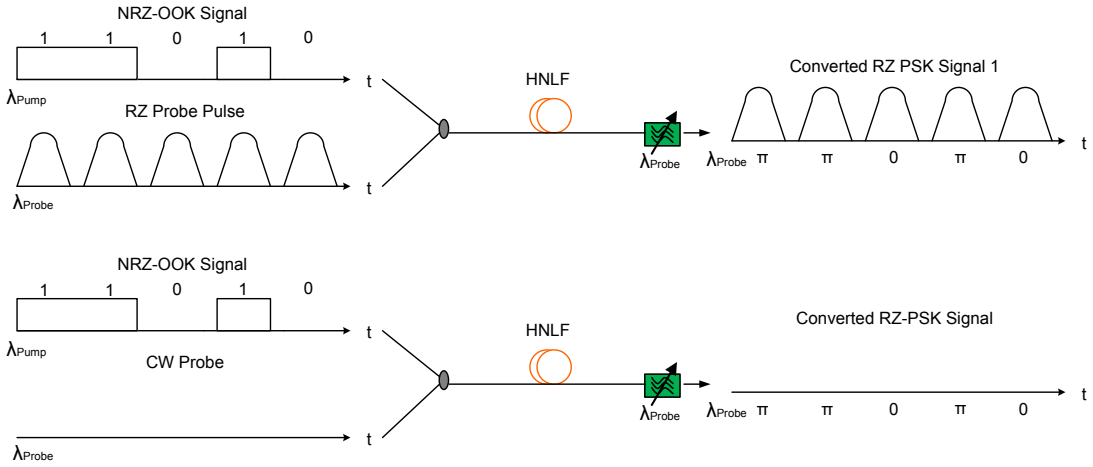

Figure 3.2 Configuration of NRZ-OOK to DPSK conversion (top: RZ probe [29], bottom: CW probe).

Figure 3.2 shows the basic idea of the NRZ-OOK to RZ-DPSK conversion, which is similar to the RZ-OOK to RZ-DPSK conversion. However, according to Eq. 3.1, the phase shift due to XPM is proportional to the peak power of the pump; thus, an NRZ-OOK pump requires a much higher average power than an RZ-OOK pump to achieve the same phase shift. The high pump power causes unwanted nonlinear effects, such as parametric amplification and stimulated Brillouin scattering (SBS). These effects

severely degrade the format conversion process. Thus, for the purpose of our investigation, we only consider an RZ-OOK pump.

3.3
Simulation results and analysis

All of the simulations are carried out in OptiSystem™ and operate at 10 Gb/s. As shown in Figure 3.1, the probe signal can be either an RZ pulse or a CW laser; simulations are done for both cases for comparison. Figure 3.3(a) shows the screenshot from OptiSystem™ and (b) shows the schematic diagram. The RZ-OOK pump is generated by a CW laser modulated by a PRBS Gaussian pulse generator using a MZM. The short bit length of 2^5 is due to the limitation of OptiSystem (it cannot measure the BER when the bit length is larger). The RZ probe is generated by an optical Gaussian pulse generator and the CW probe is generated by a CW laser. The pump and probe are coupled and propagate in the HNLF. The SBS is considered in the HNLF with a typical frequency shift of 11 GHz and a gain constant of 46×10^{-12} m/W; Rayleigh scattering is considered as well. Both the pump signal and the probe signal, as well as the output after HNLF, are amplified by an EDFA with a noise figure of 5 dB. An optical Gaussian filter with a bandwidth of 0.4 nm is used to filter out the noise from the EDFA. A delay line interferometer (DLI) is used for demodulation with an free spectral range (FSR) of 10 GHz. The photodetector (PD) responsivity is 1 A/W with a dark current of 10 nA; shot noise, thermal noise (100×10^{-24}W/Hz), signal-ASE noise, and ASE-ASE noise are all considered. Each PD is followed by an electric low-pass filter with a cut-off frequency of $0.8B$, where B

is the bit rate. We use the receiver sensitivity for graphically showing the impact from signal degradation. The BER is measured from the BER analyzer and the received power is recorded by an optical power meter placed at the optical output.

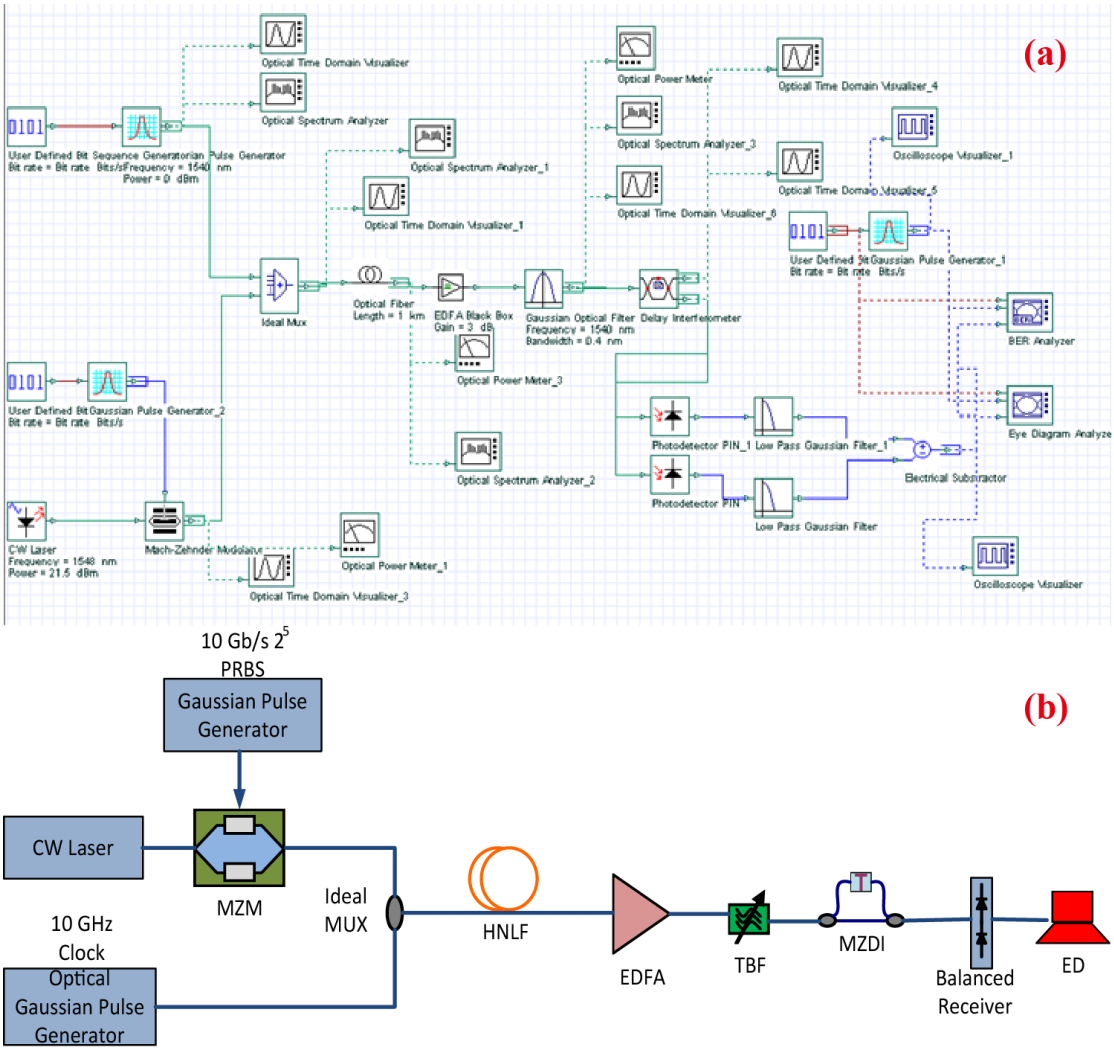

Figure 3.3 OptiSystem™ setup for the RZ-OOK to DPSK simulation. (a) Software screenshot and (b) schematic diagram.

3.3.1 Overview

Figure 3.4 (a) shows an example of a converted RZ-DPSK signal (using an RZ probe and an ideal RZ-OOK pump) versus an RZ-DPSK generated directly. We can see that the conversion is almost perfect except for some amplitude fluctuations. Figure 3.4 (b) compares the corresponding optical spectra.

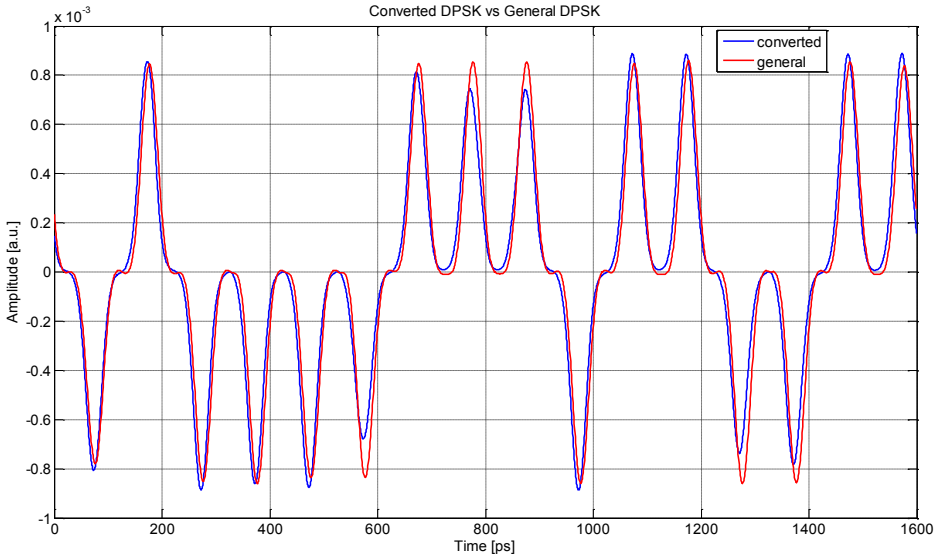

Figure 3.4 (a) converted DPSK versus general DPSK.

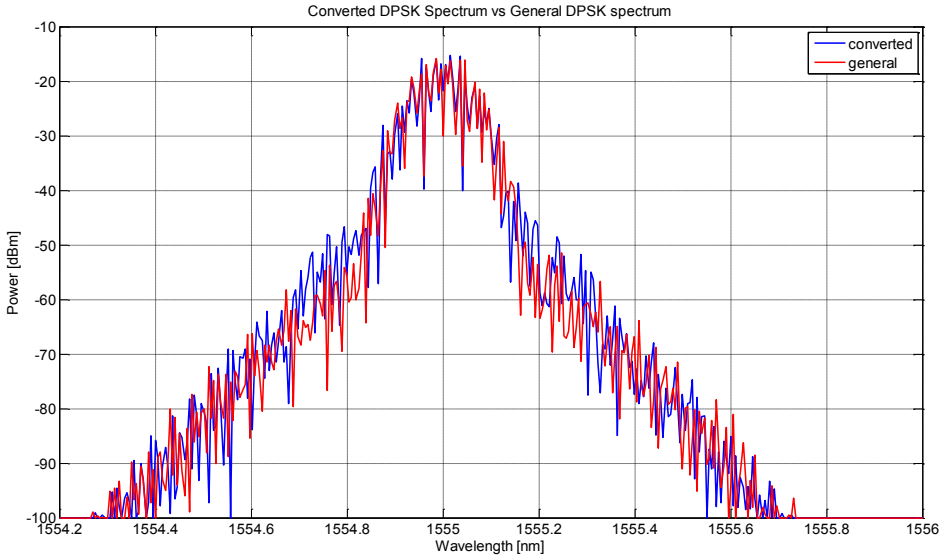

Figure 3.4 (b) converted DPSK versus general DPSK.

3.3.2 Parameters of the HNLF

The parameters of the HNLF are given in Table 3.1. These correspond to the parameters of the HNLF available in the lab and used in the experiments.

Fiber	Length [m]	Nonlinearity coefficient[$W^{-1}km^{-1}$]	Chromatic Dispersion @1550nm[ps/nm/km]	Dispersion slope @1550nm[ps/nm^2/km]
HNLF	1007	11.5	-0.71	0.01

Table 3.1 Parameters of HNLF at 1550nm

In the simulation, we set the effective area of the fiber to be 11.5 μm^2 and n_2 to be 30× 10^{-21} m^2/W, which give us a nonlinear coefficient of 11.5 $W^{-1}km^{-1}$. The zero dispersion wavelength of the HNLF was 1600 nm to minimize parametric amplification between the two signals. The slope of the dispersion curve is relatively low to provide small dispersion differences between various wavelengths. Thus, the relative wavelength spacing between the probe signal and the pump signal are more important than the exact wavelengths used.

3.3.3 Pump Power

According to the HNLF parameters, the pump peak power to acquire π phase shift is estimated to be 21.5 dBm, which is calculated using Eq. (3.1).

3.3.4 Pump and probe wavelength

In this section, we examine the change of the receiver sensitivity due to the change of wavelength spacing.

a) RZ Probe

We first consider the case when the probe is an RZ pulse. We fix the pump wavelength at 1550 nm and we always keep the peak power at 21.5 dBm (optimized in OptiSystem™ using the optimization function, *i.e.*, a simulation loop to find the

optimum peak power, which is also close to our calculation). The duty cycle of the pump is 40% while the duty cycle of the probe is 33%.

Figure 3.5 shows that as long as the probe wavelength is either less than 1546 nm or larger than 1554 nm, the format conversion can be achieved with error-free performance. For a probe wavelength of 1545 nm to 1554 nm, the parametric amplification distorts the pulse and results in a closed eye so that error-free operation cannot be obtained. The lowest receiver sensitivities are acquired when the probe wavelength is around 1541 nm or 1555 nm.

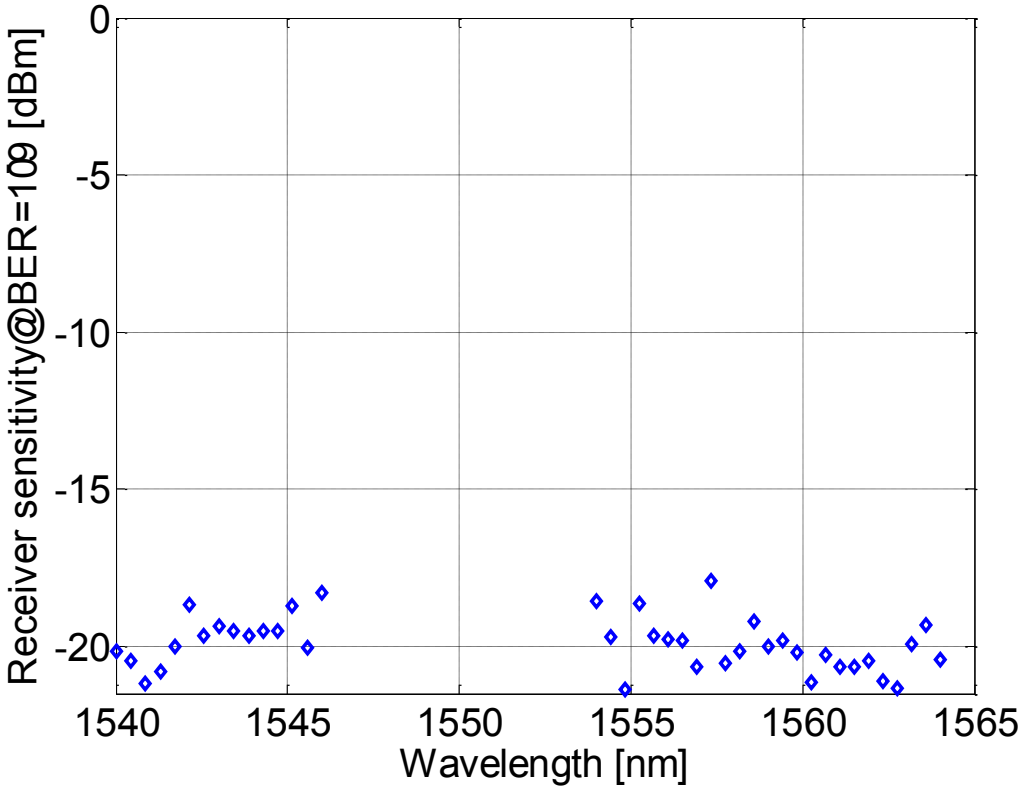

Figure 3.5 Receiver sensitivity as a function of probe wavelength for an RZ pump at 1550 nm.

We then change the pump wavelength to 1555 nm and repeat the simulation while keeping all other parameters the same. From Figure 3.6, we can observe that the probe wavelength needs to be either less than 1551 nm or larger than 1559 nm for error-free format conversion. The lowest receiver sensitivity is acquired when the probe

wavelength is around 1541 nm. Comparing the results from Figures 3.5 and 3.6, we can see that as long as the wavelength spacing $\Delta\lambda = \lambda_{Pump} - \lambda_{Probe}$ is more than 4 nm, the format conversion functions properly. Also, the lowest receiver sensitivities for both plots are quite similar, around -22 dBm.

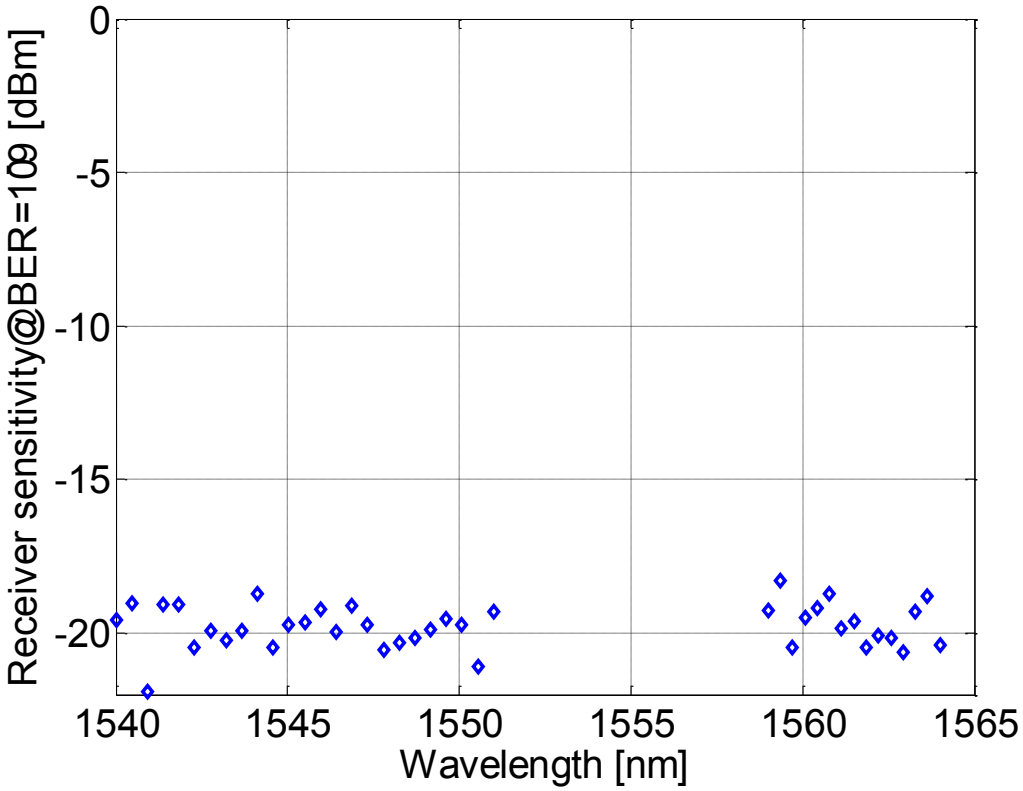

Figure 3.6 Receiver sensitivity as a function of probe wavelength for an RZ pump at 1555 nm.

To have a much clearer view of the impact of wavelength spacing between pump and probe, we plot the receiver sensitivity as a function of pump peak power for $\Delta\lambda$ of 5 nm, 10 nm, 14 nm, and 15 nm (the pump is fixed at 1555 nm). From Figure 3.7, we can observe that the four different spacing sets have similar saddle-like traces and the performance of the conversion does not differ very much between three of them (only the $\Delta\lambda = 5$ nm is the different variation). The minimum receiver sensitivity is obtained for $\Delta\lambda = 10$ nm. However, the minimum received power requires a peak power of over 23 dBm. When the power is higher, the SBS is more significant, which

results in a reduction of forward pump power. Based on these simulations, the probe wavelength should be kept around 1541 nm and the pump wavelength around 1555 nm, with a pump power of 21.5 dBm, which is close to the estimate given in section 3.3.3.

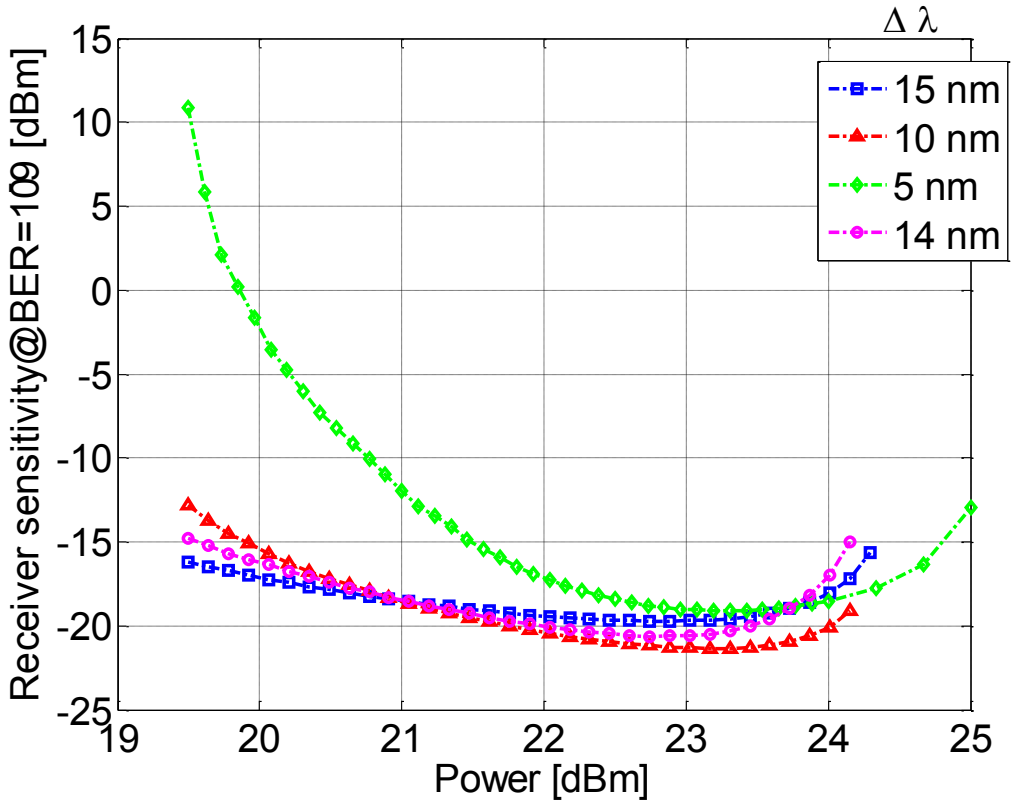

Figure 3.7 Receiver sensitivity plot versus pump peak power when probe is RZ

b) CW Probe

Next, we consider the case when the probe is a CW signal. The pump peak power and duty cycle are the same as in the RZ probe case. We fix the pump wavelength at 1550 nm and vary the probe wavelength and plot the receiver sensitivity.

From Figure 3.8, we can observe that the minimum received power to have a BER of 10^{-9} is acquired when the probe wavelength is around 1541 nm and 1558 nm, which

is similar to the RZ probe case. The receiver sensitivity is around -19 dBm which is 3 dB worse than the RZ probe case.

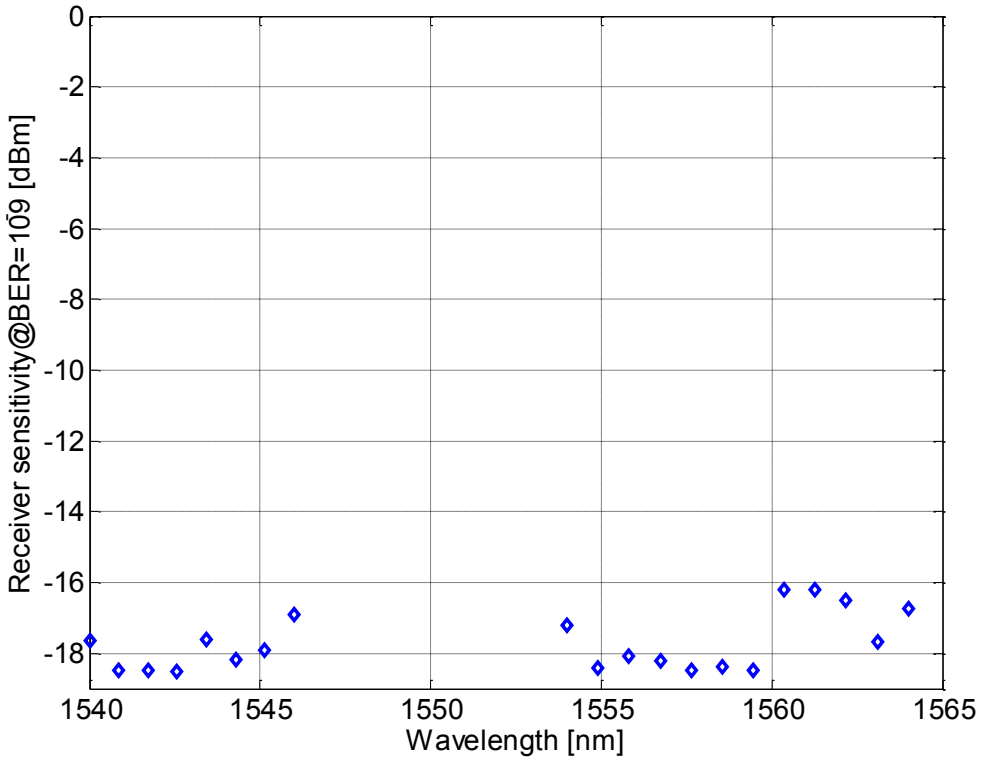

Figure 3.8 Receiver sensitivity as a function of CW probe wavelength for an RZ pump at 1550 nm

We then change the pump wavelength to 1545 nm and repeat the simulation while keeping all other parameters the same.

From Figure 3.9, we can observe that the minimum received power to have a BER of 10^{-9} (~ -19 dBm) is acquired when the pump wavelength is around 1554 nm or 1561 nm. Comparing the two plots, we can easily see that the requirements for using a CW probe are similar to an RZ probe, which is that $\Delta\lambda$ should be more than 4 nm.

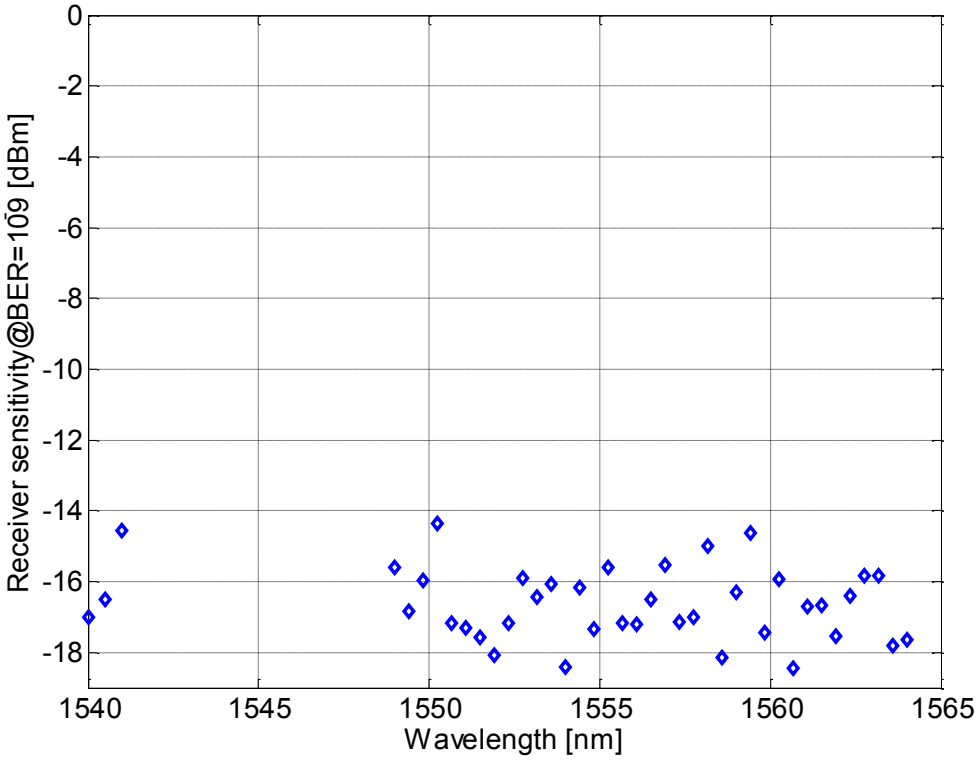

Figure 3.9 Receiver sensitivity as a function of CW probe wavelength for an RZ pump at 1545 nm

The receiver sensitivity as a function of pump power is also plotted for different values of Δλ (λ_{Pump} is fixed at 1555 nm), see Figure 3.10. The plots exhibit the same trends as in the case of an RZ probe. The minimum receiver sensitivity is acquired when $\Delta\lambda = 14$ nm. The CW probe results match those of an RZ probe with the only difference being a 3 dB penalty in receiver sensitivity.

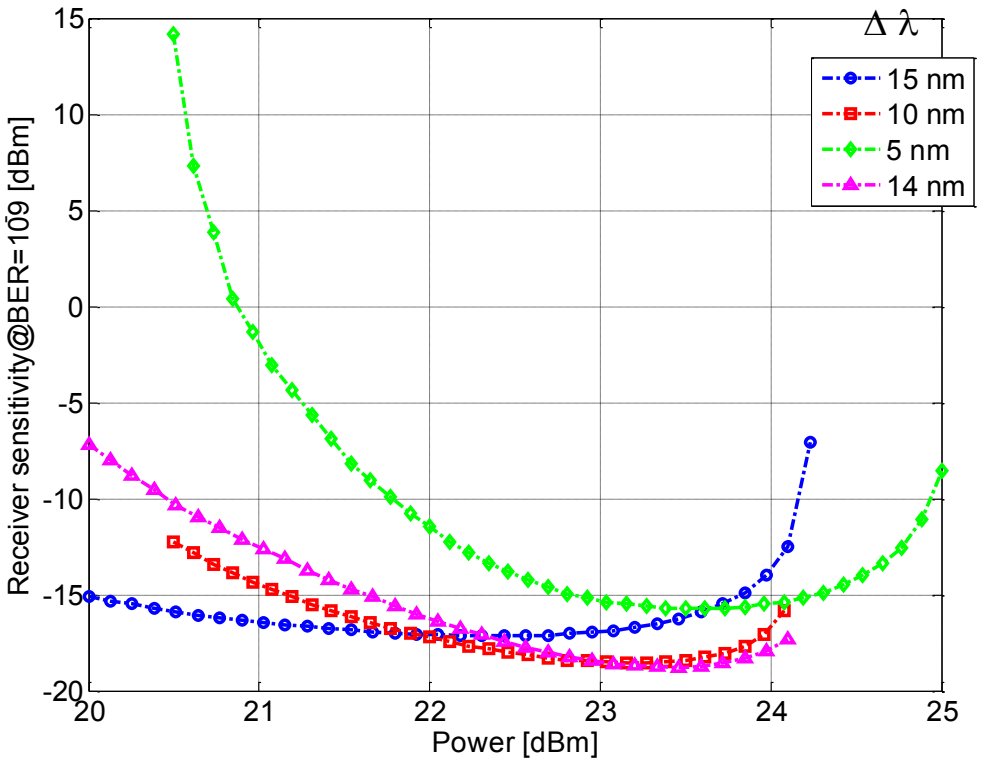

Figure 3.10 Receiver sensitivity plot versus pump power when probe is CW

After investigating the impact of pump and probe wavelengths, we determine the dependence of the quality of the converted signal on important properties of the input data signal, such as the duty cycle, state of polarization, PMD, OSNR, and residual dispersion. We also investigate the impact of the FSR of the DLI used at the receiver. For each case, we plot the receiver sensitivity to quantify the conversion performance.

3.3.5 Duty Cycle

If not mentioned specifically, the RZ probe has a wavelength of 1541 nm, duty cycle of 33%, and a peak power of 0 dBm. The CW probe has a wavelength of 1541 nm and a peak power of 0 dBm. The RZ-OOK pump has a duty cycle of 40%, a wavelength of 1555 nm, and a peak power of 21.5 dBm. The reason we chose the probe

wavelength to be 1541 nm and pump wavelength to be 1555 nm has been discussed previously: this results in a wavelength spacing larger than 4 nm and the lowest receiver sensitivity.

a) RZ Probe case

First, we want to determine whether or not the duty cycle of the RZ probe pulse has an impact on the format conversion performance. The peak power is fixed at 0 dBm. Figure 3.11 shows that, as the duty cycle of the probe pulse increases, the received power increases, which is equivalent to a decrease in the conversion performance. Ideally, the RZ probe should be shorter than the pump pulse to operate the full nonlinear phase change over the pulse duration.

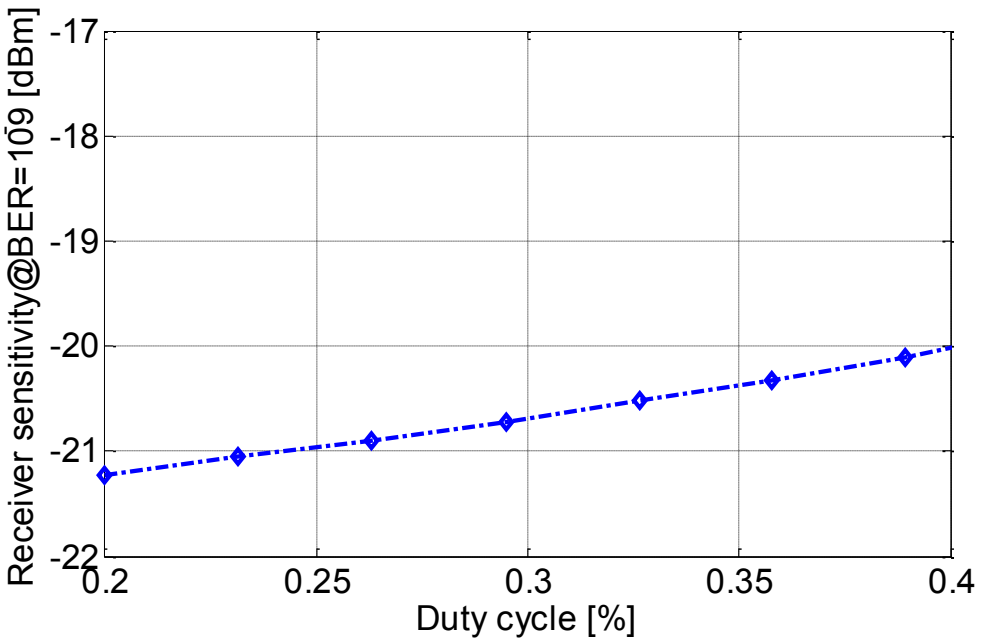

Figure 3.11 Receiver sensitivity plot versus probe duty cycle when probe is RZ

We next want to see whether or not the duty cycle of the pump pulse has an impact on the format conversion performance. Figure 3.12 shows that the receiver sensitivity initially decreases as the pump duty cycle increases up to around 40%, and then remains almost constant until 80%. The peak power of the RZ-OOK signal is kept

constant at 21.5 dBm. Therefore, the average optical power varies with the duty cycle. At a duty cycle of around 40% or 80%, the system has the best performance of XPM. But changing the duty cycle does not degrade the performance significantly as long as the duty cycle of the pump is larger than the duty cycle of the probe.

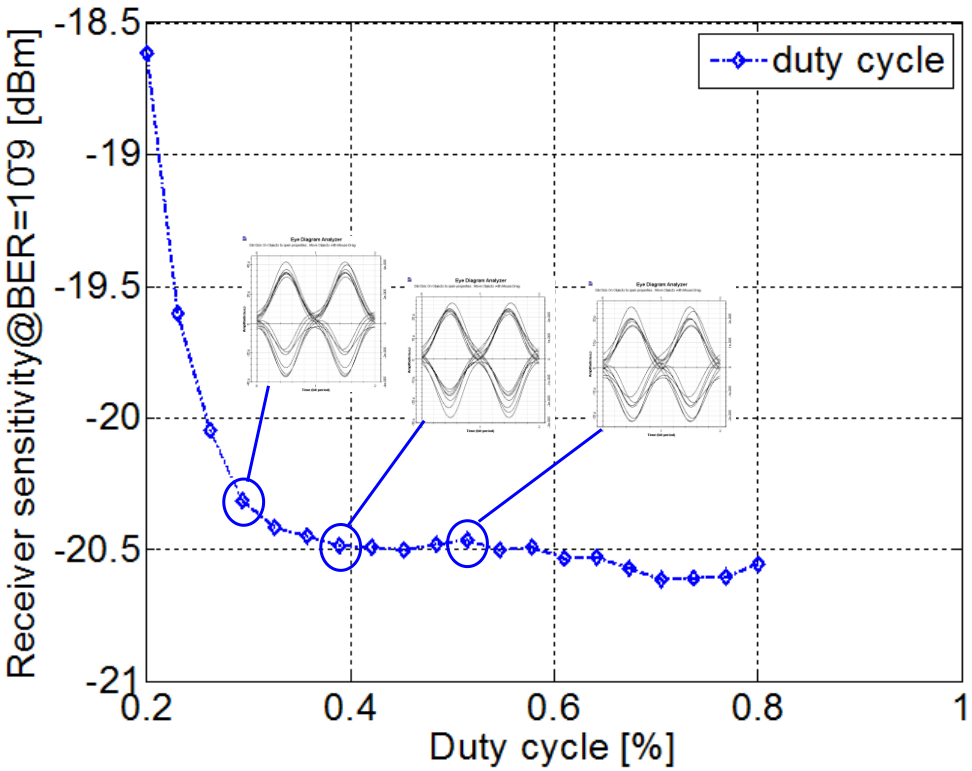

Figure 3.12 Receiver sensitivity plot versus pump duty cycle when probe is RZ

b) CW Probe case

For the CW probe case, we only plot the receiver sensitivity as a function of the duty cycle of the pump pulse. By observing Figure 3.13, we can see that the performance of the format conversion improves as the pump duty cycle increases up to around 50%, then worsens as the pump duty cycle continuously increases to 68%; the performance improves again for duty cycles up to 80%. The two optimal receiver sensitivities are around -18 dBm, while the worst is at around -16.5 dBm. The results show that

changing the pump duty cycle when using a CW probe has a greater impact on performance compared to using an RZ probe.

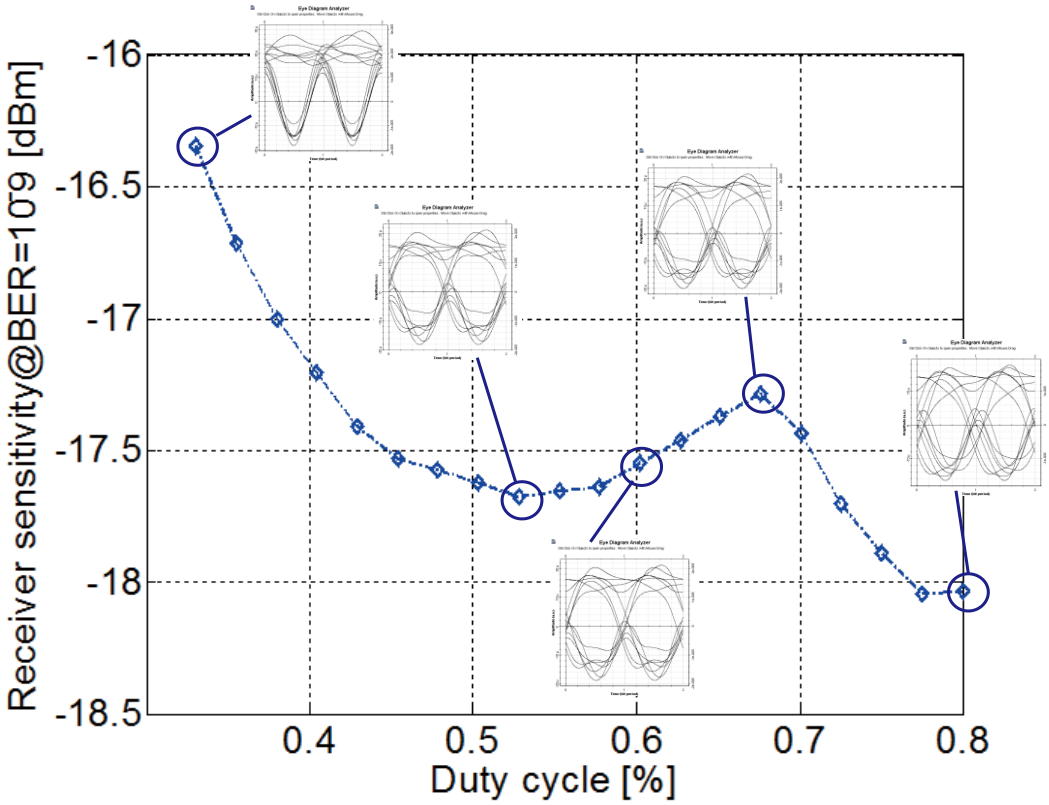

Figure 3.13 Receiver sensitivity plot versus pump duty cycle when probe is CW

3.3.6 State of Polarization

XPM is polarization sensitive process. When the two input signals are co-polarized, the phase change due to XPM is described by Eq. (3.1). However, when the two input signal are cross-polarized, the nonlinear refractive index change due to XPM is described as [43]

$$\Delta n_{r,x} = \frac{2}{3} n_2^I \left|E_y\right|^2 \qquad (3.6)$$

so that, the phase change due to XPM is given by [9]

$$\Delta\phi_x = \left|k_0 \Delta n_{r,x} L\right| = \frac{2}{3}\gamma L_{eff} P_y \qquad (3.7)$$

The phase change of two cross-polarized signals is one third that of two co-polarized signals. To have a clear view, Figure 3.14 illustrates the impact of polarization on format conversion: we fix the probe signal angle at 0 degrees and plot the receiver sensitivity as a function of the angle of the pump signal. Both a CW probe and an RZ probe are plotted for comparison. When the pump signal is co-polarized with the probe signal, the receiver sensitivity improves by 3 dB compared to when there is a 60 degree difference between the state of polarization (SOP) of the pump and probe. Moreover, there is a 3 dB difference in receiver sensitivity when comparing CW and RZ probe signals.

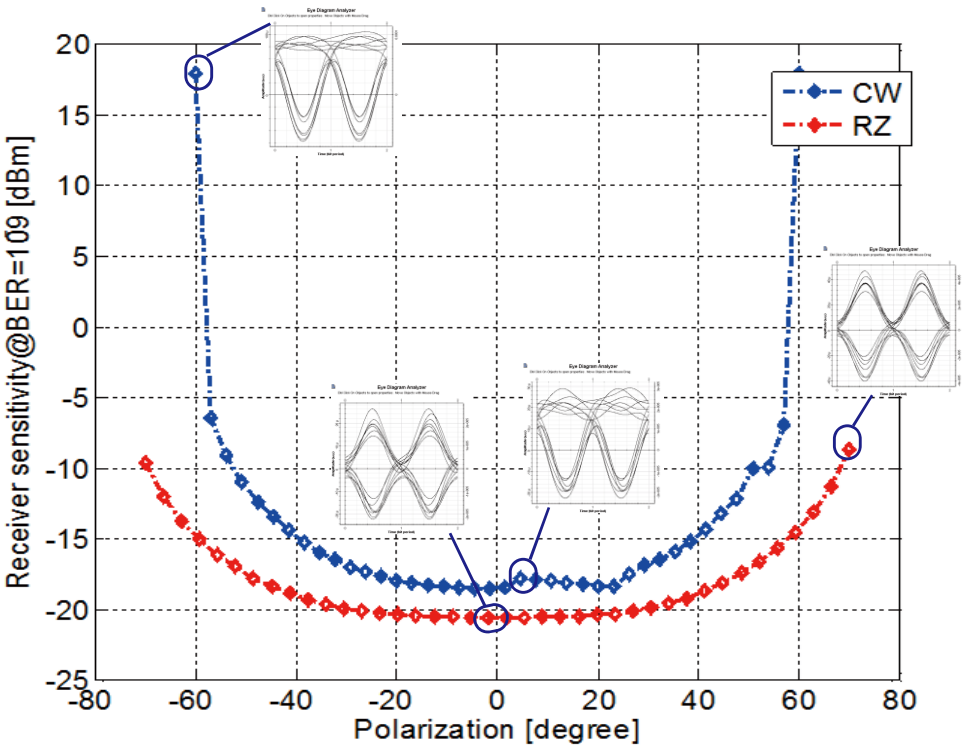

Figure 3.14 Receiver sensitivity plot versus polarization

3.3.7 PMD

Figure 3.15 shows the dependence of the received power on the differential group delay (DGD) of the input signal for both a CW probe and an RZ probe. The DGD was adjusted by adding a PMD emulator to the system. The performance of the conversion remains constant for up to 25 ps of DGD in both cases of a CW probe and an RZ probe. For these values of DGD, the impact on the optical pulse shape of the pump was similar to an increase in the duty cycle. As the DGD increases, the mismatch between the X and Y-polarizations of the input pulses increases, which cause the performance of the format conversion to drop. The RZ probe has a 6 dB advantage compare to a CW probe and the degradation in performance as a function of DGD is higher for the CW probe.

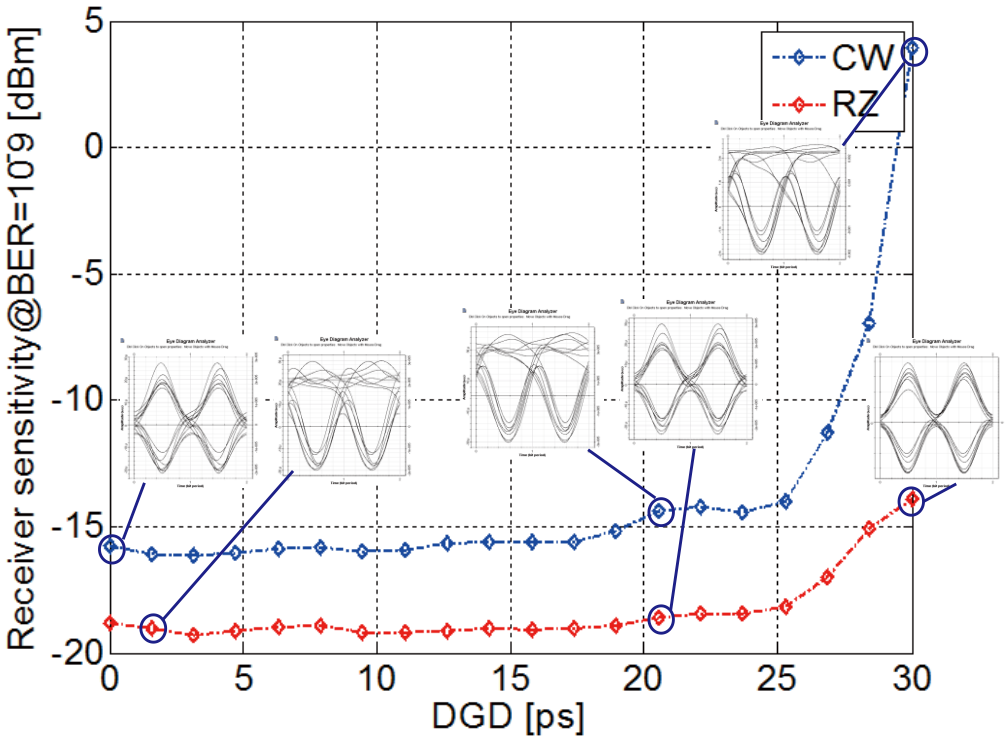

Figure 3.15 Receiver sensitivity plot versus DGD

3.3.8 OSNR

The OSNR is adjusted by coupling the input RZ-OOK pump with a white light source followed by a 0.4 nm Gaussian optical filter centered at the input wavelength. When the OSNR of the input signal is greater than 40 dB (0.1 nm noise bandwidth), the receiver sensitivity for error-free format conversion is -19 dBm and -17 dBm for an RZ probe and a CW probe, respectively. As the OSNR decreases below 35 dB, the receiver sensitivity starts to degrade rapidly. The results are summarized in Figure 3.16.

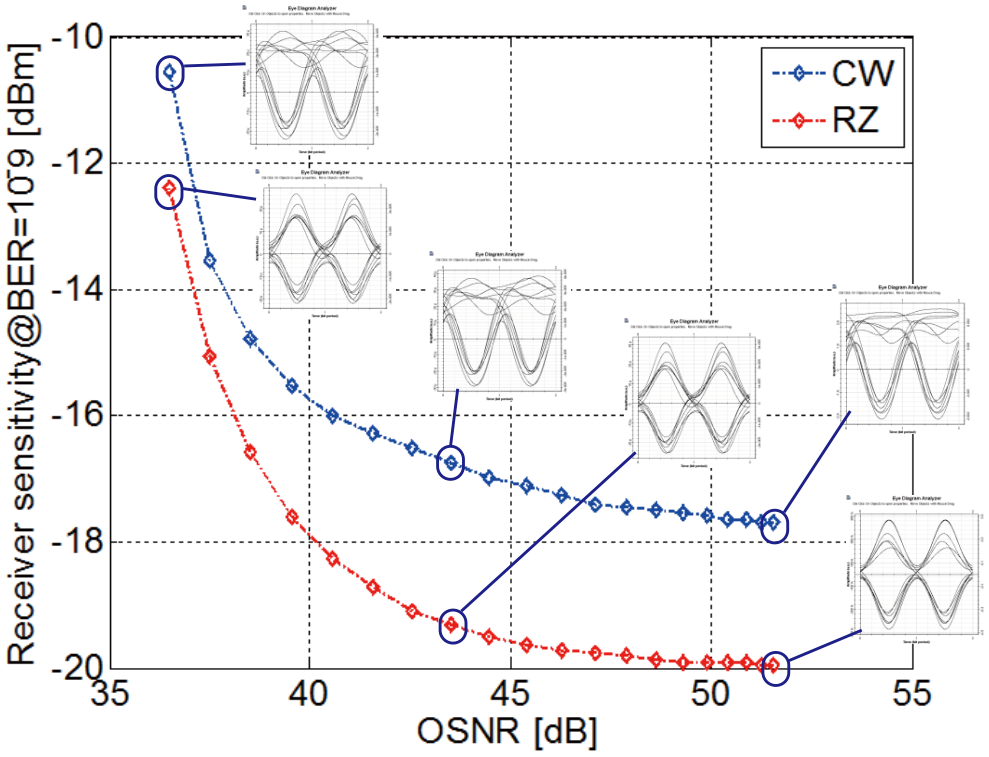

Figure 3.16 Receiver sensitivity plot versus OSNR

3.3.9 Residual Dispersion

Residual dispersion occurs in optical transmission systems when the links are not perfectly dispersion compensated. Figure 3.17 illustrates the dependence of the receiver sensitivity of the format conversion on the residual dispersion of the input

RZ-OOK signal. The residual dispersion was adjusted by adding a spool of fiber to the simulation. The receiver sensitivity is about -20 dBm and -17 dBm for a residual dispersion in the range of 0 ps/nm to 200 ps/nm for an RZ and CW probe, respectively. Outside this range, pulse broadening causes degradation in the format conversion, analogous to signals with a large duty cycle.

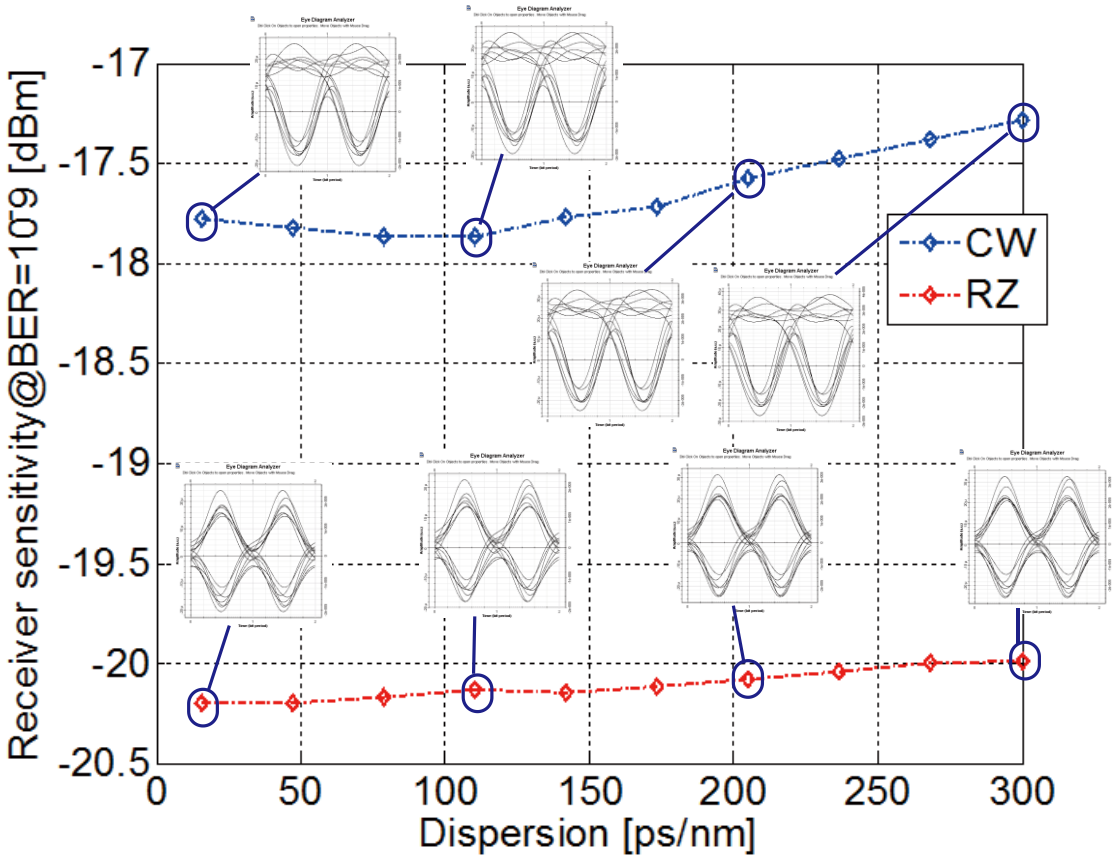

Figure 3.17 Receiver sensitivity plot versus residual dispersion

3.3.10 FSR

The FSR of the MZDI at the receiver is very important to the BER measurement of the demodulated signal. Figure 3.18 shows the dependence of the receiver sensitivity as a function of the delay of the MZDI (the FSR was adjusted by changing the delay parameter of the MZDI in the simulation system). In order to have stable performance,

the time delay in the MZDI should be kept between 80 ps and 120 ps, for both the RZ and CW probes. Outside of this range, the mismatch causes a serious degradation in the format conversion performance.

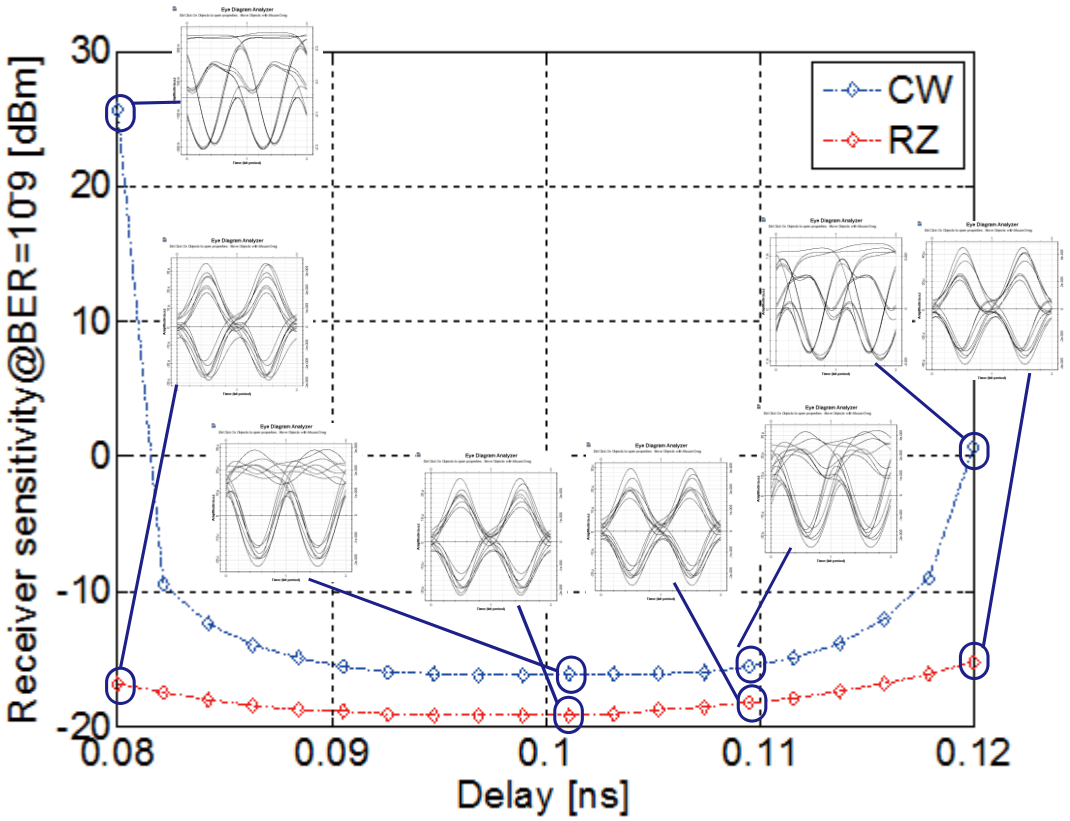

3.18 Receiver sensitivity plot versus delay in MZDI

3.4

Experiment results and analysis

As discussed in Chapter 3.2.2, we chose RZ-OOK for our experiments, which produce more reliable results for XPM-based format conversion. Figure 3.19 shows the experimental setup. The FSR of the delay line interferometer is 12.5 GHz. Based on simulation results, in order to have the best performance for format conversion, we

operate our experiment at 12.5 Gb/s to match the FSR. An RZ pulse is generated by modulating a tunable laser source (TLS) in a MZM (MZM1) at a wavelength of 1548 nm. The duty cycle of the pulse is kept at 40%. The RZ pulse is then passed through another MZM (MZM2) driven by a 12.5 Gb/s pseudo random bit sequence (PRBS) of length $2^{31} - 1$ to generate the RZ-OOK pump pulse, shown in Figure 3.20 (a). The OSNR of the pump is measured to be 42 dB. An RZ probe pulse is generated by modulating the CW light from a distributed feedback laser (DFB) at 1537.4 nm using a MZM (MZM3) driven by a 12.5 GHz clock from a synthesizer. The duty cycle of the probe signal is kept at 33%, as shown in Figure 3.20 (b). A 0.4 nm tunable bandpass filter is used to filter out the ASE noise generated from the EDFA3, and the OSNR is measured to be 41.7 dB. A tunable delay line is added to the setup to align the probe pulse and the RZ-OOK signal, see Figure 3.20 (c). The pump and probe signal are coupled together by a WDM coupler. We use a polarizer to make the pump and the probe co-polarized in order to optimize the performance of the format conversion. After the polarizer, the pump and probe signals are launched into the HNLF to undergo XPM. The parameters of the HNLF are provided in Table 3.1. A 0.8 nm tunable bandpass filter is used to select the probe signal before amplification by EDFA4. A 0.85 nm tunable bandpass filter is used to filter out the ASE. The converted RZ-DPSK signal is then passed into the MZDI to demodulate the DPSK signal. A balanced PD is used to transfer the optical signal into electrical signal and we use an error detector to measure the BER. The balanced PD has a 3 dB bandwidth of 45 GHz, a common mode rejection ratio (CMRR) of 15 dB, a DC responsivity of 0.5 A/W, and a dark current of 5 nA.

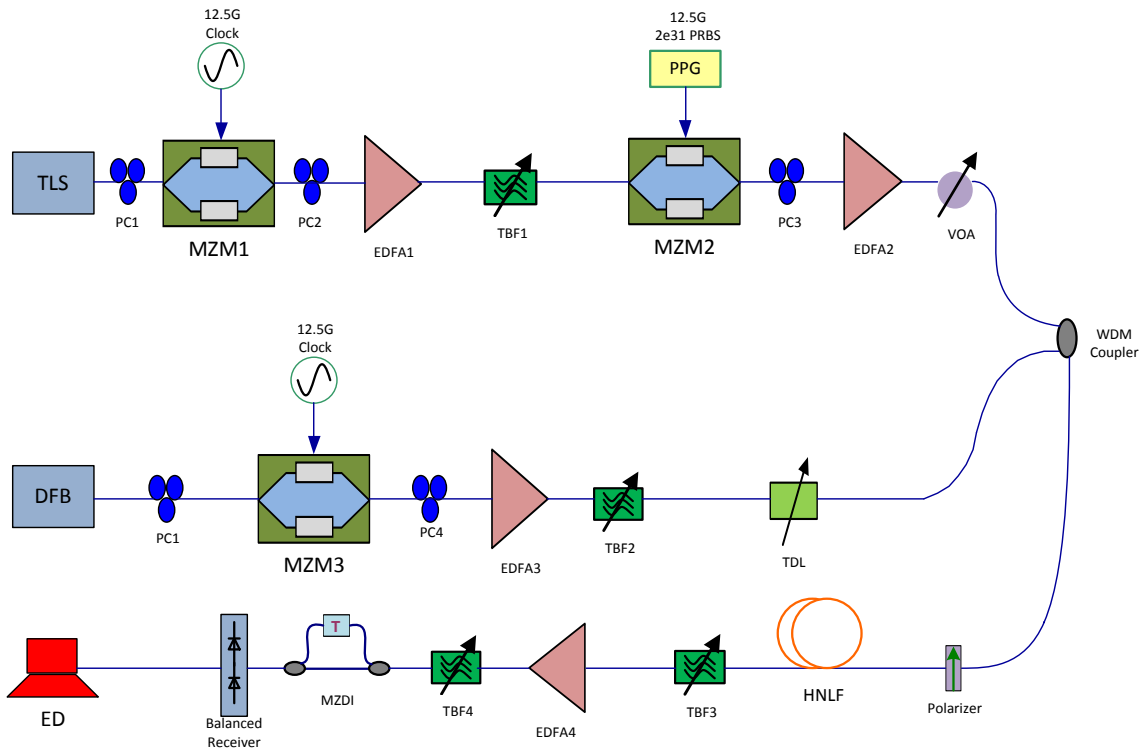

Figure 3.19 Experiment setup of RZ-OOK to RZ-DPSK format conversion

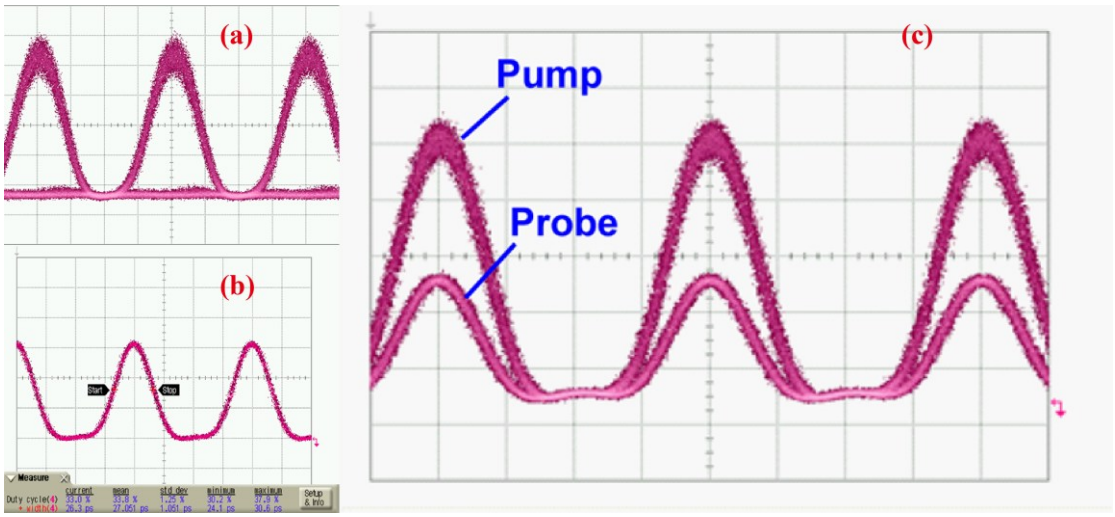

Figure 3.20(a) RZ-OOK pump at 4dBm with 40% duty cycle. (b) RZ probe with 33% duty cycle. (c) Pump and probe aligned together. [20 ps/div]

3.4.1 Pump Power

First, we consider the impact of varying the pump power. Figure 3.21 shows the measured eye diagrams of the converted signal at various average powers of the pump signal.

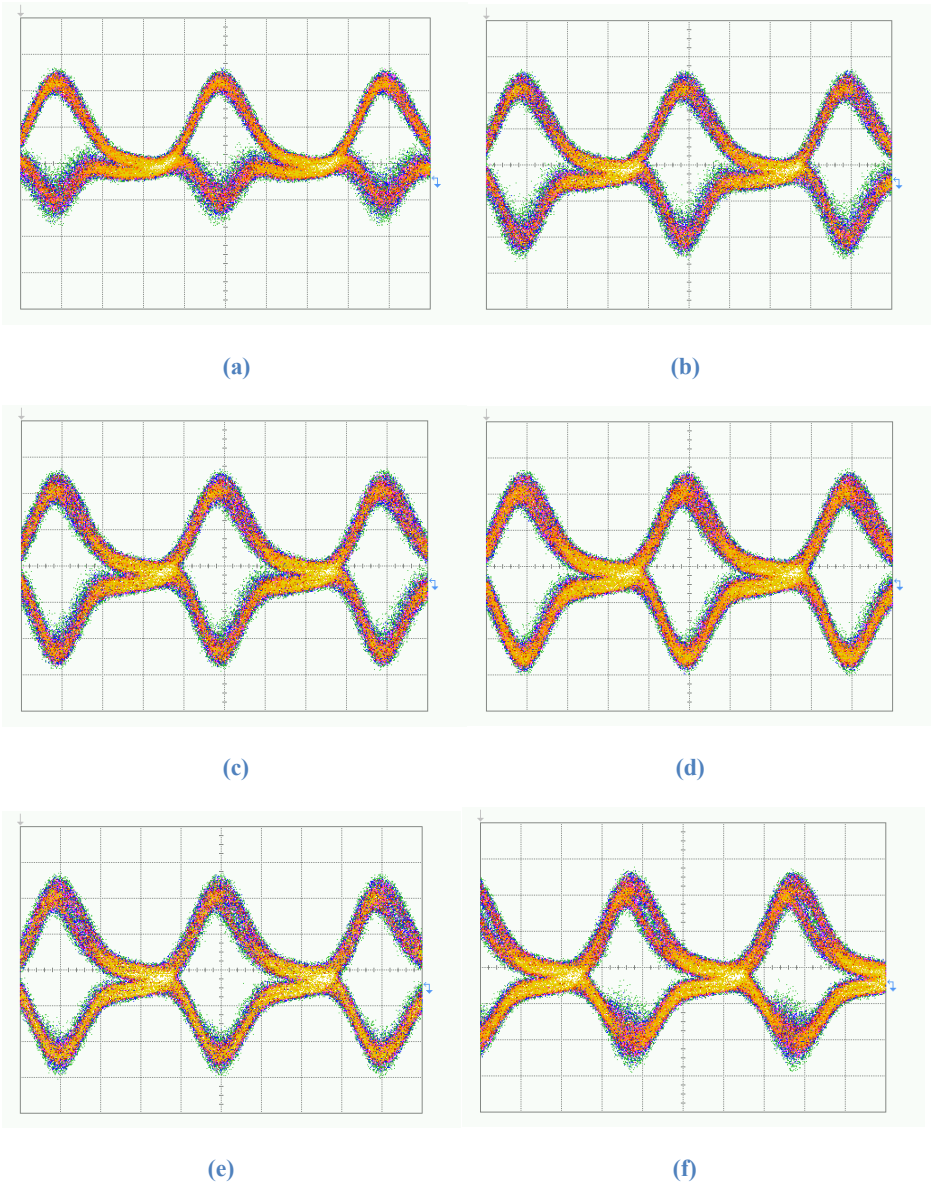

Figure 3.21 Eye diagram when the average pump power is (a) 15 dBm, (b) 16 dBm, (c) 16.5 dBm, (d) 17 dBm, (e) 17.5 dBm and (f) 18 dBm. [20 ps/div]

For each case, we measure the corresponding BER, see Figure 3.22. Note that the back-to-back measurements are made right after MZM2, the duty cycle of the RZ-OOK pump is 38%. When the average pump power is 17.5 dBm, there is roughly 3

dB power penalty due to the conversion process. We can see that the optimum average pump power is 17.5 dBm (corresponding to a peak power of 20.98 dBm). The average pump power level to have error-free operation is from 15 dBm to 18 dBm. Figure 3.23 (a) shows a receiver sensitivity plot for different pump powers at 38% duty cycle. The green line is a shape-preserving curve. Figure 3.23 (b) shows the simulation result of the receiver sensitivity plot with the same parameters, except the bit sequence length (in the experiment, the sequence length is $2^{31} - 1$, whereas in the simulation, it is $2^5 - 1$). Although the simulated and measured results differ in absolute values of received power, in general they exhibit similar trends. The difference in received power between the experiment and simulation results is due in part to the difference in the bit sequence length used. Both curves initially decrease as the necessary power to have π phase shift is approached, and then they increase as the power increases.

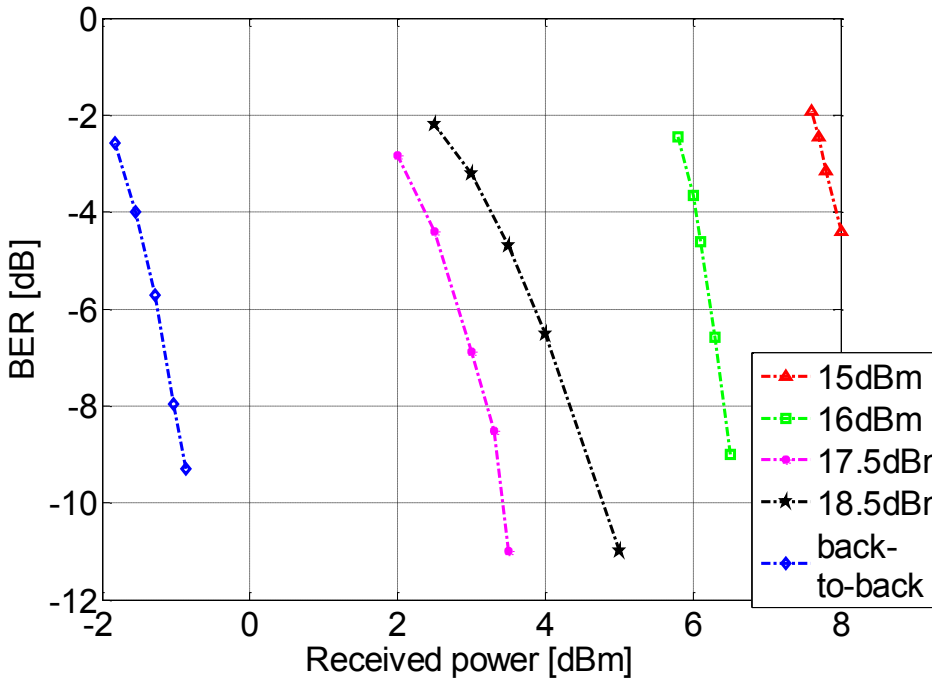

Figure 3.22 BER for various powers of RZ-OOK pump with 38% duty cycle.

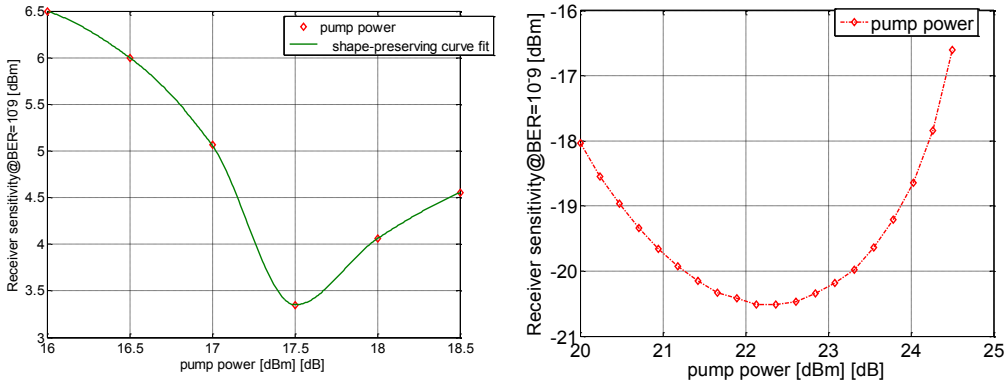

(a) (b)

Figure 3.23 (a) Received power for different pump power to have 10^{-9} BER with 38% duty cycle (b) Simulation results of received power for different pump power to have 10^{-9} BER

3.4.2 Duty Cycle

We adjust the bias voltage of MZM1 to obtain different duty cycles for the RZ-OOK pump. We change the average power of the pump before the HNLF to keep the peak power at 21.5 dBm while varying the duty cycle. Figure 3.24 shows the eye diagrams of the converted signal. Figure 3.25 shows the BER of the converted signals for the different duty cycles. We cannot obtain error-free operation at a duty cycle of 46%. There is about 4 dB power penalty due to the conversion process. At a duty cycle of 38%, we can operate the conversion process under an error-free condition at the minimum received power. Performance of the format conversion drops slightly when we increase the duty cycle beyond 38% or when we decrease the duty cycle below 38%. The conversion process fails to achieve error-free performance when the duty cycle is larger than 46%. The larger duty cycle requires a larger average power to maintain the same peak power which result in larger ASE noise and parametric amplification. Figure 3.26 (a) shows a receiver sensitivity plot for different pump duty cycles with 21.5 dBm peak power. The green line is a shape-preserving curve fit.

Figure 3.26 (b) shows the simulation result of the receiver sensitivity plot with the same parameters. The receiver sensitivity for both the experiment result and the simulation result decreases to a minimum point as the duty cycle increases, and then they increase afterwards. Again, the difference in received power between the experiment and simulation results is due to the difference in the bit sequence length. Since we were keeping the peak powers of each case at the same level, ideally the XPM induced phase change should be the same for each case. However, a larger duty cycle requires higher pump power to maintain the same peak power, thereby introducing additional noise and preventing error free operation (e.g., when the duty cycle is 46%). From both the simulation and experiment results, we can conclude that the duty cycle has an effect on the performance of the format conversion.

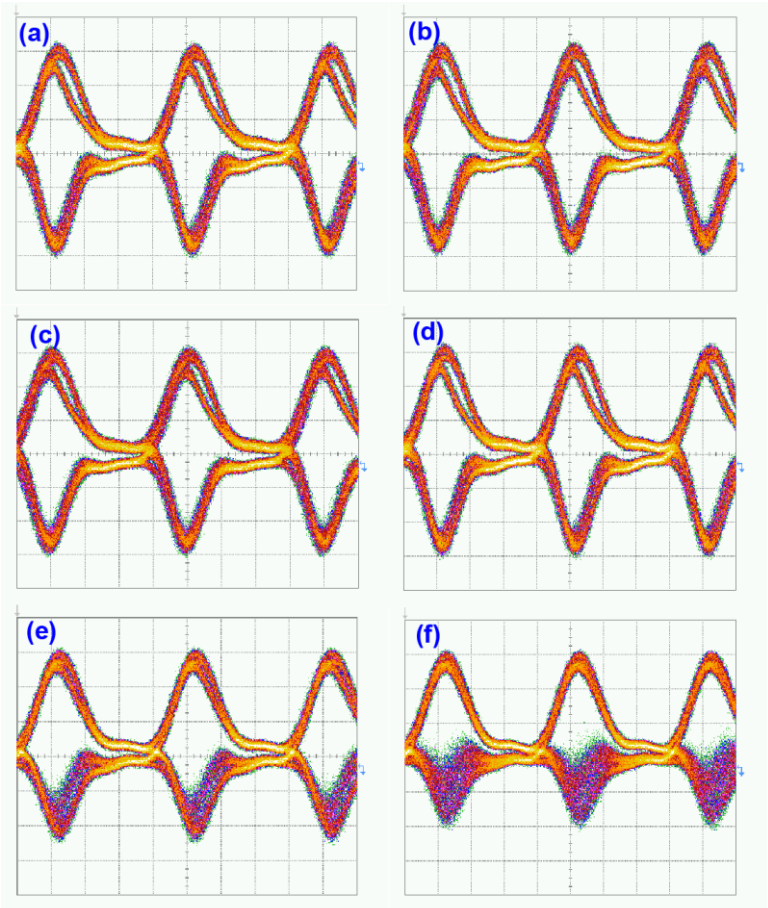

Figure 3.24 Eye diagrams with different duty cycles: (a) 36%, (b) 38%, (c) 40%, (d) 42%, (e) 44% and (f) 46%. [20 ps/div]

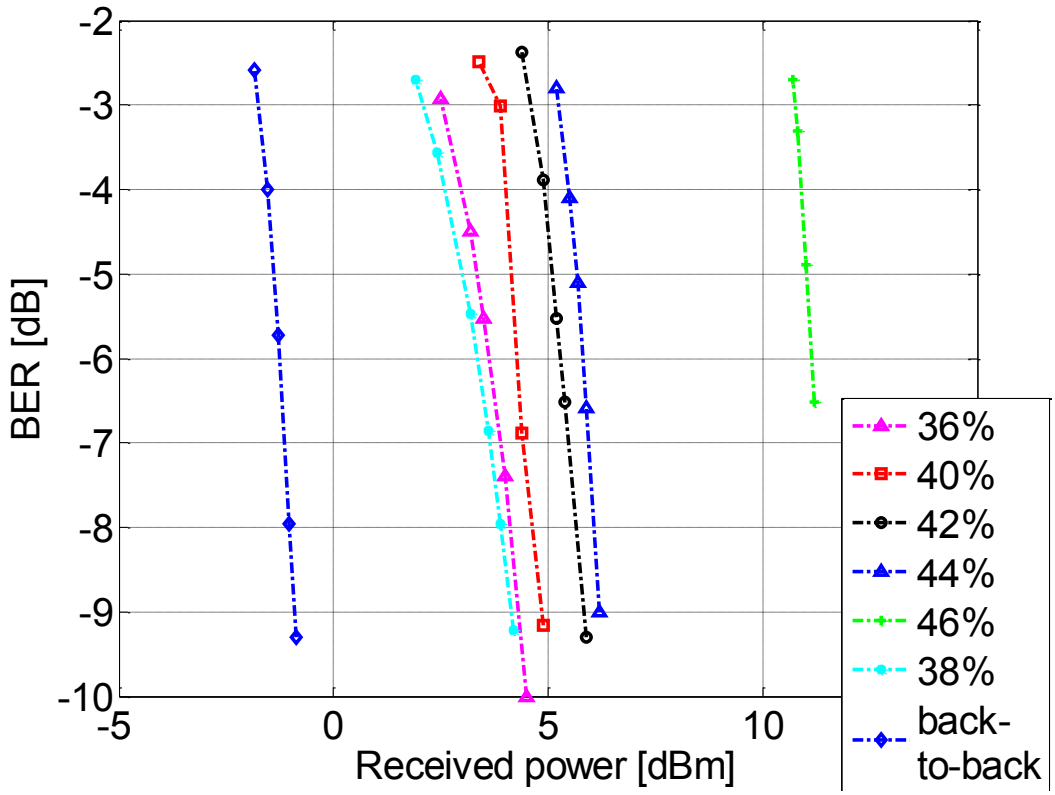

Figure 3.25 BER for various duty cycles of RZ-OOK pump with 21.5 dBm peak power

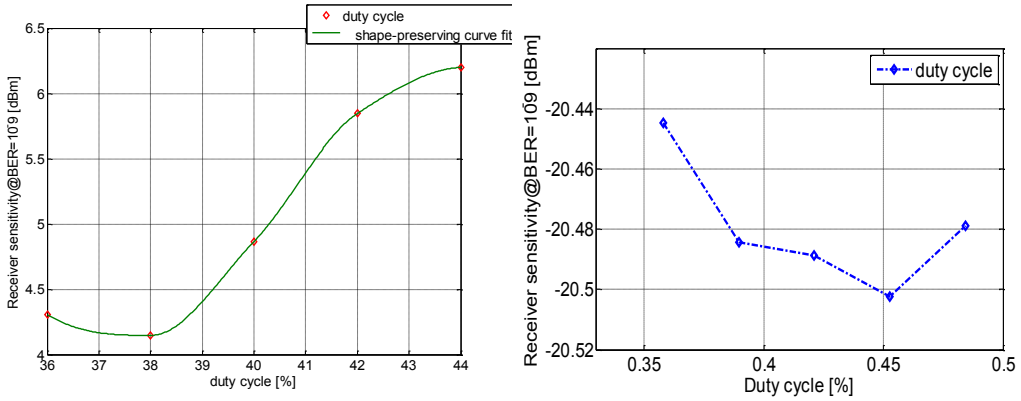

(a) (b)

Figure 3.26 (a) Received power for different pump duty cycles to have 10^{-9} BER with 21.5 dBm peak power. (b) Simulation results of received power for different duty cycles to have 10^{-9} BER

3.4.3 Residual Dispersion

We add a dispersion compensator before EDFA2 to simulate residual dispersion in the RZ-OOK pump signal. Figure 3.27 shows the eye diagrams of the RZ-OOK pump

with different value of dispersion. The inset above every eye diagram shows the pump with the corresponding dispersion measured at 4 dBm average pump power. The increase of residual dispersion causes a temporal pulse-broadening; at a dispersion of 300 ps/nm, the quality of the RZ-OOK pump signal is quite low.

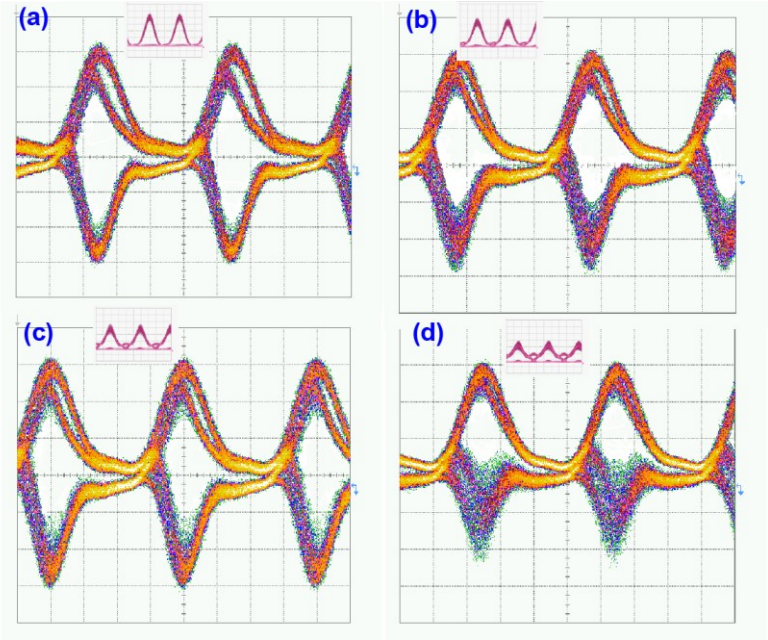

Figure 3.27 Eye diagram for various dispersions on RZ-OOK pump: (a) 100 ps/nm, (b) 200 ps/nm, (c) 250 ps/nm and (d) 300 ps/nm. [20 ps/div]

Figure 3.28 compares the performance of the conversion for different amounts of residual dispersion. The back-to-back measurements are made at 38% duty cycle with zero dispersion. There is a 4 dB power penalty due to the conversion process. At a dispersion of 0 ps/nm, the performance of the conversion process is the best. The performance of the format conversion drops when we increase the dispersion. After a dispersion of 250 ps/nm, we can no longer sustain error-free operation. Figure 3.29 (a) shows a receiver sensitivity plot for different amounts of residual dispersion. Figure 3.29 (b) shows the corresponding simulation results. Comparing the experimental results to the simulation results shows that the performance of the format conversion degrades as the dispersion increases. The dispersion distorts the pump signal and decreases the efficiency of XPM. From the experimental results, we can conclude that

the residual dispersion has a large impact on the performance of the format conversion.

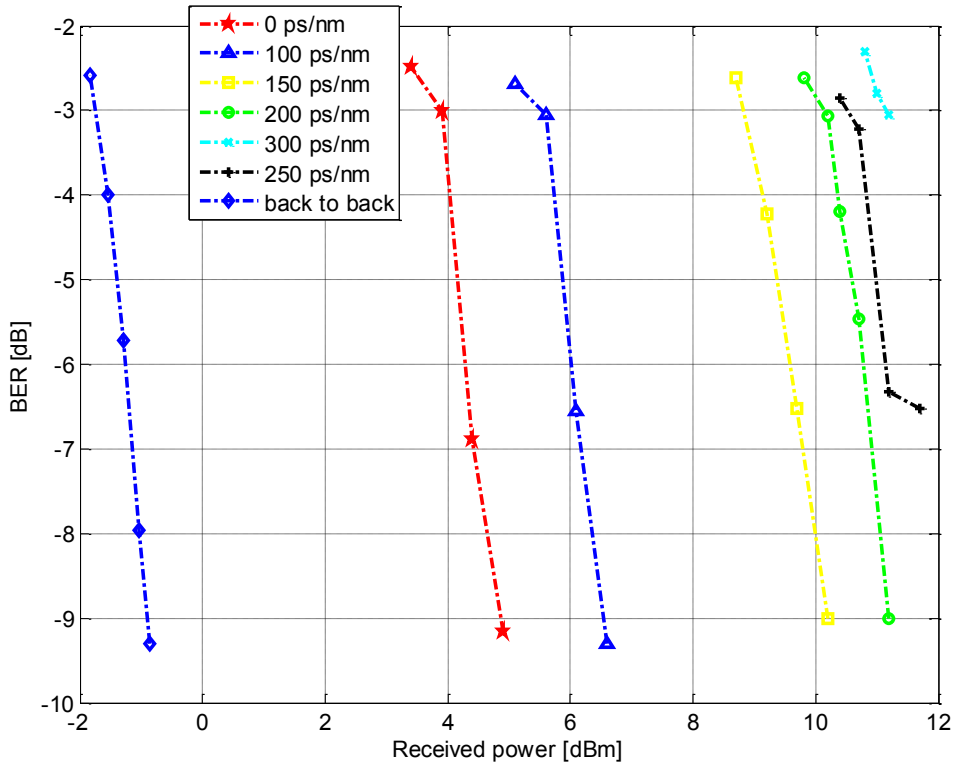

Figure 3.28 BER for various dispersions on RZ-OOK pump

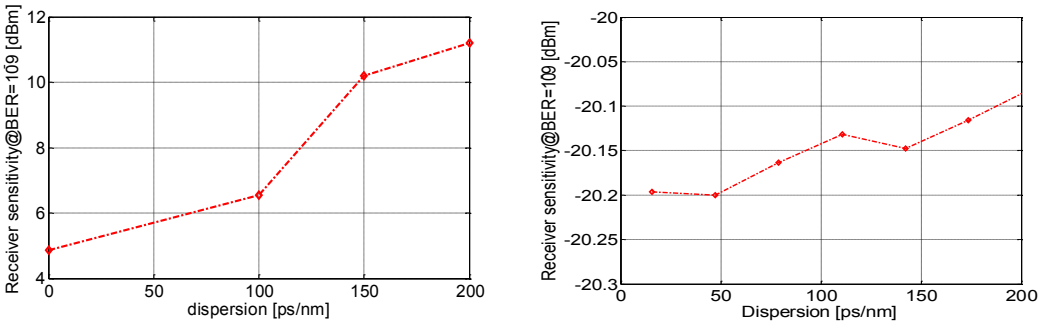

(a) (b)

Figure 3.29 (a) Simulation results of received power for different dispersions to have 10^{-9} BER. (b) Simulation results of received power for different dispersions to have 10^{-9} BER

3.4.4 OSNR

We adjust the OSNR of the RZ-OOK pump signal to see the degradation of the format conversion due to a change of OSNR. Figure 3.30 shows that we couple a new

branch to the RZ-OOK pump signal. TBF4 with a bandwidth of 0.4 nm and a center wavelength of 1548 nm is used to filter the ASE noise generated from EDFA5, and EDFA6 is used to amplify the ASE noise. VOA2 was placed before the coupler to control the power of the noise. We adjust the attenuation of the VOA2 to add noise to the RZ-OOK pump while keeping the other parameters the same as before. Figure 3.31 shows the converted eye diagrams for various pump OSNRs. The insets show the eye diagrams of the corresponding pump signal. All OSNRs are measured with a 0.1 nm noise bandwidth. The decrease of OSNR causes an increase in the ASE noise of the pump signal, and additional fluctuations for the converted signal. We can see that the conversion qualities drop as the OSNR decreases.

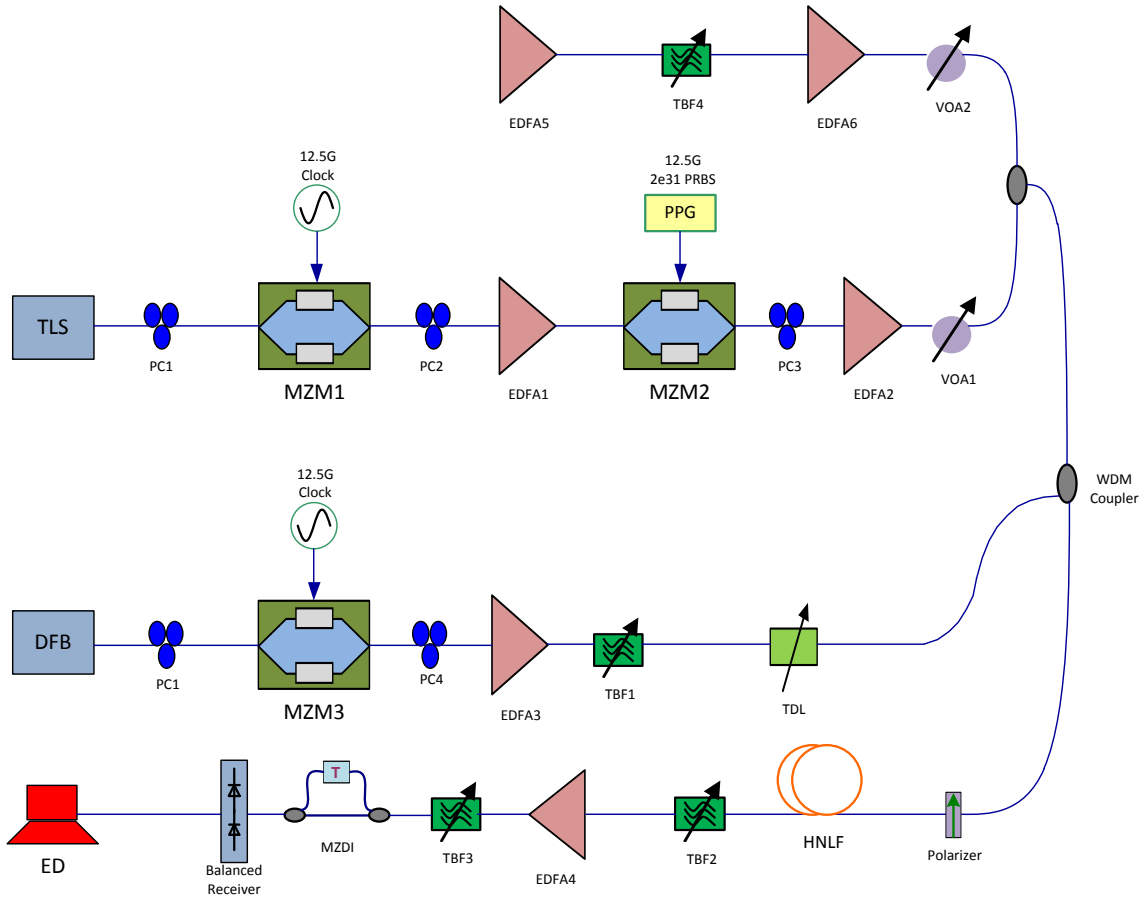

Figure 3.30 Experiment setup for RZ-OOK to RZ-DPSK format conversion to adjust OSNR

Figure 3.32 shows the BER as a function of OSNR. The back-to-back signal has an OSNR of 44 dB. At an OSNR of 44 dB, the performance of the format conversion process is the best. The performance of the format conversion drops when we decrease the OSNR and in particular, below an OSNR of 36 dB, we cannot have error-free operation (while the phase shift caused by XPM is sufficient, noise limits the BER). Figure 3.33 (a) shows a receiver sensitivity with various OSNRs and Figure 3.33 (b) shows the corresponding simulation results. From both the experiment results and simulation results, we can conclude that the OSNR of the RZ-OOK pump has to be larger than 36 dB in order to achieve proper modulation format conversion.

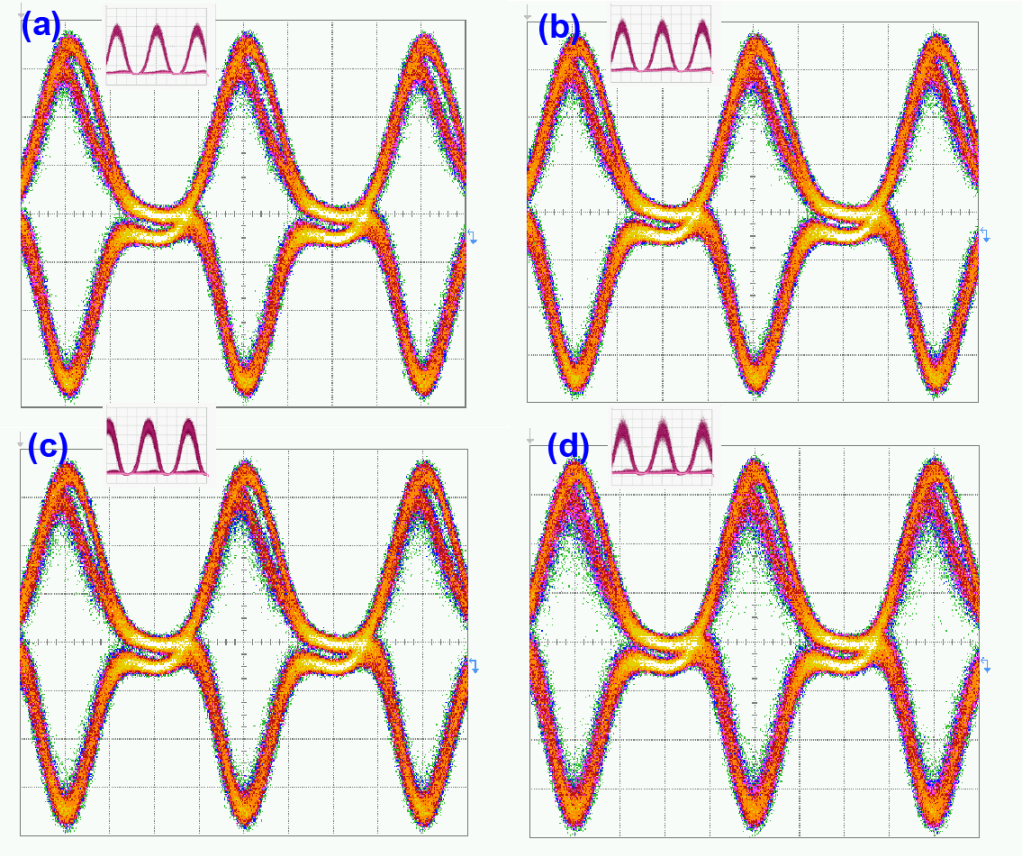

Figure 3.31 Eye diagram for various OSNR on RZ-OOK pump: (a)40 dB, (b)36 dB, (c)32 dB and (d)28dB. [20 ps/div]

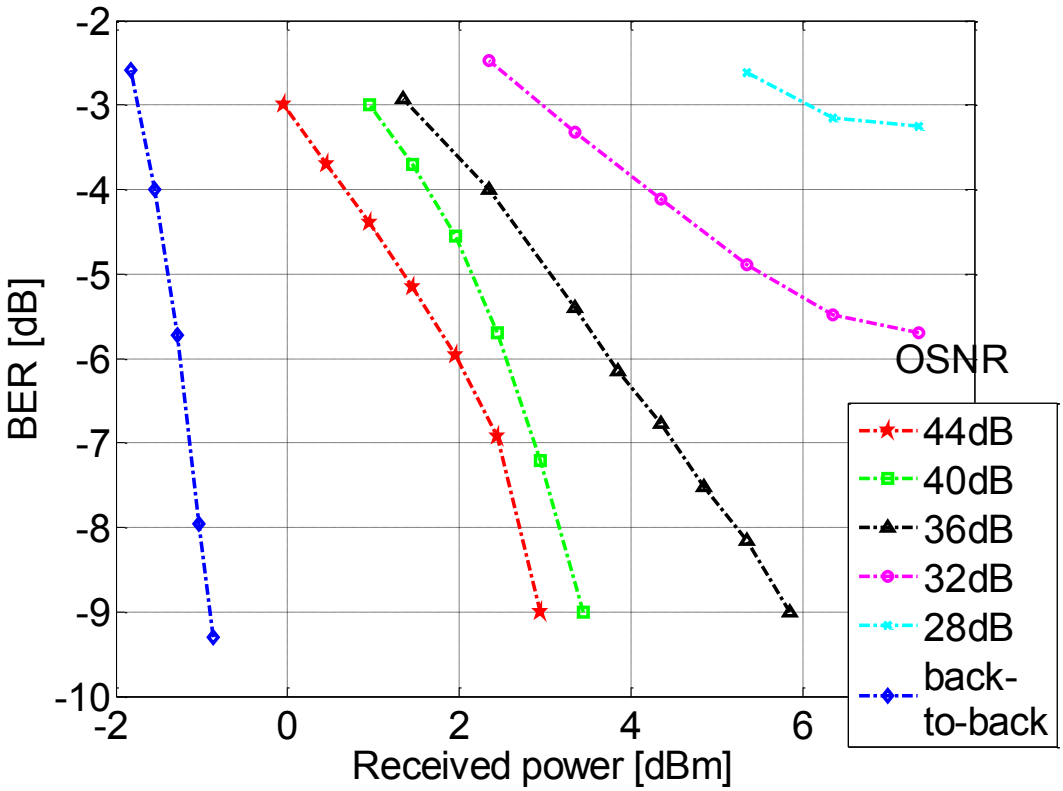

Figure 3.32 BER for RZ-OOK pump with various OSNRs

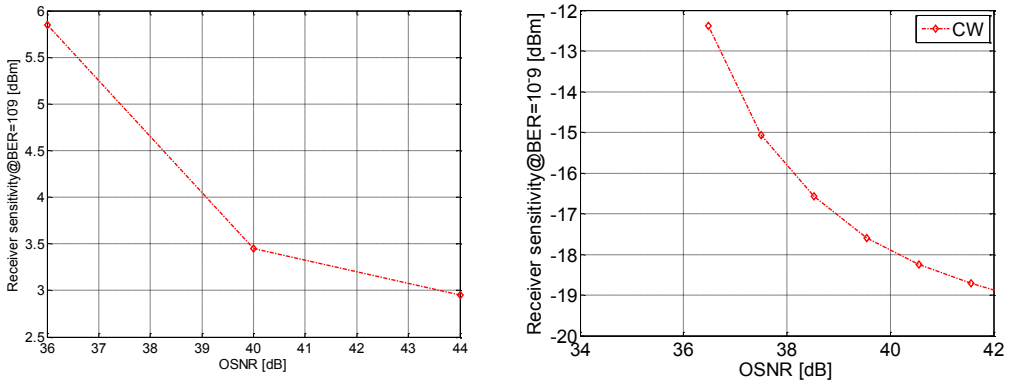

(a) (b)

Figure 3.33 (a) Received power for pump with various OSNRs to have 10^{-9} BER. (b) Simulation results of received power for pump with various OSNRs to have 10^{-9} BER.

3.4.5 DGD

We add a PMD emulator before EDFA2 to adjust the DGD of the RZ-OOK pump. In our experiments, we use a polarizer, since XPM is polarization-dependent; thus,

changing the DGD of the pump signal is equivalent to adding a time delay to the signal. Figure 3.34 shows the RZ-OOK pump with a DGD of 25 ps, 50 ps, 75 ps, and 100 ps. The increase in DGD causes a mismatch between the pump signal and the probe signal. At DGDs of 25 ps, 50 ps, and 100 ps, the mismatch is large; thus, the format conversion fails. However, at a DGD of 75 ps, which is close to the period of the signal (80 ps), the format conversion is successful. Figure 3.35 shows the BER plot for different DGDs. The insets are the corresponding eye diagrams. The BERs of 25 ps and 50 ps were not measureable, the eye is totally closed, the pump and the probe were totally misaligned.

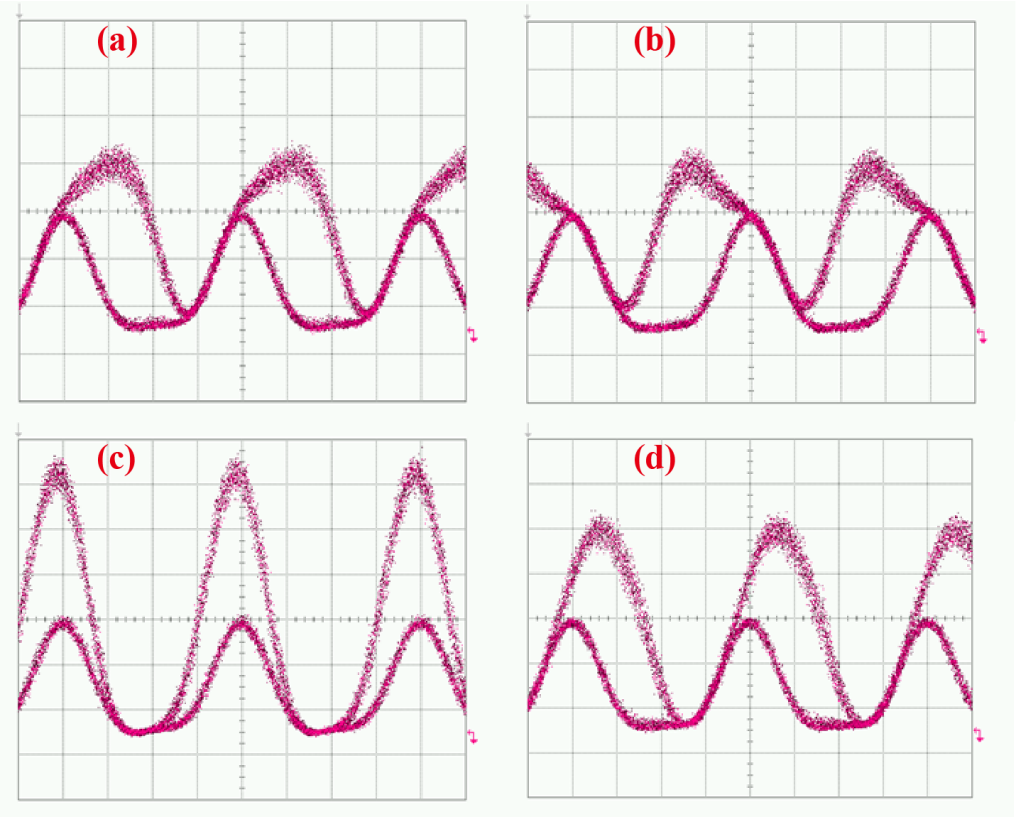

Figure 3.34 RZ-OOK pump with (a) 25 ps DGD, (b) 50 ps DGD, (c) 75 ps DGD and (d) 100 ps DGD. [20 ps/div]

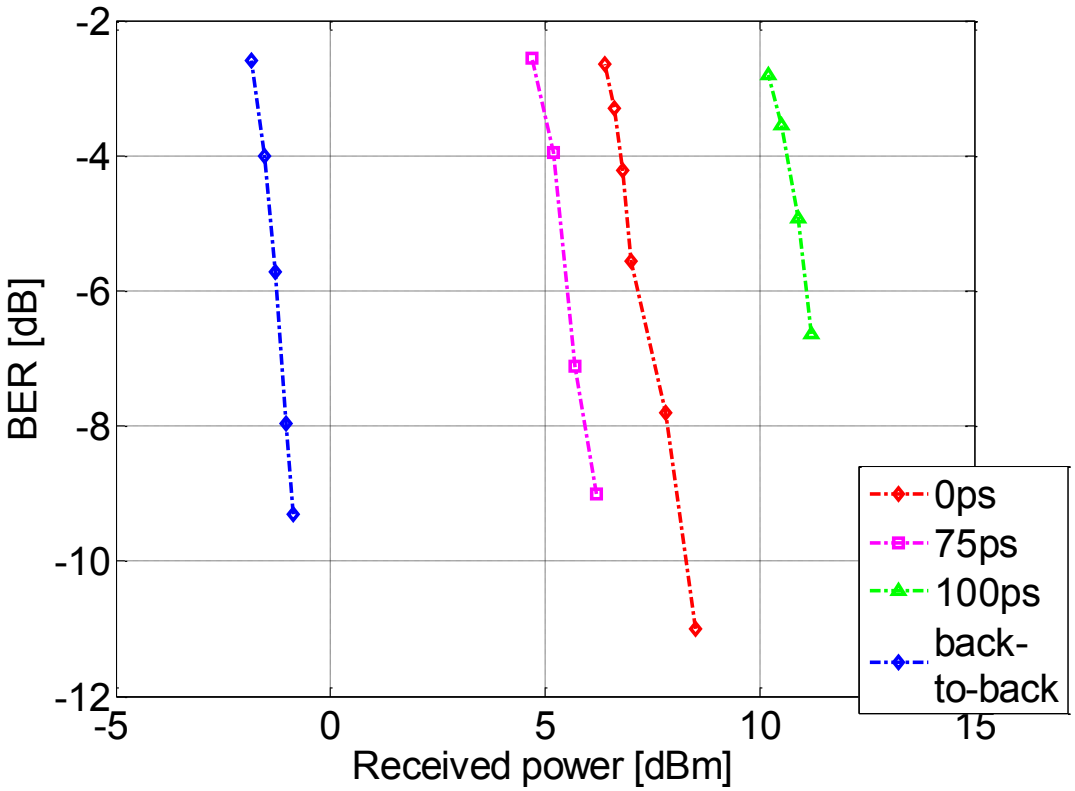

Figure 3.35 BER for various DGDs on RZ-OOK pump.

3.5

OOK to DPSK Modulation Format Conversion With Wavelength Multicasting

Taking the optimized parameters from Section 3.4, we then designed an RZ-OOK to RZ-DPSK format conversion scheme capable of wavelength multicasting. Four RZ probe signals, with a wavelength spacing of 0.8 nm are coupled with an RZ-OOK pump and transmitted through a length of HNLF. XPM occurs simultaneously on all four probes which impose a phase change when the pump signal is on. The phase change is π by adjusting the input power of the pump. After the HNLF; the four channels of RZ-DPSK signals can be obtained individually by optical filtering. Figure

3.36 shows the experiment setup of OOK to DPSK format conversion with wavelength multicasting. The experiment is carried out at 12.5 Gb/s to match the FSR of the MZDI (12.5 GHz). An RZ pulse is generated by modulating a TLS using MZM1 at a wavelength of 1548 nm. The duty cycle of the pulse is 38%. The RZ pulse is then modulated by MZM2 to generate the RZ-OOK pump signal (PRBS of length $2^{31} - 1$), as shown in Figure 3.37. The OSNR of the pump is measured at 44 dB. Four CW signals at wavelengths of 1534.94 nm, 1535.73 nm, 1536.50 nm and 1537.4 nm are coupled together by an AWG and then modulated by MZM3 driven by a 12.5 GHz clock from a synthesizer. The duty cycle of the probe signals are kept at 37%. The average powers of each wavelength are: 2.51 dBm at 1534.94 nm, 2.73 dBm at 1535.73 nm, 2.32 dBm at 1536.50 nm and 3 dBm at 1537.4 nm. A tunable delay line is added to the setup to align the four probe pulses and the RZ-OOK signal. The four probes and pump signal are coupled together by a WDM coupler. We use a polarizer to make the probe and the pump co-polarized in order to optimize the performance of the format conversion, and polarization of each channel is carefully adjusted to maximize the average power. After the polarizer, the pump and four probe signals are launched into the HNLF to undergo XPM. To test the performance of the conversion channel-by-channel, a 0.8 nm tunable bandpass filter is used to select the probe signal and is amplified by EDFA4. Another 0.85nm tunable bandpass filter is placed after in order to filter out the ASE noise from EDFA4. The converted RZ-DPSK signal is then passed into the MZDI to demodulate the DPSK signal. A balanced PD is used to transfer the optical signal into an electrical signal, and we use an error detector to measure the BER.

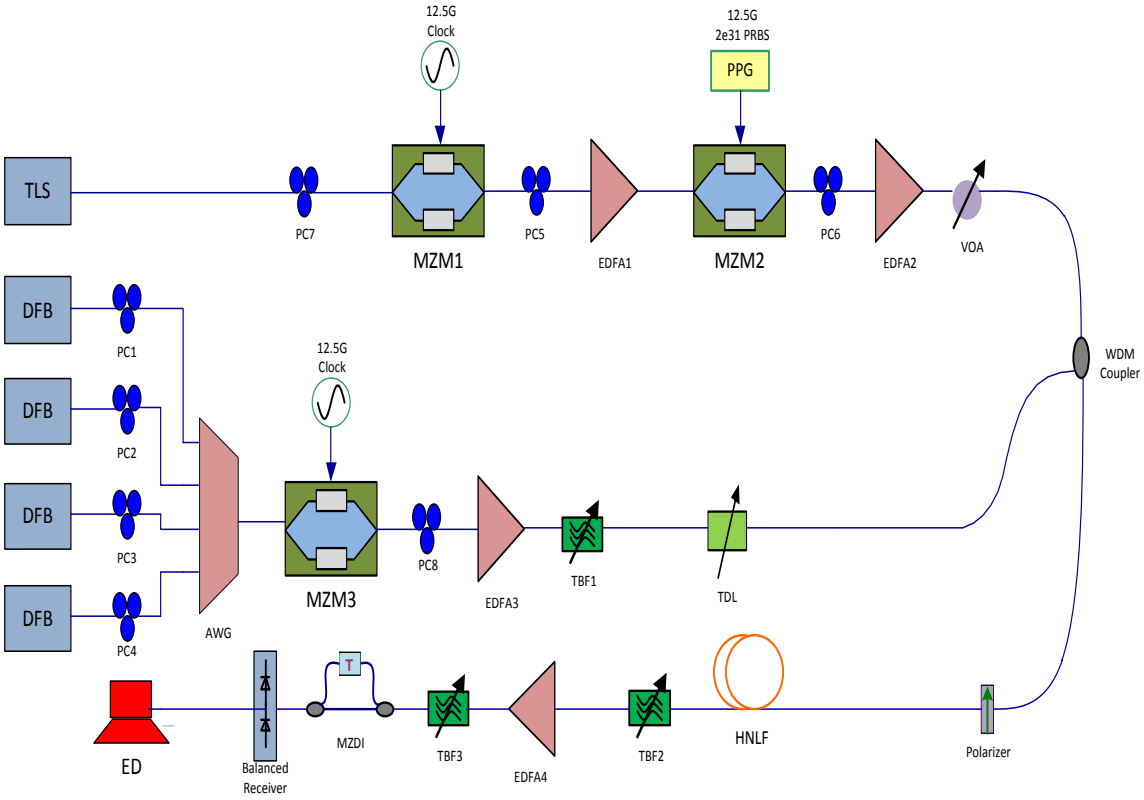

Figure 3.36 Experiment setup of the multicasting OOK to DPSK format conversion

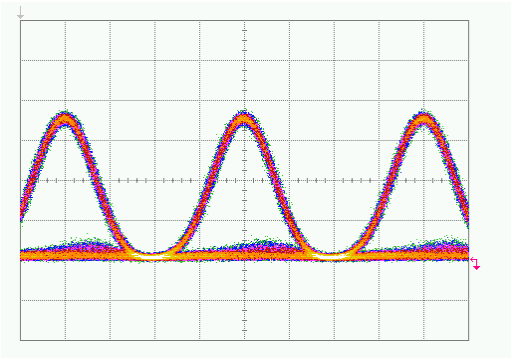

Figure 3.37 RZ-OOK signal at 4dBm. [20 ps/div]

Figures 3.38 (a) and (b) show the spectrum measured before and after the HLNF using the complex OSA. All four probes are broadened due to the XPM by the high power pump, and the pump spectrum is also broadened due to SPM. The powers of the four probes are kept relatively low so the FWM between each channel can be ignored, but the parametric amplification from the high power pump may distort the pulse shape when the pump power is really high. Figure 3.39 shows the eye diagrams of received electrical signals of each channel and Figure 3.40 shows the

corresponding BER plots. The eye diagrams of all channels are open, and error-free operation can be obtained. The back-to-back BER curve is measured after the MZM2, where the duty cycle of the pump is 37% with an OSNR of 44 dB. There is roughly 2 dB power penalty for the best case and 4 dB for the worst case. The difference in performance of format conversion for the four channels is due to the difference in peak power, duty cycle, and polarization of each probe. Although we are modulating the four probe signals using a single modulator, the adjustment of polarization of each probe is done individually, so the peak power, duty cycle, and polarization for each probe is not exactly the same.

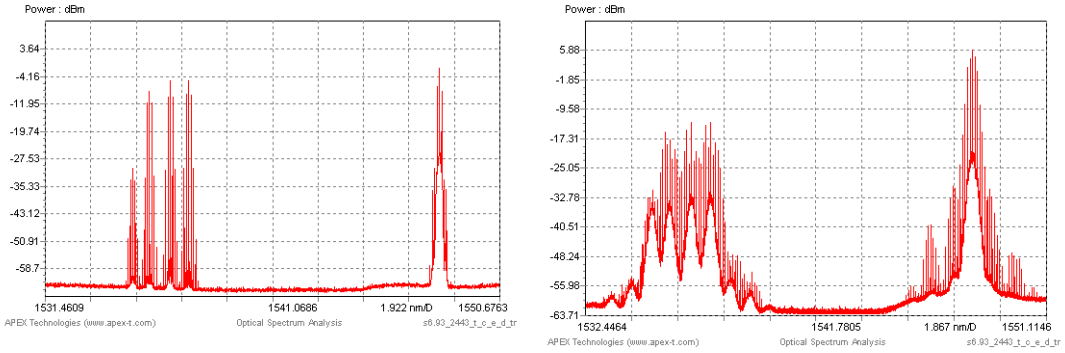

(a) **(b)**

Figure 3.38 Spectra (a) before and (b) after the HNLF

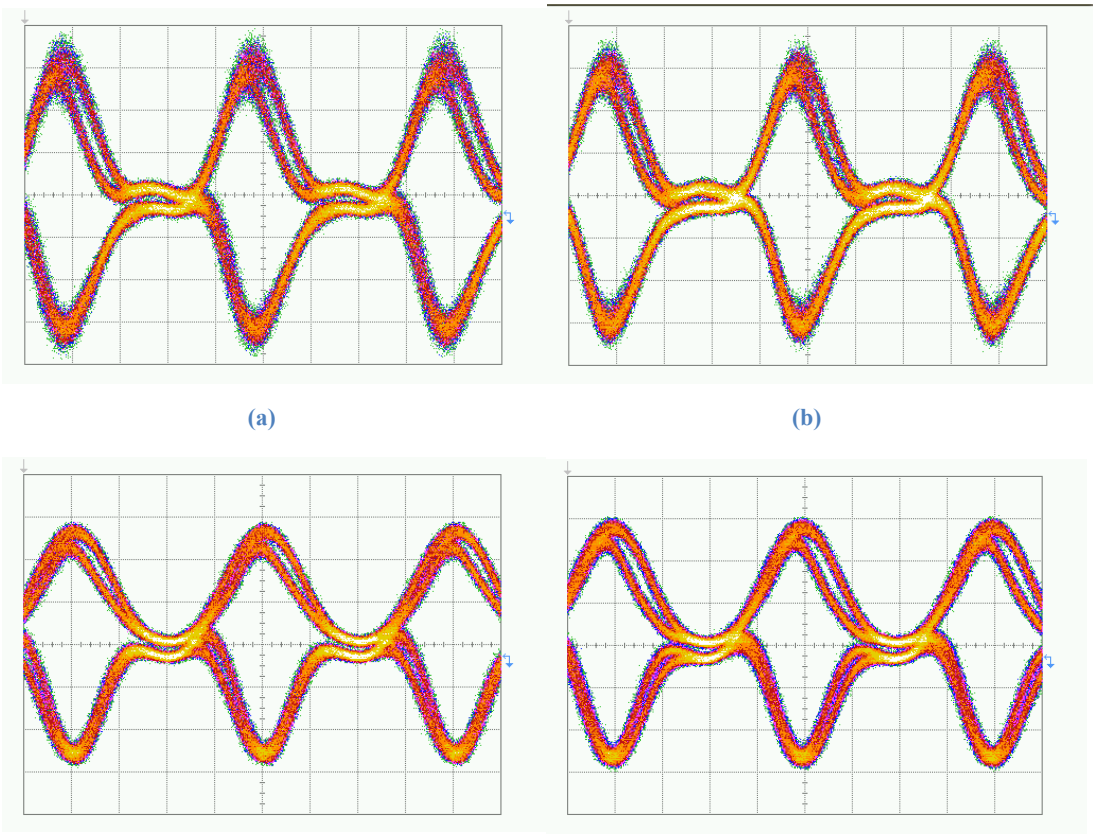

(a) (b)

(c) (d)

Figure 3.39 Eye diagram of the converted signal at (a) 1534.94nm, (b) 1535.73nm, (c) 1536.5nm and (d) 1537.4nm. [20 ps/div]

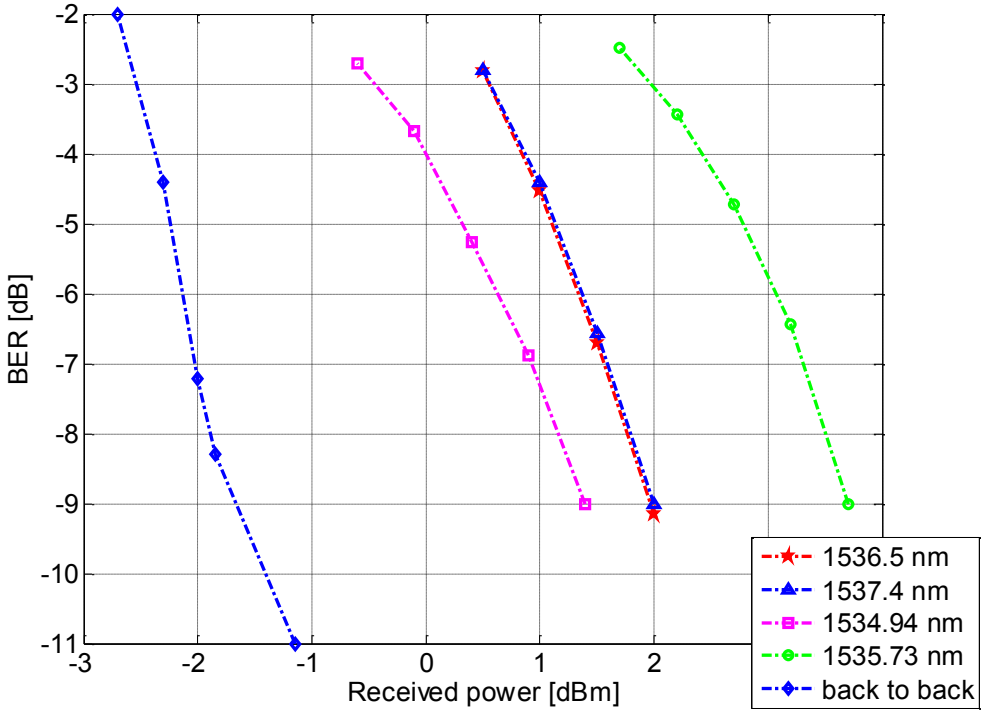

Figure 3.40 BER plots of different channels

3.6

Summary

In this chapter, we performed a detailed investigation of RZ-OOK to RZ-DPSK modulation format conversion. In Section 3.2, we explained the principle of operation and why we chose to use an RZ-OOK pump instead of NRZ-OOK. In Section 3.3, we simulated the impact of various signal impairments on the conversion process. In Section 3.4, we showed our experimental results. Finally, we demonstrated the conversion process with wavelength multicasting in Section 3.5.

Chapter 4

OOK to DPSK Modulation Format Conversion at 40 Gb/s

4.1

Introduction

In this chapter, we investigate the suitability of the OOK to DPSK format conversion at higher bit rates. In particular, we consider a bit rate of 40 Gb/s while keeping all other parameters the same (unless otherwise noted).

4.2

Pump and probe wavelength

4.2.1 RZ Probe case

We first consider the case when the probe is an RZ pulse. The duty cycle of the RZ pulse is 33% and the duty cycle of the RZ-OOK pump is 50% (in this case, the conversion fails when the duty cycle of the pump is 40%). We fix the pump peak power at 22.5 dBm (optimized value from OptiSystem™) and the probe peak power at 0 dBm. The probe wavelength is at 1548 nm, and we vary the pump wavelength to plot the receiver sensitivity. From Figure 4.1, we can observe that the minimum receiver sensitivity is acquired when the pump wavelength is around 1541 nm or 1556 nm and the probe wavelength is at 1548 nm.

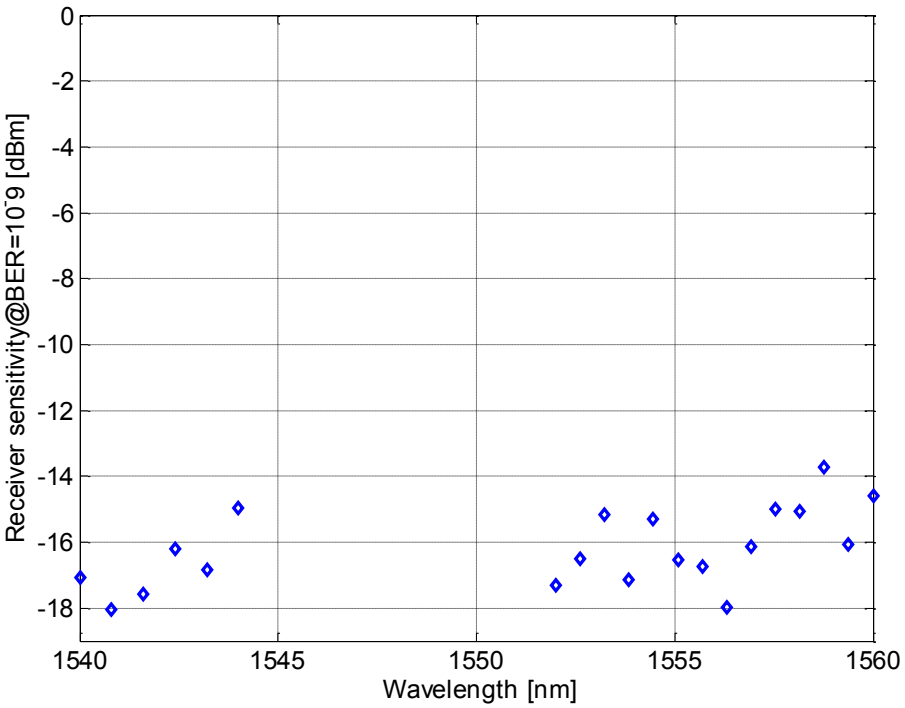

Figure 4.1 Receiver sensitivity as a function of pump wavelength for an RZ probe at 1548 nm.

We then change the pump wavelength to 1552 nm and repeat the simulation while keeping all other parameters the same. From Figure 4.2, we can observe that the minimum receiver sensitivity is acquired when the pump wavelength is around 1544 nm or 1560 nm and the received power is around -18 dBm. Comparing Figures 4.1 and 4.2, we can see that as long as $\Delta\lambda$ is more than 4 nm, the format conversion is functioning. For $\Delta\lambda < 4$ nm, parametric amplification can distort the signal. The lowest receiver sensitivities for both cases are quite similar, around -17 dBm.

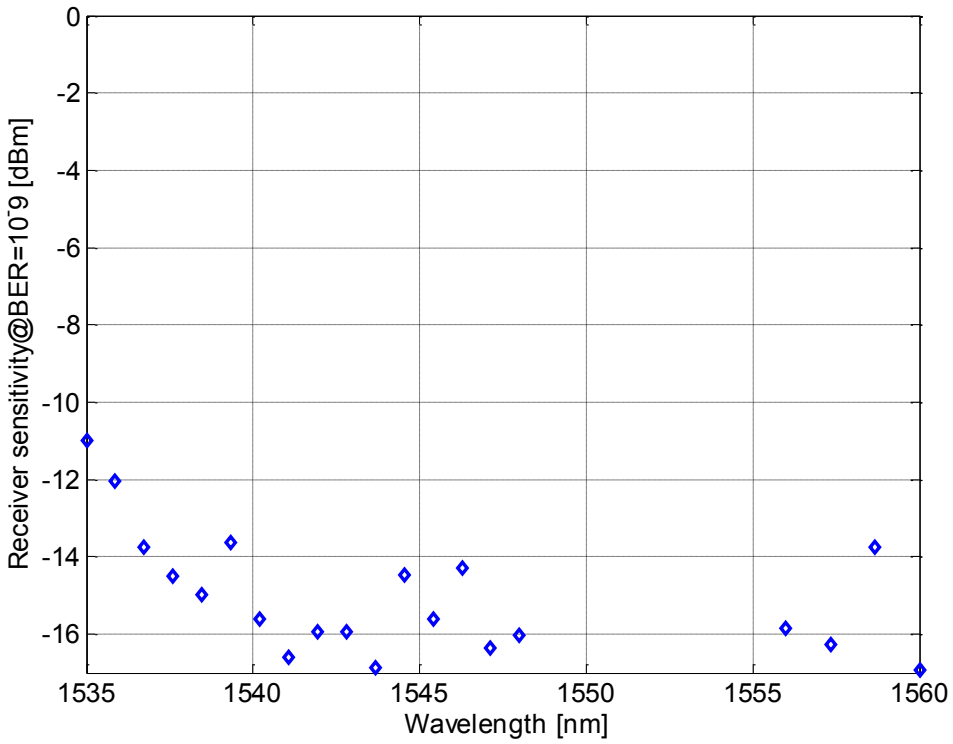

Figure 4.2 Receiver sensitivity as a function of pump wavelength for an RZ probe at 1552 nm.

To have a much clearer view of the impact of wavelength spacing between probe and pump, we plot the receiver sensitivity as a function of pump power for $\Delta\lambda$ of 12 nm, 8 nm, 4 nm and -4 nm (the pump is fixed at 1548 nm). From Figure 4.3, we can observe that the four different spacing sets have similar traces. Compared to 10 Gb/s, it is

obvious that the 40 Gb/s system requires a higher power level and the received power is around 3 dB higher.

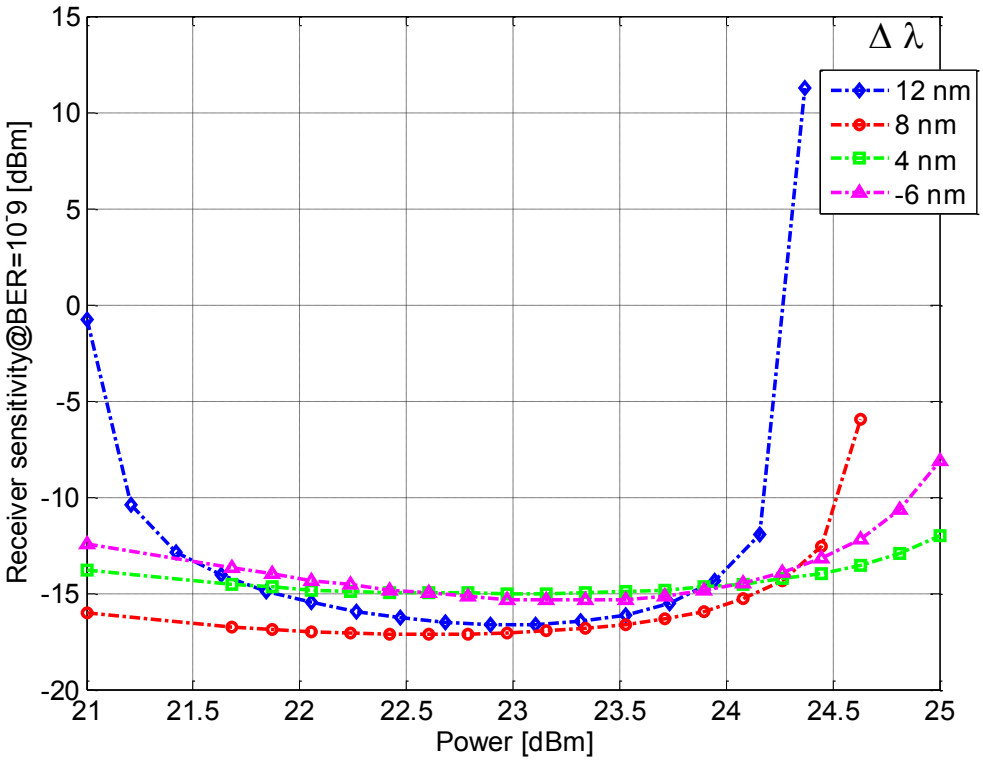

Figure 4.3 Receiver sensitivity plot versus pump power when probe is RZ.

4.2.2 CW Probe case

Next, we consider the case when the probe is CW. We fix the pump peak power at 22.5 dBm and the probe peak power at 0 dBm. The probe wavelength is at 1540 nm, and we vary the pump wavelength.

From Figure 4.4, we can observe that the minimum receiver sensitivity is acquired when pump wavelength is around 1552 nm. The received power is around -16 dBm which is 2 dB higher than the RZ probe case.

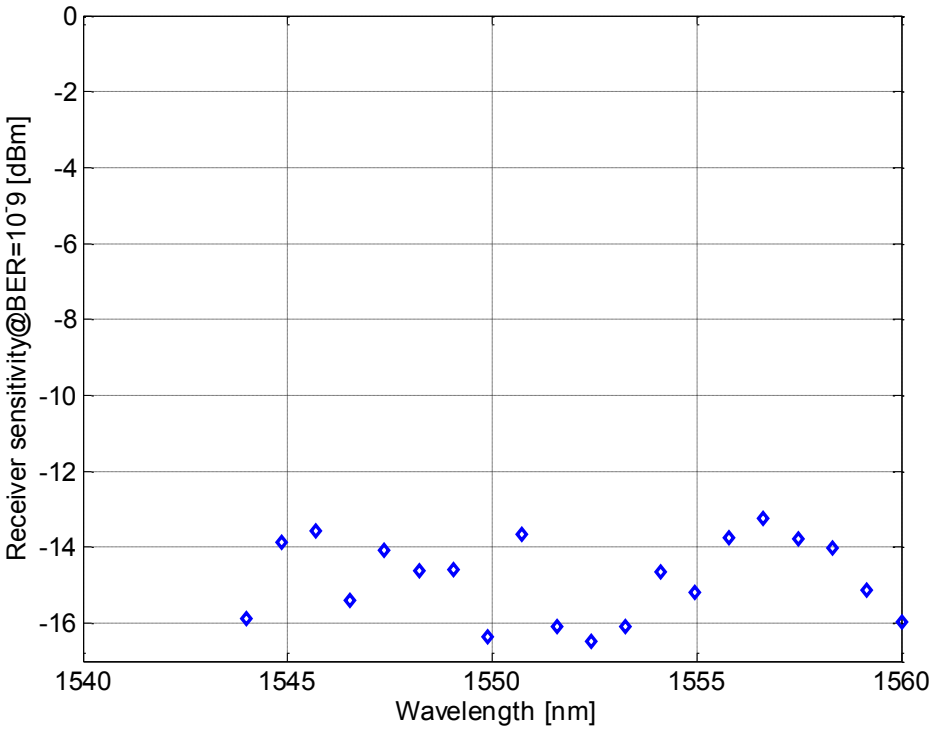

Figure 4.4 Receiver sensitivity plot of pump wavelength when probe is 1540nm when probe is CW.

For comparison, we then fix the probe wavelength at 1550 nm and vary the pump wavelength. From Figure 4.5, we can observe that the minimum receiver sensitivity is acquired when the pump wavelength is around 1540 nm or 1544 nm, and the probe wavelength is at 1550 nm. Comparing the two plots, we can see that the requirements for using a CW probe are similar to an RZ probe, which is that $\Delta\lambda$ should be more than 4 nm. The pump power versus received power plot is also plotted at different values of $\Delta\lambda$ for the CW probe. For these set of data, the probe wavelength is fixed at 1540 nm; while $\Delta\lambda = 4$ nm, 8 nm, and 12 nm.

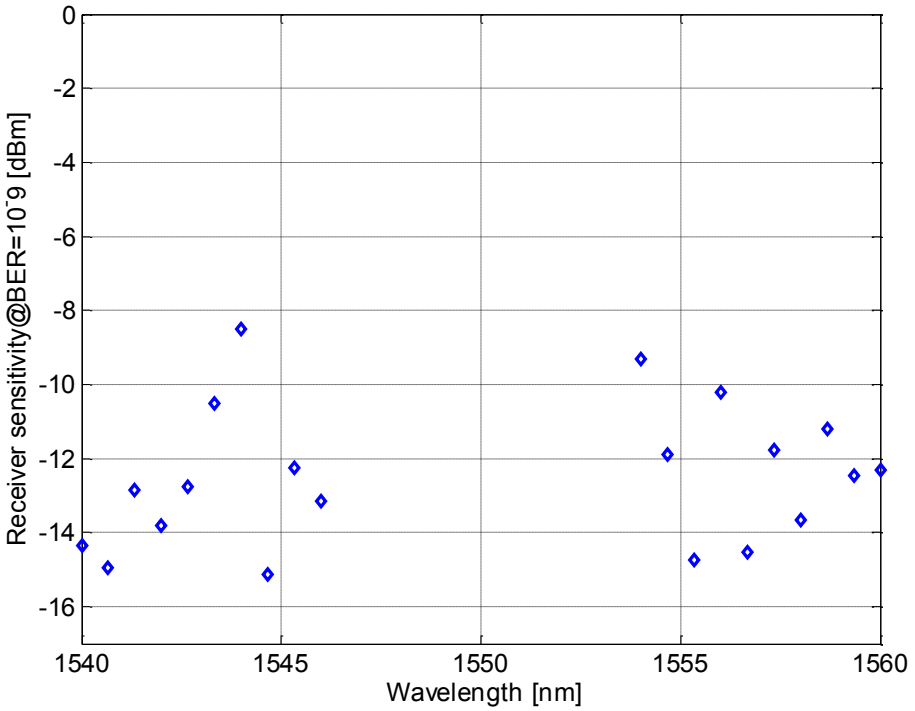

Figure 4.5 Receiver sensitivity plot of probe wavelength when probe is 1555nm CW.

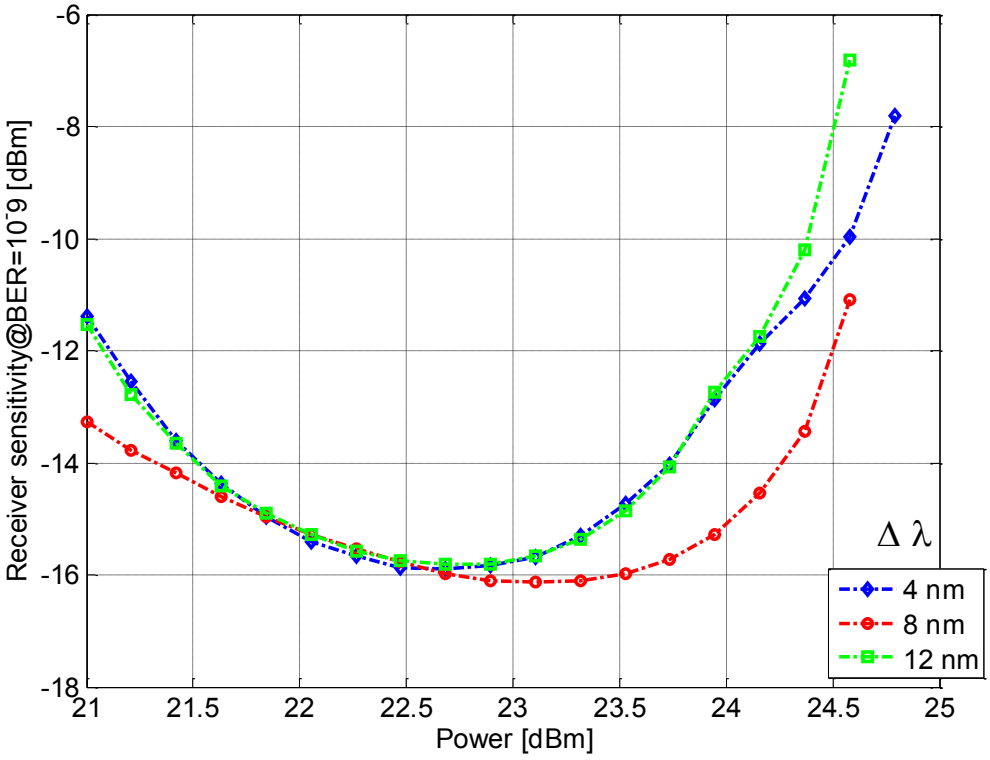

Figure 4.6 Receiver sensitivity plot versus pump power when probe is CW.

Similar to RZ probe case, the traces in Figure 4.6 have a similar shape. The lowest receiver sensitivity Δλ set is 8 nm. Comparing 10 Gb/s system and 40 Gb/s system, we can see that the power level required for 40 Gb/s is higher than 10 Gb/s system, the received power is 2 dB higher. The higher power level required is expected, since the duty cycle of the pump is larger for 40 Gb/s.

In Sections 4.3-4.7, we simulate the dependence of the quality of the converted signal on important properties of the input data signal, including the duty cycle, state of polarization, PMD, OSNR, and residual dispersion. For each case, we plotted the receiver sensitivity to quantify the conversion performance. If not mentioned specifically, the RZ probe has a duty cycle of 33%, a wavelength of 1540 nm, and a peak power of 0 dBm. The CW probe has a wavelength of 1540 nm, and a peak power of 0 dBm. The RZ-OOK pump has a duty cycle of 50%, a wavelength of 1548 nm, and a peak power of 22.5 dBm. The reason we choose the probe wavelength to be 1540 nm and pump wavelength to be 1548 nm has been discussed previously; they have a wavelength spacing larger than 4 nm and they have the minimum receiver sensitivity compared to others.

4.3

Duty Cycle

4.3.1 RZ Probe case

First, we want to determine whether or not the duty cycle of the RZ probe pulse has an impact on the format conversion performance under 40 Gb/s bit rate. The pump is

a 50% RZ-OOK signal (33% did not work) and we vary the duty cycle of the probe pulse to plot the receiver sensitivity.

Figure 4.7 shows that, similar to 10 Gb/s case, as the duty cycle increases, the received power increases, which is equivalent to a decrease in the conversion performance.

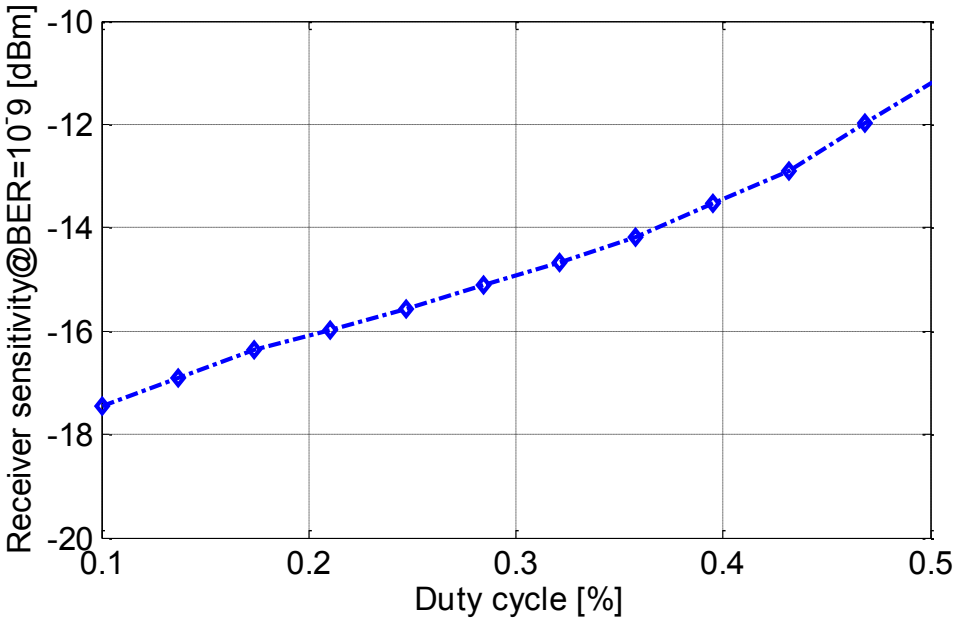

Figure 4.7 Receiver sensitivity plot versus probe duty cycle when probe is RZ.

Next, we want to see whether or not the duty cycle of the pump pulse has an impact on the format conversion performance. Figure 4.8 shows that the performance of the format conversion increases as the pump duty cycle increases. The peak power of the RZ-OOK signal is kept constant at 22.5 dBm. The larger the duty cycle is, the better the performance of XPM. Compared to the 10 Gb/s system, we can see that the pump duty cycle required at 40 Gb/s system is larger. The format conversion fails when the duty cycle of the pump is below 30%.

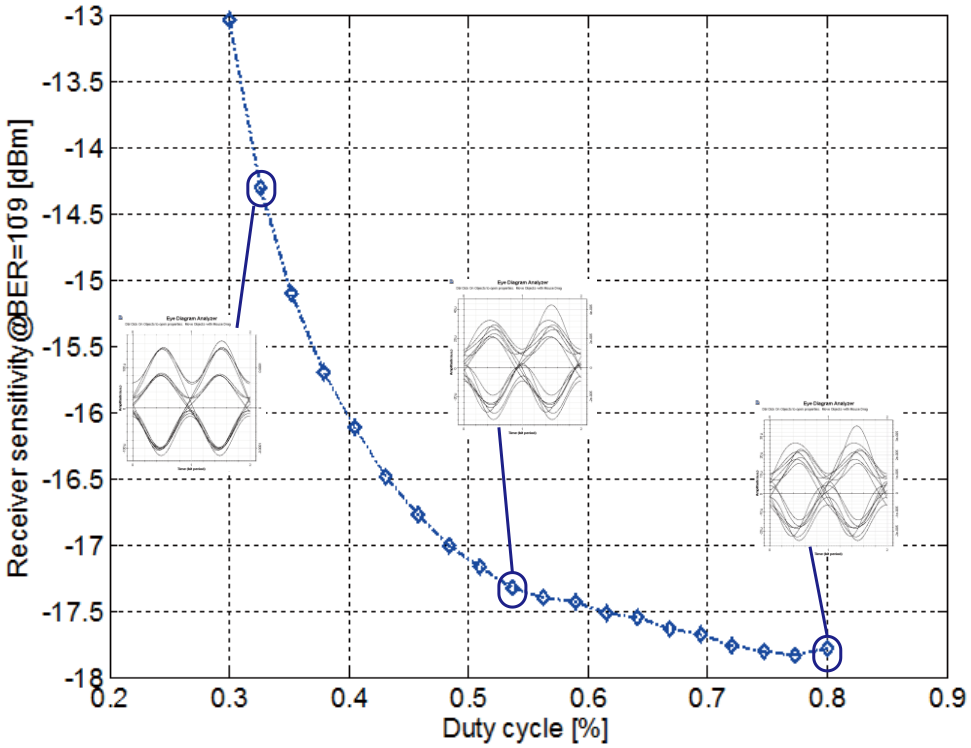

Figure 4.8 Receiver sensitivity plot versus pump duty cycle when probe is RZ.

4.3.2 CW Probe case

For the CW probe case, we only plot the receiver sensitivity as a function of the duty cycle of the pump pulse. By observing Figure 4.9, we can see that the performance of the format conversion with CW probe initially improves as the pump duty cycle increases up to around 65%, then the performance worsens as the pump duty cycle keeps increasing. The optimum received power is around -16 dBm. Similar to the RZ case, the peak power of the RZ-OOK signal is kept constant at 22.5 dBm.

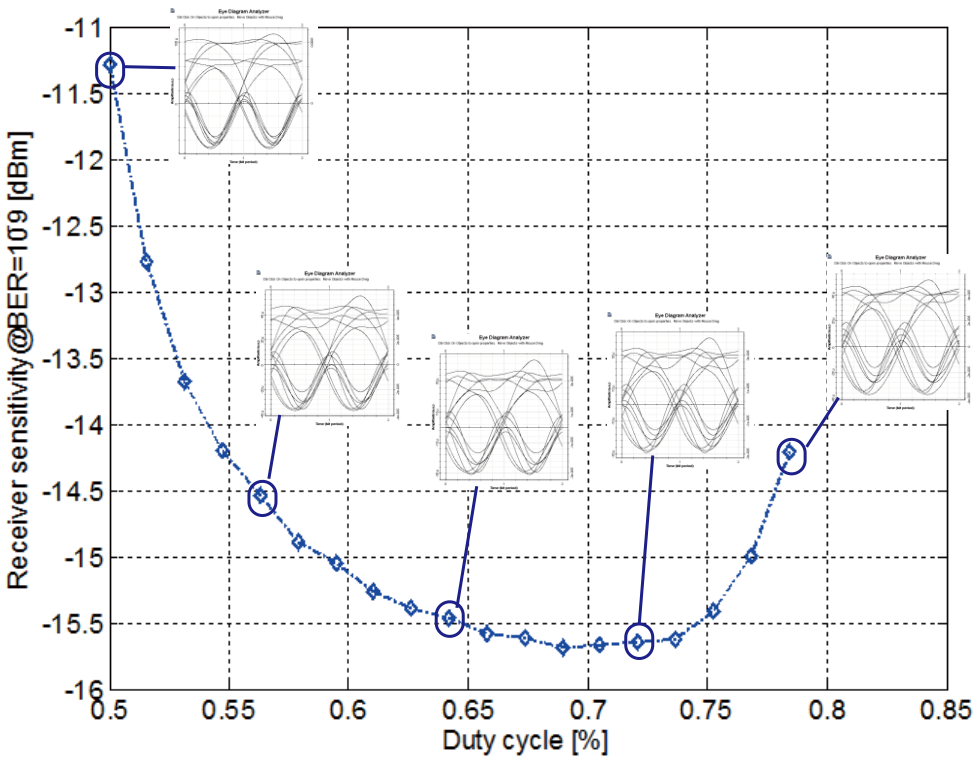

Figure 4.9 Receiver sensitivity plot versus pump duty cycle when probe is CW.

4.4

State of Polarization

We then illustrate the impact of polarization to the conversion process. We fix the probe signal angle at 0 degrees, and plot the receiver sensitivity as a function of the angle of the pump signal. Both a CW probe and an RZ probe are plotted for comparison. Figure 4.10 illustrates that when the pump signal is co-polarized with the probe signal, the receiver sensitivity improves by 3 dB compared to when there is a 50 degree difference between the SOP of the pump and probe. The largest difference in angle is 10 degrees less than the 10 Gb/s system.

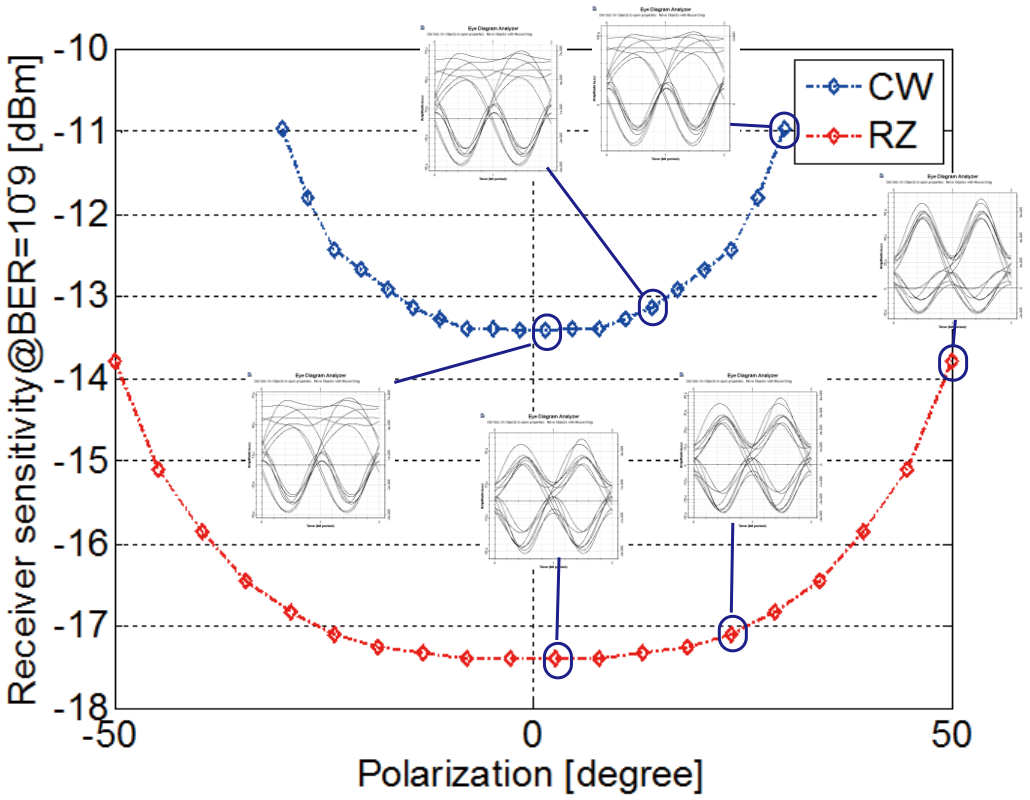

Figure 4.10 Receiver sensitivity plot versus polarization.

4.5

PMD

Figure 4.11 shows the dependence of the receiver sensitivity on the DGD of the input signal for both a CW and an RZ probe. The performance of the conversion using a CW probe is more stable than an RZ probe, due to the narrow shape of the RZ pulse. Compared to the 10 Gb/s system, the performance worsens when the probe is RZ.

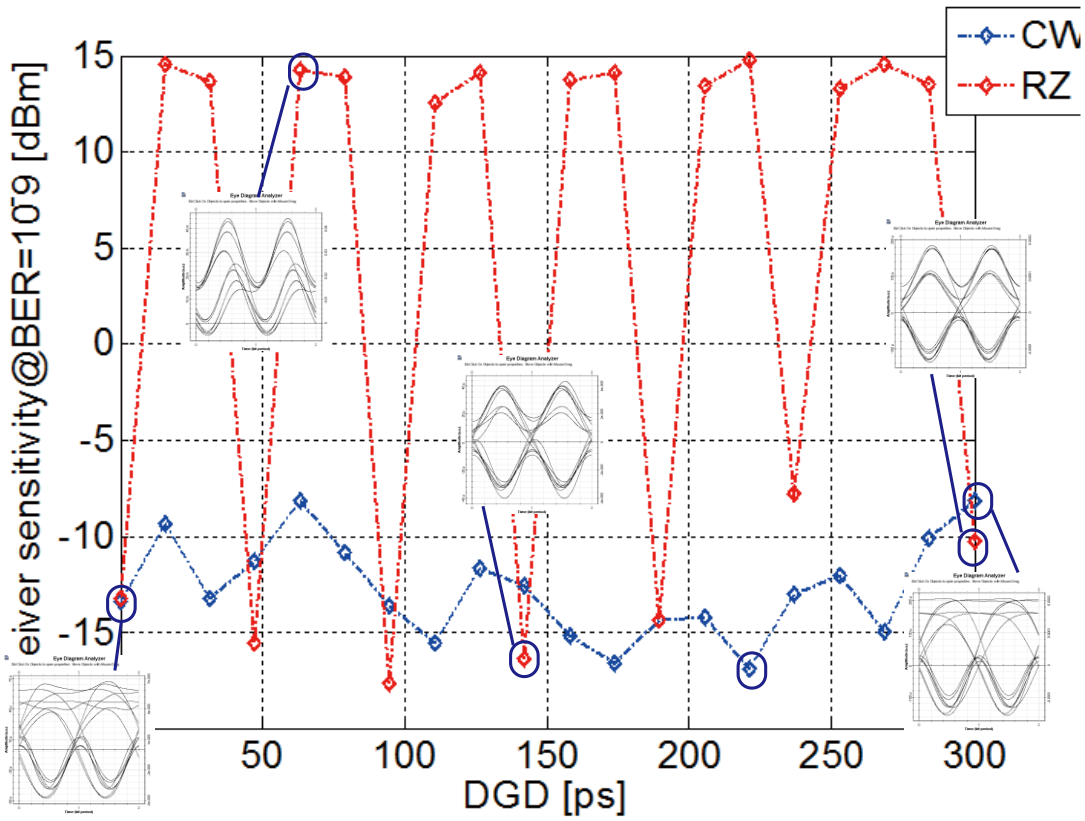

Figure 4.11 Receiver sensitivity plot versus DGD.

4.6

OSNR

When the OSNR of the input signal is greater than 33.9 dB (0.1 nm noise bandwidth), the receiver sensitivity for error-free format conversion is -16 dBm and -12 dBm for an RZ probe and a CW probe, respectively. The results are summarized in Figure 4.12. Compared to 10 Gb/s system, the performance does not drop from OSNR perspective.

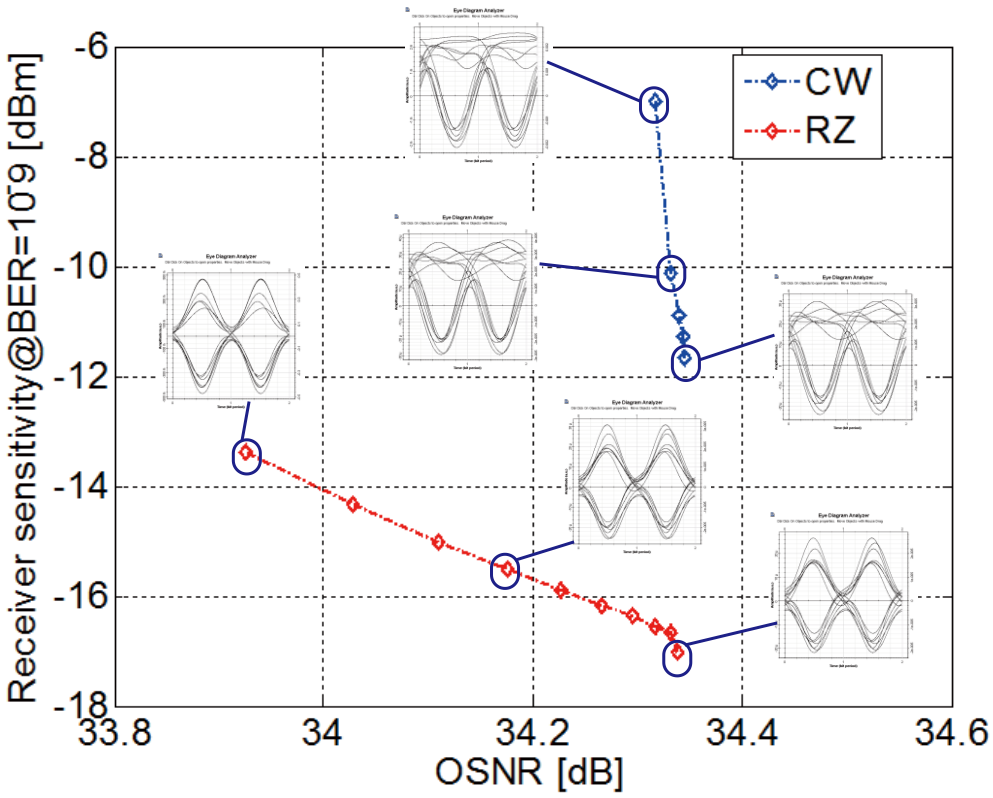

Figure 4.12 Receiver sensitivity plot versus OSNR.

4.7

Residual Dispersion

Figure 4.13 illustrates the dependence of the receiver sensitivity of the format conversion on the residual dispersion of the 40 Gb/s RZ-OOK signal. The receiver sensitivity is about -17 dBm and -13 dBm for a residual dispersion in the range of -50 ps/nm to 50 ps/nm for an RZ and CW probe, respectively. Outside this range, pulse broadening causes degradation in the format conversion performance analogous to signals with a large duty cycle. The RZ probe case is more stable compared to the CW probe. Compared to 10 Gb/s system, as the data rate increased, the degradation due to dispersion is much more significant, since the pulse width is narrower.

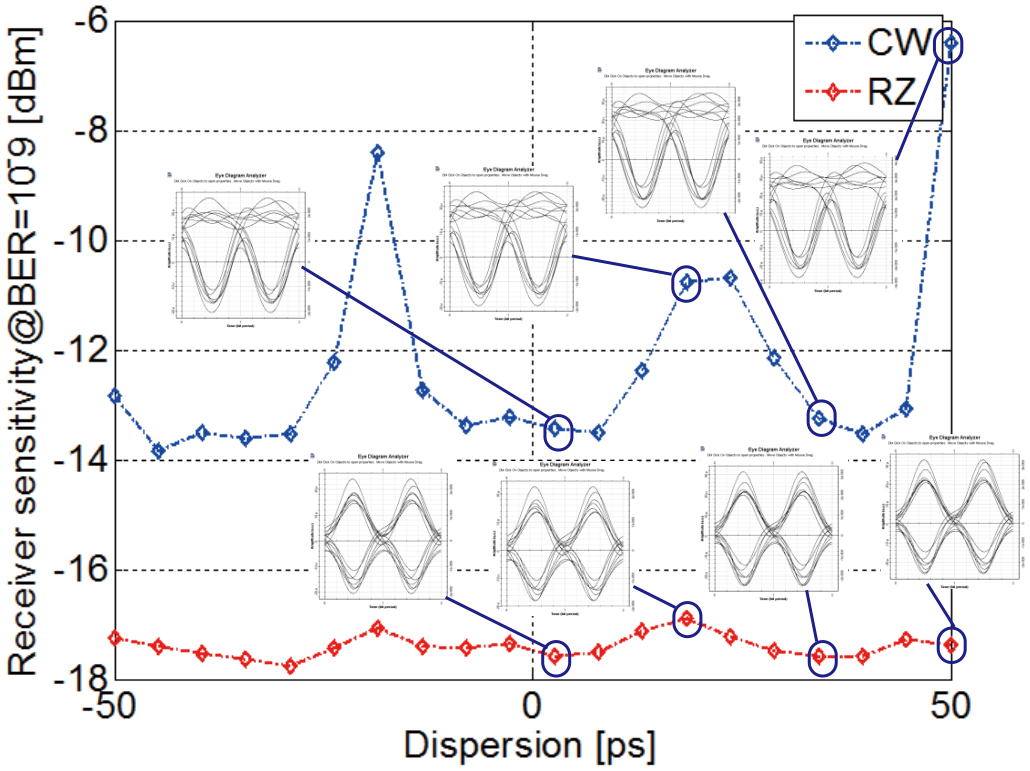

Figure 4.13 Receiver sensitivity plot versus residual dispersion.

4.8

Summary

In this chapter, we investigate the RZ-OOK to RZ-DPSK modulation format conversion at a data rate of 40 Gb/s. From the simulations, we conclude that the format conversion is feasible at 40 Gb/s. Compared to the 10 Gb/s system, the 40 Gb/s system requires a larger pump duty cycle, which results in a higher power level and lower residual dispersion requirements.

Chapter 5

Conclusion and Future works

This thesis studied the phase information extraction and phase modulated signals format conversion in all optical communication. Chapter 1 provided a brief historical background of the field of optical fiber communications and explained the need for optical modulation format conversion that is capable of future high speed network. In particular, the OOK to DPSK format conversion is critical in a metropolitan network to long-haul transmission systems. In Chapter 2, a novel method of phase characterization for optical signals was provided. The resolution is high and the setup is simple. Chapter 3 gave a detailed theoretical characterization of the all optical OOK to DPSK conversion. Simulation results and experiment results were obtained between the RZ probe and the CW probe for the dependence of the received power to have 10^{-9} BER of the converted DPSK signal. We investigated the variation of the conversion quality due to the variation on the input signal duty cycle, peak power, state-of-polarization (SoP), OSNR, and waveform distortion due to PMD and residual dispersion. For the format conversion of the input signal to be functioning, the input signal properties must satisfy the following: duty cycle from 20 to 60%, peak power from 21 to 23 dBm, OSNR larger than 34 dB (0.1 nm bandwidth), residual dispersion from 0ps/nm to 300 ps/nm, and differential group delay smaller than 30 ps. The

polarization control is particularly effective for degradation in the performance of format conversion. This result is important since most fiber systems are birefringence. A non-birefringence system is highly desirable for format conversions involving XPM. In the experiment verification part, we added a polarizer to minimize the degradation from polarization. All the experimental results agree with the simulation results. Based on the characterization results, we designed and built a setup of OOK to DPSK modulation format conversion with wavelength multicasting. All the channels can have an error-free operation with low received power. Chapter 4 showed the simulation of the OOK to DPSK modulation format conversion at 40 Gb/s.

One obvious extension to this work would be to carry out the experiment at 40 Gb/s, since the analysis of the OOK to DPSK format conversion at higher data rate is required. Furthermore, we could implement the analysis of the OOK to QPSK format conversion and the BPSK to QPSK format conversion. The modulation format of DP-QPSK is being extensively studied for future transmission systems.

References

[1] M. Mims III. “Alexander Graham Bell and the Photophone: The Centennial of the ivention of Light-Wave Communications, 1880-1980.”, *Opt. News 6*, no. 1 ,1980: 8-16.

[2] A. A. Huurdeman, The Worldwide History of Telecommunication, Wiley, New York, 2003, Chap. 21.

[3] T. H. Maiman, “Stimulated Optical Radiation in Ruby,” *Nature* 187, 493, 1960.

[4] K. C. Kao and G. A. Hockman, “Dielectric-fibre surface waveguides for optical frequencies,” *Proc. IEE 113,* 1151 (1966); A. Werts, Onde Electr. 45, 967, 1966.

[5] G. P. Agrawal, Lightwave technology telecommunication systems, Hoboken, N.J.: Wiley-Interscience, 2005.

[6] I. Magaziner and M. Patinkin, The Silent War: Inside the Global Business Battles Shaping America’s Future, NY: Vintage Books, 1989.

[7] J. I. Yamada, S. Machida, and T. Kimura, “2 Gbit/s optical transmission experiments at 1.3 um with 44 km single-mode fibre,” *Electronics Letters*, vol. 17, 479, 1981.

[8] A. H. Gnauck, B. L. Kasper, R. A. Linke, R. W. Dawson, T. L. Koch, T. J. Bridges, E. G. Burkhardt, R. T. Yen, D. P. Wilt, J. C. Campbell, K. C. Nelson, and L. G. Cohen, "4 Gbit/s transmission over 103 km of optical fiber using a novel electronic multiplexer/demultiplexer," *J. Lightwave Technol.*, vol. 3, no.2, 1032, 1985.

[9] J. M. Kahn and K.-P. Ho, "Spectral efficiency limits and modulation/detection techniques for DWDM Systems", *J. Sel. Top. Quantum Electron*., vol. 10, no.2, 259–271, 2004.

[10] P. J. Winzer and R.-J. Essiambre, "Advanced optical modulation formats", *Proc. IEEE*, vol. 94, no.5, pp. 952, 2006.

[11] K. Fukuchi, T. Kasamatsu, M. Morie, R. Ohhira, T. Ito, K. Sekiya, D. Ogasahara, and T. Ono, "10.92-Tb/s (273 × 40-Gb/s) triple-band/ultra-dense WDM optical repeatered transmission experiment," in *Proc. Optical Fiber Communication Conf. (OFC)*, 2001, Paper PD24.

[12] Y. Frignac, G. Charlet, W. Idler, R. Dischler, P. Tran, S. B. S. Lanne, C. Martinelli, G. Veith, A. Jourdan, J.-P. Hamaide, and S. Bigo, "Transmission of 256 wavelengthdivision and polarization-divisionmultiplexed channels at 42.7 Gb/s (10.2 Tb/s capacity) over 3 × 100 km of TeraLight fiber," in *Proc. Optical Fiber Communication Conf. (OFC),* 2002, Paper FC5.

[13] G. Charlet, E. Corbel, J. Lazaro, A. Klekamp, R. Dischler, P. Tran, W. Idler, H. Mardoyan, A. Konczykowska, F. Jorge, and S. Bigo, "WDM transmission at 6 Tbit/s capacity over transatlantic distance and using 42.7 Gb/s differential phase-shift keying without pulse carver," in Proc. Optical Fiber Communication Conf. (OFC), 2004, Paper PDP36.

[14] A. H. Gnauck, G. Raybon, S. Chandrasekhar, J. Leuthold, L. S. C. Doerr, A. Agarwal, S. Banerjee, D. Grosz, S. Hunsche, A. M. A. Kung, D. Maywar, M. Movassaghi, X. Liu, C. Xu, X. Wei, and D. M. Gill, "2.5 Tb/s (64 × 42.7 Gb/s) transmission over 40 × 100 km NZDSF using RZ-DPSK format and all Raman amplified spans," in *Proc. Optical Fiber Communication Conf*. (OFC), 2002, Paper FC2.

[15] C. Rasmussen, T. Fjelde, J. Bennike, F. Liu, S. Dey, P. M. B. Mikkelsen, P. Serbe, P. V. der Wagt, Y. Akasaka, D. Harris, D. Gapontsev, V. Ivshin, and P. Reeves-Hall, "DWDM 40 G transmission over transpacific distance (10,000 km) using CSRZ-DPSK and enhanced FEC and all Raman amplified 100 km Ultrawave fiber spans," in *Proc. Optical Fiber Communication Conf. (OFC)*, 2001, Paper PD18.

[16] G. Charlet, J. Renaudier, H. Mardoyan, P. Tran, O.B. Pardo, F. Verluise, M. Achouche, A. Boutin, F. Blache, J.-Y. Dupuy, S. Bigo, "Transmission of 16.4-bit/s Capacity Over 2550 km Using PDM QPSK Modulation Format and Coherent Receiver," *Journal of Lightwave Technology*, vol.27, no.3, pp.153-157, Feb.1, 2009.

[17] J. Leibrich, C. Wree, and W. Rosenkranz, "Phase shift keying (PSK & DPSK) techniques for long-haul wavelength division multiplexing systems over standard single-mode fiber", *Proc. SPIE* 4906, 1 ,2002.

[18] C. Xu, X. Liu, and X. Wei, "Differential phase-shift keying for high spectral efficiency optical transmissions", *IEEE J. Sel. Top. Quantum Electron*., vol.10, no.2, 281, 2004.

[19] A. H. Gnauck and P. J. Winzer, "Optical phase-shift-keyed transmission," *J. Lightw. Technol*., vol. 23, no. 1, pp. 115–130, Jan. 2005.

[20] G. Charlet, E. Corbel, J. Lazaro, A. Klekamp, R. Dischler, P. Tran, W. Idler, H. Mardoyan, A. Konczykowska, F. Jorge, and S. Bigo, "WDM transmission at 6 Tbit/s capacity over transatlantic distance and using 42.7 Gb/s differential phase-shift keying without pulse carver," in *Proc. Optical Fiber Communication Conf. (OFC),* 2004, Paper PDP36.

[21] D. Penninckx, H. Bissessur, P. Brindle, E. Gohin, and F. Bakhti, "Optical differential phase shift keying (DPSK) direct detection considered as a duobinary signal," in *Proc. ECOC* 2001, Amsterdam, The Netherlands, 2001, pp. 456–457.

[22] R. A. Linke and A. H. Gnauck, "High-capacity coherent lightwave systems," *J. Lightwave Technol.*, vol. 6, no.10, pp. 1750–1769, 1988.

[23] J. P. Gordon and L. F. Mollenauer, "Phase noise in photonics communications systems using linear amplifier," *Opt. Lett.*, vol. 15, no.23, pp. 1351–1355, 1990.

[24] O. Vassilieva, T. Hoshida, S. Choudhary, G. Castanon, H. Kuwahara, T. Terahara, and H. Onaka, "Numerical comparison of NRZ, CS-RZ and IM-DPSK formats in 43 Gbit/s WDM transmission," in *Proc. IEEE LEOS 14th Annu. Meeting*, 2001, pp. 673–674.

[25] P. S. Cho, V. S. Grigoryan, N. Reingand, and I. Shpantzer, "Optical differential binary phase shift keying of return-to-zero pulses for long-haul DWDM transmission systems," presented at the *OECC* 2002, Yokohama, Japan, 2002, Paper PD-1-7.

[26] C. Xu, X. Liu, L. F. Mollenauer, and X. Wei, "Comparison of return-to-zero differential phase-shift keying and on-off keying in long-haul dispersion

managed transmission," *IEEE Photon. Technol. Lett.*, vol. 15, no.4, pp. 617–619, 2003.

[27] K. Mishina, A. Maruta, S. Mitani, T. Miyahara, K. Ishida, K. Shimizu, T. Hatta, K. Motoshima, and K. Kitayama, "NRZ-OOK to RZ-BPSK Modulation Format Conversion Using SOA-MZI Wavelength Converter", *Journal of Lightwave Technology*, vol. 24, no.10, 2006.

[28] K. Mishina, S. M. Nissanka, A. Maruta, S. Mitani, K. Ishida, K. Shimizu, T. Hatta, and K. Kitayama, "All-optical modulation format conversion from NRZ-OOK to RZ-QPSK using parallel SOA-MZI OOK/BPSK converters" *Optics Express*, vol. 15, no.12, 2007.

[29] K. Mishina, S. Kitagawa, and A. Maruta, "All-optical modulation format conversion from on-off-keying to multiple-level phase-shift-keying based on nonlinearity in optical fiber" *Optics Express*, vol. 15, no.13, 2007.

[30] S. Kitagawa, S. M. Nissanka, and A. Maruta, "All-optical modulation format conversion from NRZ-OOK to RZ-M-ary PSK based on fiber nonlinearity", *OFC/NFOEC* 2008. Conference on, vol., no., pp.1-3, 24-28 Feb. 2008.

[31] I. Kang and C. Dorrer, ''Method of optical pulse characterization using sinusoidal optical phase modulations,'' *Opt. Lett*., vol. 32, no.17, pp. 2538-2540, 2007.

[32] C. Dorrer and I. Kang, "Simultaneous temporal characterization of telecommunication optical pulses and modulators by use of spectrograms," *Optics Letters*, vol. 27, no.15, pp. 1315–1317, 2002.

[33] I. Kang and C. Dorrer, “Highly sensitive differential tomographictechnique for real-time ultrashort pulse characterization,” *Opt. Lett*., vol. 30, no.12, pp. 1545-1547, 2005.

[34] I. Walmsley and C. Dorrer, “Characterization of ultrashort electromagnetic pulses,” *Adv. Opt. Photon*., vol. 1, no.2, 308-437, 2009.

[35] C. Dorrer and I. Kang, “Complete temporal characterization of short optical pulses by simplified chronocyclic tomography,” *Opt. Lett*.,vol. 28, no. 20, pp. 1481-1483, 2003.

[36] B. C. Thomsen, M. A. F. Roelens, R. T.Watts, and D. J. Richardson, “Comparison between nonlinear and linear spectrographic techniques for the complete characterization of high bit-rate pulses used in optical telecommunications,” *IEEE Photon. Technol. Lett*., vol. 17, no.9, pp. 1914–1916, 2005.

[37] R. Trebino, K. W. DeLong, D. N. Fittinghoff, M. A. Krumbügel, B. A. Richman, and D. J. Kane, “Measuring ultrashort laser pulses in the time frequency domain using frequency-resolved optical gating,” Amer. Inst. Phys., *Rev. Sci. Instrum.,* vol. 68, pp. 3277–3295, 1997.

[38] J. L. A. Chilla and O. E. Martinez, “Direct determination of the amplitude and the phase of femtosecond light pulses,” *Opt. Lett.*, vol. 16, no.1, pp. 39–41, 1991.

[39] R. Trebino, ed., “Frequency Resolved Optical Gating: the Measurement of Ultrashort Optical Pulses”*,* Kluwer Academic, 2002.

[40] C. Iaconis and I. A. Walmsley, "Spectral phase interferometry for direct electric-field reconstruction of ultrashort optical pulses," *Opt. Lett*., vol. 23, no.10, 792–794, 1998.

[41] C. Iaconis and I. A. Walmsley, "Self-referencing spectral interferometry for measuring ultrashort optical pulses," *IEEE J. Quantum Electron.* **35**, pp. 501–509 ,1999.

[42] H. Kimand A.H. Gnauck, "Chirp characteristics of dual-drive Mach-Zehnder modulator with a finite DC extinction ratio," *IEEE Photonics Technology Letters*, vol. 14, no.3, pp.298-300, Mar 2002.

[43] G. P. Agrawal, Fiber - Optic Communications Systems, Fourth edition, 2007, Wiley Series in microwave and optical engineering.

[44] W. Astar, P. Apiratikul, B.M. Cannon, T. Mahmood, J.J. Wathen, J.V. Hryniewicz, S. Kanakaraju, C.J.K. Richardson, T.E. Murphy, and G.M. Carter, "Conversion of RZ-OOK to RZ-BPSK by XPM in a Passive AlGaAs Waveguide," *IEEE Photonics Technology Letters,* vol. 23, no.19, pp.1397-1399, Oct.1, 2011.